

Dr.
MAT
1420

Heat Transfer Characteristics of Sisko Fluid in the presence of Convective Boundary Conditions



By

Rabia Malik

Department of Mathematics
Quaid-i-Azam University, Islamabad
PAKISTAN
2017



Heat Transfer Characteristics of Sisko Fluid in the presence of Convective Boundary Conditions



By

Rabia Malik

Supervised by

Dr. Masood Khan

Department of Mathematics
Quaid-i-Azam University, Islamabad
PAKISTAN
2017

**Heat Transfer Characteristics of Sisko Fluid in
the presence of Convective Boundary
Conditions**

By

Rabia Malik

A Thesis
Submitted in the Partial Fulfillment of the
Requirements for the Degree of
DOCTOR OF PHILOSOPHY
IN
MATHEMATICS

Supervised by

Dr. Masood Khan

Department of Mathematics
Quaid-i-Azam University, Islamabad
PAKISTAN
2017

Author's Declaration

I **Rabia Malik** hereby state that my PhD thesis titled **Heat Transfer Characteristics of Sisko Fluid in the presence of Convective Boundary Conditions** is my own work and has not been submitted previously by me for taking any degree from the Quaid-i-Azam University Islamabad, Pakistan or anywhere else in the country/world.

At any time if my statement is found to be incorrect even after my graduate the university has the right to withdraw my PhD degree.

Rabia Malik.

Name of Student: **Rabia Malik**

Date: **23-01-2017**

Plagiarism Undertaking

I solemnly declare that research work presented in the thesis titled "Heat Transfer Characteristics of Sisko Fluid in the presence of Convective Boundary Conditions" is solely my research work with no significant contribution from any other person. Small contribution/help wherever taken has been duly acknowledged and that complete thesis has been written by me.

I understand the zero tolerance policy of the HEC and Quaid-i-Azam University towards plagiarism. Therefore, I as an Author of the above titled thesis declare that no portion of my thesis has been plagiarized and any material used as reference is properly referred/cited.

I undertake that if I am found guilty of any formal plagiarism in the above titled thesis even afterward of PhD degree, the University reserves the rights to withdraw/revoke my PhD degree and that HEC and the University has the right to publish my name on the HEC/University Website on which names of students are placed who submitted plagiarized thesis.

Student/Author Signature: *Rabia Malik*

Name: Rabia Malik

Certificate of Approval

is to certify that the research work presented in this thesis entitled Heat Transfer Characteristics of Sisko Fluid in the presence of Convective Boundary Conditions was conducted by Ms Rabia Malik under the supervision of Prof. Dr. Masood Khan. No part of this thesis has been submitted anywhere else for any other degree. This thesis is submitted to the Department of Mathematics, Quaid-i-Azam University, Islamabad in partial fulfillment of the requirements for the degree of Doctor of Philosophy in Field of Mathematics from Department of Mathematics, Quaid-i-Azam University Islamabad, Pakistan.

Student Name: Rabia Malik Signature: *Rabia Malik.*

External committee:

a) External Examiner 1: Signature:
Name: Dr. Rahmat Ellahi
Designation: Associate Professor
Office Address: IIUI, Islamabad

R. Ellahi
23/1/2017

b) External Examiner 2: Signature:
Name: Dr. Tanvir Akbar Kiani
Designation: Assistant Professor
Office Address: CIIT, Islamabad

Tanvir Akbar Kiani
23.01.2017

c) Internal Examiner: Signature:
Name: Dr. Masood Khan
Designation: Professor
Office Address: Department of Mathematics, QAU Islamabad.

Masood Khan



Supervisor Name: Signature: *Masood Khan.*
Prof. Dr. Masood Khan

Name of Dean/ HOD Signature:

Muhammad Yousaf Malik

Prof. Dr. Muhammad Yousaf Malik

Heat Transfer Characteristics of Sisko Fluid in the presence of Convective Boundary Conditions

By

Rabia Malik

CERTIFICATE

A DISSERTATION SUBMITTED IN THE PARTIAL FULFILLMENT OF THE REQUIREMENTS FOR THE DEGREE OF THE DOCTOR OF PHILOSOPHY

We accept this dissertation as conforming to the required standard.



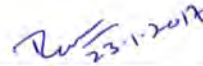
Dr. Masood Khan
(Supervisor)



Prof. Dr. Muhammad Yousaf Malik
(Chairman)



Dr. Rahmat Ellahi
(External Examiner)
Associate Professor, IIUI,
Islamabad



Dr. Tanvir Akbar Kiani
(External Examiner)
Assistant Professor, CIIT,
Islamabad

Department of Mathematics
Quaid-i-Azam University
Islamabad, Pakistan
2017

Dedication

Every challenging work needs self efforts as well as guidance of elders especially those who were very close to our hearts.

My humble effort I dedicate to my sweet and loving

Father, Mother & Siblings

whose affection, love, encouragement and prays of day and night make me able to get such success and honor,

along with hard working and respected supervisor

Prof. Dr. Masood Khan

Acknowledgements

All praises is due to **Almighty Allah** alone without whose help we can do nothing. First of all, thanks to Allah, He who turn my each failure into a success and never make me hopeless. It is only His help and blessings that today I am able to accomplished my PhD studies.

May blessings be upon **Prophet Muhammad** (peace be upon Him) after whom there is no other Prophet. Bundles of thanks to **Him** (peace be upon Him), who by religious make it obligatory for us to seek education by stating “it is obligatory for every Muslim man and woman to seek education” and “seek knowledge from cradle to grave”. He (peace be upon Him) is always a source of courage and hope for me.

I would always be indebted to all my teachers by whom I gained marvelous skills and knowledge. Especially I am highly grateful to my kind natured, dedicated, sincere and devoted supervisor **Prof. Dr. Masood Khan**, a great teacher and a great human, who helped me with my research. I am always inspired by his dedication, his hard work and his style of research that would help me to conduct quality research in the future as well. Without his generous help and guidance it was not possible for me to complete this work.

I further, particularly wish to acknowledge the Ex. chairman **Prof. Dr. Tasawar Hayat** and the present chairman **Prof. Dr. Muhammad Yousaf Malik** for providing research oriented environment and excellent facilities at the department.

I am highly indebted to my senior colleagues **Dr. Asia Anjum**, **Dr. Asif Munir** and **Dr. Azeem Shahzad** for their valuable discussions and guidance throughout my Ph.D. Further, I want to extend my heartfelt thanks to my friends specially **Dr. Anum Shafiq**, **Dr. Shagufta Ijaz**, **Dr. Hina Sadaf**, **Iqra Shahzadi** and **Rehana Rahim** who always helped me during my studies in all respects.



I would like to express my heart-felt gratitude to my family; none of this would have been possible without their support. I heartily thank to my **mother** the source of love and care, my **brothers** and my **sisters** who always supported me. In last but not least, I owe sincere gratitude to my **Father (late)** whose presence was always a source of strength and inspiration for me.

Rabia Malik

Dated: 23 January, 2017

Table of Contents

Table of Contents	xi
Abstract	xv
1 Introduction	1
1.1 Introduction	1
1.1.1 The Background and Objectives of the Research	1
1.1.2 The Structure of the Thesis	11
2 Flow and Heat Transfer in Sisko Fluid with Convective Boundary Conditions	16
2.1 Mathematical Formulation	17
2.1.1 Governing Equations	17
2.1.2 Flow Equations	20
2.1.3 Heat Transfer Analysis	22
2.2 Solution Methodologies	23
2.2.1 The Homotopy Analytic Solution	23
2.2.2 The Numerical Solution	25
2.2.3 The Exact Solution for Particular Cases	25
2.3 Results and Discussion	27
3 MHD Flow and Heat Transfer of Sisko Fluid over a Radially Stretching Sheet	40
3.1 Formulation of the Problem	41
3.1.1 Geometry of the Problem	41
3.1.2 Flow and Heat Transfer Analysis	41
3.2 Solution Methodologies	44

3.2.1 The HAM Solution	44
3.2.2 The Numerical Solution	45
3.2.3 The Exact Solution	46
3.3 Results and Discussion	48
4 Mixed Convective Heat Transfer to Sisko Fluid over a Radially Stretching Sheet	63
4.1 Problem Formulation	64
4.1.1 Geometry of the Problem	64
4.2 Solution Methodologies	67
4.2.1 The HAM Solution	68
4.2.2 The Numerical Solution	68
4.3 Results and Discussion	69
5 Forced Convective Heat Transfer to Sisko Fluid Flow past a Stretching Cylinder	81
5.1 Mathematical Description of the Problem	82
5.1.1 Boundary Layer Equations.	82
5.1.2 Geometry of the Problem	84
5.1.3 Governing Equations	84
5.1.4 Boundary Conditions	85
5.1.5 Transformed Problem	85
5.1.6 Physical Quantities	87
5.2 Solution Methodologies	88
5.2.1 The Numerical Solution	88
5.2.2 The Homotopic Solution	89
5.3 Results and Discussion	90

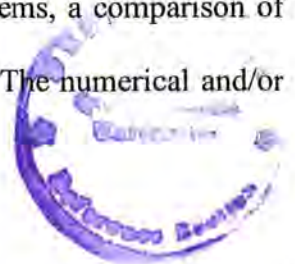


6 Nonlinear Radiative Heat Transfer to Stagnation-Point Flow of Sisko Fluid past a Stretching Cylinder	99
6.1 Problem Formulation	100
6.1.1 Physical Model	100
6.1.2 Governing Equations	100
6.1.3 Boundary Conditions	101
6.1.4 Local-Similarity Transformations	102
6.1.5 Physical Quantities	103
6.2 Solution Methodology	103
6.3 The Homotopy Solution and Validity	104
6.4 Results and Discussion	105
7 Forced Convective Heat Transfer to Sisko Nanofluid past a Stretching Cylinder in the Presence of Variable Thermal Conductivity	116
7.1 Problem Formulation	117
7.1.1 Governing Equations	117
7.1.2 Boundary Conditions	118
7.1.3 Local-Similarity Transformations	119
7.1.4 Physical Quantities	120
7.2 Solution Methodology	121
7.3 Validity of Numerical Results	122
7.4 Results and Discussion	122
8 Homogeneous-Heterogeneous Reactions in Stagnation-Point Flow of Sisko Fluid past a Stretching Cylinder	132

8.1 Formulation of the Problem	133
8.1.1 Governing Equations	133
8.1.2 Boundary Conditions	134
8.1.3 Local-Similarity Transformations	135
8.1.4 Physical Quantities	137
8.2 Solution Methodologies	137
8.2.1 The Numerical Solution	137
8.2.2 Validity of Numerical Solution	138
8.3 Results and Discussion	139
9 Conclusions and Future Work	145
9.1 Conclusions	148
9.2 Future Work	152
Bibliography	153

Abstract

Research in the thermo-fluid mechanics is crucial as it covers wide range of fundamental applied research areas. More specifically, it is a key to the understanding and development of a variety of engineering systems. Accordingly, this thesis develops a more intuitive understanding of heat transfer mechanism for the boundary layer flows involving non-Newtonian fluids. Therefore, this thesis is predominantly focused on the theoretical analysis of the heat transfer phenomenon in the Sisko fluid flow while convective boundary conditions are considered. It is noteworthy, that the Sisko fluid is one of the Generalized Newtonian Fluids (GNF) or a purely viscous fluid which exhibits the properties of shear thinning and shear thickening fluids for the power law and upper Newtonian regions. This study is concerned with analyzing the steady boundary layer flows and heat transfer characteristics to the Sisko fluid over moving surfaces and considers a variety of problems of practical interest. The problems include, the forced and mixed convective heat transfer over planer and radially stretching sheet, the forced convective heat transfer over a cylinder assuming different situations e.g., stagnation-point flow, nanofluid, homogeneous and heterogeneous reactions. The modeled governing partial differential equations are transformed into the ordinary differential by using appropriate transformations. Due to evolution of the efficient computing, it is somewhat possible to calculate numerical and analytical solutions of the problems under consideration. In this work, a comprehensive study has been done and the shooting technique is used along with the Runge-Kutta method to conduct numerical simulations whereas, the homotopy analysis method is employed to obtain the analytical results. In some special cases, the exact solutions are also fabricated and compared with the obtained approximate solutions to affirm their validity. Additionally, for some considered problems, a comparison of present results with the results already available in the literature is made. The numerical and/or



analytical solutions have been generated for the velocity, temperature and concentration profiles. Important relevant physical parameters are presented graphically in order to explore their influence for both integer and non-integer values of the power-law index. Additionally, the local skin friction coefficient and local Nusselt number are presented in tabular form for a set of values of the non-dimensional parameters. Akin to previous studies, it is found that the momentum boundary layer thickness is larger for the shear thinning fluid when compared to the shear thickening fluid. Results further show that the magnitude of temperature is also larger for the shear thinning fluid as compared to the shear thickening fluid. One key observation of this discussion corresponds to that the thermal boundary layer thickness is larger in case of flow over cylinder when compared to the flow over flat plate.

Chapter 1

Introduction

1.1 Introduction

This chapter presents the literature survey for the Newtonian fluids, non-Newtonian fluids, forced convection, mixed convection, viscous dissipation, linear and non-linear thermal radiation, stagnation point flow, nanofluid and homogeneous–heterogeneous reactions. Also, a brief description of all chapters of this thesis is included in this chapter.

1.1.1 The Background and Objectives of the Research

In 1687, the research of famous British scientist Sir Isaac Newton was published usually termed as "Newton's law of viscosity". The viscous fluids follow the Newton's law of viscosity which is a direct relationship between the shear stress and the shear strain rate. Over a century later, Navier and Stokes established a consistent three dimensional theory for fluids obeying Newton's law of viscosity (viscous fluid) and so-called Navier-Stokes equations form the basis of Newtonian fluid mechanics.

It became abundantly clear from 19th century onwards that many fluids like materials having non-linear relationship between the shear stress and rate of strain



that cannot be characterized as Newtonian fluids, hence, an upsurge of interest in the field of non-Newtonian fluids was developed. Indeed, there would be no exaggeration in saying that non-Newtonian fluid behavior is so widespread in nature that the Newtonian fluid behavior feels as an exception rather than rule. Many examples of such fluids include foams, slurries, dispersions and suspensions, emulsions, certain oils, mud, paints, blood at low shear rate, clay coatings, polymer melts, greases and so forth.

The non-Newtonian fluids are more extensive class of fluids which cannot be depicted by a solitary model because the ability of each model for portraying the fluid properties is limited. Several models have been proposed in the literature to characterize different non-Newtonian fluids. A class of non-Newtonian fluids model, characterized by having viscosity depending on shear rate gained much importance due to describing most commonly existing nature of fluids, i.e., shear thinning and shear thickening, named as Generalized Newtonian Fluids (GNF) or purely viscous fluids. This class of non-Newtonian fluids does not depict elastic behavior of fluids. The most common and simplest fluid model in GNF is the power-law fluid model but this fluid model cannot predict the flow properties in upper or lower Newtonian regions. The Sisko fluid [1] model is GNF which overcomes this limitation of the power-law fluid and portrays the flow in the power-law and upper Newtonian regions. Aforementioned model is most appropriate to describe the flow behavior of fluids in high shear rate regions. Initially, this model was introduced to describe the flow of greases, as greases have high viscosities at low shear rates and low viscosities at high shear rates; but, it was found later that it also describes the flow behavior of cement pastes etc. Its industrial applications incorporate drilling fluids, cement slurries and

waterborne coatings etc.

Within a material the association of temperature is due to the motion of molecules which is directly related to the kinetic energy of molecules. The energy transferred between two points having different temperatures is referred as heat and the transfer of heat is governed by the laws of thermodynamics. More precisely, due to the spatial temperature difference the transition of thermal energy is called heat transfer.

Heat transfer theory can be utilized to determine temperature fields, heating/cooling times in the problems involving heat transfer, heat fluxes and so forth. In most typical thermal applications like heating and/or cooling heat transfer problems may arise e.g., because of the thermal insulation of the ice layer the defrosting problem in air conditioning and refrigeration admits several solutions which are dealt by heat transfer. Also, cooling rubbing parts in mechanical transmission. If overheated the oil loses its lubricating capacity; in a hydraulic converter, under the pressure created the fluid leaks. The overheating in an electric motor causes deterioration of the insulation. In an overheated internal-combustion engine the pistons may seize in the cylinders. Moreover, in engineering industries energy conversion devices (e.g., solar collectors, combustors, nuclear reactors etc.), materials processing (e.g., casting, welding, hot shaping, crystal growth etc.) and so forth are controlled by heat transfer analysis. Further, not only engineering materials, food processing, cooking, cloth washing, dish washing, ironing and drying and many other house-hold tasks are controlled by heat transfer.

Due to vast applications in a variety of engineering operations the analysis of heat transfer over a stretching surface (e.g., flat plate, cylinder etc.) has gained much importance. A few applications in the field of chemical engineering and metallurgy

include extrusion of polymers, production of paper and so forth. The final product's quality massively depends on heat transfer rate between the fluid and stretching surface during the operation of heating and/or cooling. Consequently, most suitable heating and/or cooling fluid must be chosen as it has immense influence on the heat transfer rate. The physical importance of heat transfer over a moving surface has compelled many researchers to report their findings on this topic. Heat transfer analysis is discussed by several researchers including Hassanien *et al.* [2] who analyzed the numerical solution of the similar equations governing the momentum and heat transfer from the power-law fluid induced by the stretching sheet while including the effects of variable wall temperature. Chen [3] obtained the numerical results for the heat transfer problem in a thin liquid film of the power-law fluid over an unsteady stretching sheet and discuss the impact of very small and large values of the Prandtl number. The Keller-Box method is employed by the Prasad *et al.* [4] to solve the problem of heat transfer of the power-law fluid where the non-linearly stretching sheet and a uniform transverse magnetic field are responsible for the flow. Lin *et al.* [5] assumed the modified Fourier's law by considering the temperature and velocity fields of the similar form and obtained numerical solution for the thin film flow and heat transfer of the power-law fluid.

In processes where high temperature is evoked the convective heat transfer is of incredible importance, for instance, nuclear plants, gas turbines and storage of thermal energy and so forth. To define the linear convective heat exchange condition for algebraic entities, the convective boundary conditions are considered. It is agreed that the convective boundary conditions are more practical in various industrial and engineering processes, for instance, transpiration cooling process, material drying

etc. The practical importance of the convective boundary conditions has compelled many researchers to investigate and report their findings on this topic. The three-dimensional flow of Jeffrey fluid over a stretching surface with convective boundary conditions has been examined by Shahzad *et al.* [6]. In another paper, the flow and heat transfer in an upper-convected Maxwell fluid over a moving surface in the presence of free stream velocity with convective boundary conditions is studied by Hayat *et al.* [7]. The steady flow and heat transfer in an Eyring Powell fluid over a plate moving continuously concerning convective boundary conditions is also examined by Hayat *et al.* [8]. Srinivasacharya and Bindu [9] considered the flow of micropolar fluid through inclined channel to investigate the characteristics of the slip, entropy generation and convective boundary conditions. Rundora and Makinde [10] explored the flow of third-grade fluid through a porous medium along with the Navier slip, reactive variable viscosity and asymmetric convective boundary conditions.

A mixed convection flow is the process of heat transfer occurred as a consequence of the combined effects of free convection (caused by the temperature difference of the fluid at different locations) and forced convection (caused due to the some external applied forces) flows. Recently, the study of mixed convection boundary layer flow past a moving surface has gained remarkable attention as it assumes a pivotal part in diverse applications, such as flows in the ocean and in the atmosphere, solar receivers laid open to wind currents, nuclear reactors cooled amid emergency shutdown, electronic gadgets cooled by fans, heat exchangers put in a low-velocity environment and so forth. For the case of horizontal flows over the heated surfaces the buoyancy force can be ignored. However, a strong influence can be exerted by the buoyancy force for the vertical or inclined surfaces. Extensive investigations have been attempted

by considering the boundary layer approximation on the mixed convection flow over isothermal and non-isothermal surfaces. Recently, many researchers focused on the mixed convection by taking various aspects and geometries. By only assuming the buoyancy aiding configuration, Srinivas *et al.* [11] studied the mixed convective heat transfer from a heated cylinder immersed in the power-law fluid. Shahzad and Ali [12] explored the characteristics of mixed convective heat transfer from an electrically conducting power-law fluid in the presence of a uniform magnetic field over a linearly vertically stretching sheet. Employing the modified Fourier's law, Sui *et al.* [13] scrutinized the effects of mixed convective heat transfer to the power-law fluid over a moving conveyor along the inclined plate. Naseer *et al.* [14] considered the power-law fluid over a vertical stretching cylinder and investigated the characteristics of mixed convective heat transfer numerically by employing the Fehlberg method.

Energy is required for the deformation and flow of materials. This mechanical energy is dissipated i.e., during the flow it is transformed into the material's internal energy. An increase of internal energy is then expressed as a rise in temperature. For the case of viscous fluids the viscous dissipation is always positive whereas for the elastic fluids it assumes positive or negative values. The effects of viscous dissipation being negligibly small were disregarded before Gebhart [15]. He showed that in natural convection critical viscous dissipation may happen in different gadgets which are liable to substantial deceleration or work at high rotation speeds. Further, he affirmed that paramount viscous dissipation impacts might likewise be available in processes in which the scale of the process is large, e.g., on larger planets, in huge masses of gas in space and in powerful gravitational fields. After that groundbreaking work viscous dissipation is investigated intensively by many researchers.



Chamkha *et al.* [16] presented numerical solution for the mixed convective heat and mass transfer from the power-law fluid saturated into a non-Darcian porous medium. Moreover, the chemical reaction effects and viscous dissipation are considered. Numerical solution by utilizing the Keller-Box method for the unsteady flow and heat transfer over a permeable stretching surface in a thin liquid film of the power-law fluid is studied by Vajravelu *et al.* [17]. The influence of non-uniform heat source for the upper convected Maxwell fluid over a stretching sheet with viscous dissipation is examined by Abel *et al.* [18]. The influence of non-linear velocity, temperature and magnetic field applied perpendicular to the plate is scrutinized numerically by Kishan and Kavitha [19] on the flow and heat transfer to the power-law fluid past a stretching plate when the viscous dissipation is taken into account. The boundary layer flow and heat transfer in third grade fluid over an unsteady permeable stretching sheet is addressed by Hayat *et al.* [20].

A stagnation flow means the fluid motion near the stagnation region exists on a solid body where the fluid moves towards it. The stagnation region encounters the highest pressure, the highest heat transfer and the highest rate of mass deposition. The investigation of the stagnation-point flow followed to Hiemenz [21] in 1911. He investigated the stagnation-point flow over a plate and exact solution of the Navier Stokes was determined by him. After that the combine effects of stretching and stagnation-point were studied by Chaim [22] by taking stretching and straining velocities equal. His findings indicated that no boundary layer exists close to the sheet. Afterwards by taking different stretching and straining velocities the Chaim's work was re-investigated by Mahapatra and Gupta [23] and their findings were quite interesting. They found two types of boundary layer structure close to the sheet

depending on the ratio of stretching and straining velocity rates. The pioneering work of above mentioned researchers was extended by many researchers [24 – 27].

The thermal radiation effects are of more importance when the temperature difference between the surface and the ambient fluid is larger. Also, the thermal boundary layer structure and hence the rate of heat transfer alter in the presence of thermal radiation at high operating temperature. Many investigations have been carried out in the recent past regarding thermal effects by applying the linearized form of Rosseland approximation considering non-Newtonian fluids, which is obtained by assuming sufficiently small temperature differences within the flow, including, Prasad and Vajravelu [28], Khan *et al.* [29], Samad and Saha [30], Kishan and Kavitha [31], Mathur *et al.* [32], Saritha *et al.* [33] and so forth. The non-linear Rosseland diffusion approximation is valid for small as well as large temperature difference of surface and ambient fluid, unlike the linearized Rosseland approximation which is valid only for sufficiently small temperature difference. Recently, the Rosseland diffusion approximation is adopted by various researchers while studying the non-linear radiative heat transfer to various non-Newtonian fluids including Hayat *et al.* [34], Ananth *et al.* [35], Sulochana *et al.* [36] and so forth.

Due to the growing demands of new technologies such as, microelectronics, chemical production and power station, there is a necessity to develop novel types of fluids which transfer heat more effectively. Heat transfer efficiency of working fluid can likewise be enhanced by increasing the thermal conductivity. In general commonly used heat transfer fluids (e.g. water, ethylene glycol, and engine oil) possess low thermal conductivities when contrasted with the thermal conductivity of solids. The addition of small particles of solids possessing high thermal conductivities to fluids

can enhance the thermal conductivity of the fluid. The practicality of the usage of such suspensions of solid particles was investigated by several researchers and huge points of interest were observed [37]. Researchers are permitted because of the recent advances in nanotechnology to study the next generation heat transfer nanofluids, a term first introduced by Choi [38]. Numerous sorts of liquids, such as water, ethylene glycol, engine oil, pump oil and glycerol have been used as host liquids in nanofluids. Whereas, nanoparticles used in nanofluids are of different materials having better thermal conductivity than base fluids. Owing to this, many researchers are persuaded and revolutionary work has been done by them. Khan and Gorla [39] determined the numerical solutions by employing the finite difference method for the flow and convective heat transfer to the power-law nanofluid in the presence of convective boundary conditions. Mat *et al.* [40] investigated theoretically the influence of thermal radiation on the mixed convective heat transfer in the power-law nanofluid past a vertical plate. Ibrahim and Makinde [41] considered the power-law nanofluid over a stretching sheet and studied the combined effects of MHD stagnation point flow and convective heating. Khan and Khan [42] considered the power-law nanofluid and investigated the heat and mass transfer while taking into account the new mass flux conditions. Mixed convective flow and heat transfer of the power-law nanofluid with convective surface/boundary conditions is explored by Hayat *et al.* [43].

There is an extensive variety of chemical reactions, a lot of which have important practical applications, which proceed only very slowly, or not at all, with the exception of in the vicinity of a catalyst. Some chemical reacting systems involve both homogeneous and heterogeneous reactions, with examples occurring in combustion, catalysis and biochemical systems. The interaction between the homogeneous reac-



tions in the bulk of fluid and the heterogeneous reactions occurring on some catalytic surface is generally extremely intricate, involving the production and consumption of reactant species at different rates both within the fluid and on the catalytic surface as well as the feedback on these reaction rates through temperature variations within the reacting fluid, which in turn modify the fluid motion. Chaudhary and Merkin [44] have proposed a straightforward model of the homogeneous–heterogeneous reactions for the forced convection boundary layer flow near the two-dimensional forward stagnation-point on a non-permeable infinite wall within which an isothermal cubic autocatalytic reaction takes place. They gave the formulation of homogeneous (bulk) reaction by isothermal cubic kinetics and the heterogeneous (surface) reaction by considering the first-order kinetics. Later, Chaudhary and Merkin [45] continued their previous work and included the effect of loss of autocatalyst. Recently, the effect of homogeneous–heterogeneous reactions on stagnation-point flow of a non-Newtonian fluid over a permeable stretching/shrinking sheet is studied by Sheikh and Abbas [46]. Raju *et al.* [47] studied theoretically the combined effects of induced magnetic field, non-uniform heat source/sink and homogeneous–heterogeneous reactions on the stagnation point flow of Casson fluid past a stretching sheet. Malik *et al.* [48] obtained the numerical solutions for the problem of homogeneous-heterogeneous reaction on Williamson fluid model past a linearly stretching cylinder in its axial direction. Hayat *et al.* [49] analytically studied the homogeneous–heterogeneous reactions on the flow of an Oldroyd-B fluid along with Cattaneo–Christov heat flux model. The impact of homogeneous–heterogeneous reactions on a stagnation point flow of viscoelastic fluid is discussed at length by Animasaun *et al.* [50] when the diffusion coefficients of chemical species are assumed to be unequal unlike the afore-

mentioned investigations.

The intension of this thesis is to improve upon the current understanding of the boundary layer flow and heat transfer characteristics of the Generalized Newtonian Fluid model. Within this thesis we will consider the Sisko fluid model. The focus of the present study is to investigate the heat transfer characteristics of the Sisko fluid flow past different moving surfaces in the presence of convective boundary conditions numerically as well as analytically for the integer and non-integer values of the power-law index .

1.1.2 The Structure of the Thesis

The present thesis possesses nine chapters investigating the heat transfer characteristics to the Sisko fluid over moving surfaces in the presence of the convective boundary conditions. Here, the moving surfaces are mainly considered of two types i.e., a stretching flat plate (Chapters 2 – 4) and a horizontal stretching cylinder (Chapters 5 – 8). The thesis is composed according to the plan as detailed below.

Chapter 1 comprises the historical background of the problems considered and the structure of the thesis.

We analyzed in **chapter 2** the flow and forced convective heat transfer to the Sisko fluid over a flat plate in the presence of convective boundary conditions. The flow is induced by the stretching plate with power-law velocity and a uniform transverse magnetic field. The arising governing equations are appeared to be partial differential equations. Instead of solving them directly, we have applied local-similar transformations on these equations and converted them into ordinary differential equations which are solved then numerically (i.e., by the shooting technique) and

analytically (i.e., by the homotopy analysis method). The exact solutions of these ordinary differential equations are also determined for some special cases. The impact of pertinent parameters involving in the problem is discussed on the velocity profile, temperature profile, local skin friction and local Nusselt number at length. The velocity and temperature fields are plotted for the integer as well as non-integer values of the power-law index n . At the end, a comparison between analytical, numerical and exact solutions is made to affirm the validity of the obtained analytical results. This investigation has been published in “**PLoS ONE (2014) 9(10): e107989. doi: 10.1371/journal.pone.0107989**”.

Devotion of **chapter 3** is to scrutinize the influence of non-linearly radially stretching flat plate on MHD axisymmetric flow and convective heat transfer in Sisko fluid, when taking into account the convective boundary conditions as well. The problem under consideration is appeared to be governed by very complicated partial differential equations which are simplified by the application of usual boundary layer approximations. Implementation of the local-similarity transformations reduced the independent variables by one and hence the governing equations take the form of ordinary differential equations. The non-linear coupled set of ordinary differential equations is solved analytically to obtain series solution by the homotopy analysis method for the integer values of the power-law index and numerically by shooting technique for non-integer values of the power-law index. For some special cases the exact solutions are also obtained. In the graphical and tabular form the behavior of velocity, temperature, local skin friction and local nusselt number is presented. Moreover, the analytical, numerical and exact solutions are compared graphically to ensure authenticity of analytical results. Also, in tabular form the



analytical and exact solutions are matched very well. The work of this chapter has been published in “**Journal of the Brazilian Society of Mechanical Sciences and Engineering (2016) 38:1279-1289, doi: 10.1007/s40430-015-0437-y**”.

Chapter 4 is actually an extension of the chapter 3 by considering instead of forced convection, the mixed convective heat transfer over an impermeable radially stretching sheet along with the convective boundary conditions. Also, the viscous dissipation and the thermal radiation effects are taken into account. The local-similarity transformations are employed to transform the governing partial differential equations into non-linear coupled ordinary differential equations. The analytical and numerical results obtained by solving the governing equations, the velocity, temperature, local skin friction and local Nusselt number are presented in graphical and tabular form. The velocity and temperature profiles are discussed at length for assisting and opposing flows for various values of the parameters involved in the problem. The obtained analytical results are proved valid by giving a graphical comparison between them and numerical results as well as comparing them with the previously reported results in the literature. The results of the present work are published in “**AIP Advances 5, 087178 (2015); doi: 10.1063/1.4929832**”.

The numerical analysis of heat transfer in an electrically conducting Sisko fluid past a moving surface is carried out when taking into account the effects of a transverse magnetic field, viscous dissipation and convective boundary conditions and presented in **chapter 5**. The moving surface is specifically assumed to be a horizontal linearly stretching cylinder in its axial direction. The results of this underlying non-linear problem is mainly developed by the shooting technique for the non-integer values of the power-law index n . Also, the analytic results for the same problem are

computed by using the homotopy analysis method for comparison which leads to the authenticity of the obtained numerical results. For the shear thinning fluid (i.e., $n = 0.5$) and shear thickening fluid (i.e., $n = 1.5$) the velocity, temperature, local skin friction and local Nusselt number are discussed in detail. The aforementioned work has been published in “**AIP Advances 5, 127202 (2015); doi: 10.1063/1.4937346**”.

Chapter 6 focused on the radiative heat transfer towards the stagnation-point flow of Sisko fluid past an impermeable stretching cylinder. The convective boundary conditions are taken into account as well. By utilizing the non-linear Rosseland approximation a term representing the radiative heat flux was introduced in the energy equation. The numerical solution of the locally similar coupled non-linear differential equations is determined by utilizing the shooting method. The results are compared for the flow over a flat plate and the flow over a cylinder for shear thinning and thickening fluids for various values of emerging parameters. The validation of the present work is affirmed by comparing these results with the analytic results obtained by the homotopy analysis method. This piece of work is recently published in “**AIP Advances 6, 055315 (2016); doi: 10.1063/1.4950946**”.

Chapter 7 deals with the combined effects of variable thermal conductivity and convective boundary conditions on the flow and heat transfer past a stretching cylinder immersed in the Sisko nanofluid. Here, the nanoparticle concentration is characterized by the new mass flux conditions which physically describes that nanoparticle flux at the boundary is zero. Also, due to these conditions the effect of the Brownian motion at the temperature is negligible. The obtained numerical solutions by the shooting method are plotted for several parameters corresponding to flow over a flat plate and a cylinder. The behavior of the shear thinning and shear thickening fluids

is compared. The validation of numerical results is ensured by comparing them with the analytic results. Here, the Sherwood number is identically zero whereas, the Nusselt number is given in tabular form. These observations have been published in “**Journal of Molecular Liquids 218 (2016) 1-7**”.

Chapter 8 concentrates on the homogeneous-heterogeneous reactions on the stagnation-point flow of Sisko fluid past a non-linearly stretching cylinder along with convective boundary conditions. Here, the diffusion coefficients of species of kinds A and B are assumed to be of comparable size and the released heat amid the process is considered negligible. The governing partial differential equations are transformed into a set of non-linear ordinary differential equations by using appropriate local-similarity transformations. These coupled set of equations are solved numerically by employing the shooting technique. These results for the velocity, temperature and concentration profiles are plotted graphically and the local skin friction and Nusselt number are presented in tabular form. At the end, the numerical results are compared with the analytical results and found in good agreement. The contents of this chapter are submitted for publication in “Scientific Reports”.

Ultimately, the aim of **chapter 9** is to conclude the major findings and contributions of the research of the entire thesis. Possible future directions to continue this work are also briefly highlighted.

Chapter 2

Flow and Heat Transfer in Sisko Fluid with Convective Boundary Conditions

In this chapter, we have scrutinized the steady boundary layer flow and heat transfer in Sisko fluid with convective boundary conditions over a non-isothermal stretching sheet. The flow is induced by non-linearly stretching sheet in the presence of a uniform transverse magnetic field. The partial differential equations governing the problem have been reduced by suitable transformations into the ordinary differential equations. The transformed partially coupled non-linear ordinary differential equations are then solved analytically by using the homotopy analysis method (HAM) and numerically by the shooting technique along with the Runge-Kutta method. In addition, exact analytical solutions are presented in some possible limiting cases. Effects of different parameters like power-law index n , magnetic parameter D , stretching parameter s , generalized Prandtl number Pr and generalized Biot number γ are presented graphically. It is found that the temperature profile increases with increasing value of D and γ whereas it decreases for Pr . Numerical values of the local skin-friction coefficient and local Nusselt number are tabulated at various physical situations. Additionally, a comparison of the obtained numerical results with the

HAM and exact solutions is made. An excellent agreement between these results enhances our confidence in the HAM solutions.

2.1 Mathematical Formulation

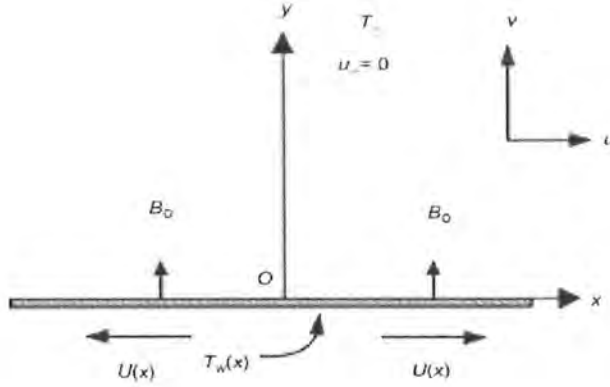


Figure 2.1: Schematic diagram of the problem.

2.1.1 Governing Equations

It is appropriate to adopt the physical laws of conservation for real flow situations. The application of these laws of conservation of mass, linear momentum and energy give rise to the basic equations describing an incompressible flow, namely, the continuity, momentum and energy equations, which are defined as follows:

$$\nabla \cdot \mathbf{V} = 0, \quad (2.1)$$

$$\rho \left[\frac{\partial \mathbf{V}}{\partial t} + (\mathbf{V} \cdot \nabla) \mathbf{V} \right] = \nabla \cdot \boldsymbol{\tau} + \rho \mathbf{B}, \quad (2.2)$$

$$\rho c_p \left[\frac{\partial T}{\partial t} + (\mathbf{V} \cdot \nabla) T \right] = \boldsymbol{\tau} \cdot \mathbf{L} - \nabla \cdot \mathbf{q} - \nabla \cdot \mathbf{q}_r, \quad (2.3)$$

where \mathbf{V} is the velocity field, ρ the density of the fluid, $\boldsymbol{\tau}$ the Cauchy stress tensor, \mathbf{B} the body force per unit mass, c_p the specific heat at constant pressure, T the fluid temperature, $\mathbf{q} = -k\nabla T$ the thermal heat flux with k as the thermal conductivity, \mathbf{q}_r the radiative heat flux and \mathbf{L} the velocity gradient.

For the Sisko fluid which is a combination of the Newtonian fluid and power-law fluids the Cauchy stress tensor $\boldsymbol{\tau}$ is defined as follows:

$$\boldsymbol{\tau} = -\nabla p + \mathbf{S}, \quad (2.4)$$

$$\mathbf{S} = \left[a + b \left| \sqrt{\frac{1}{2} \text{tr}(\mathbf{A}_1)^2} \right|^{n-1} \right] \mathbf{A}_1, \quad (2.5)$$

with $\mathbf{A}_1 = \mathbf{L} + \mathbf{L}^\top$ the first Rivlin-Ericksen tensor, p the pressure and \mathbf{S} the extra stress tensor. Further, in the above expressions, a , b and n (≥ 0) are the material constants of the Sisko fluid representing the viscosity at high shear rate, consistency index and power-law index, respectively.

For the steady, two-directional and incompressible flow we assume the velocity, temperature and stress fields of the following forms

$$\mathbf{V} = [u(x, y), v(x, y), 0], \quad T = T(x, y), \quad \mathbf{S} = \mathbf{S}(x, y). \quad (2.6)$$

By using Eq. (2.6), the equation of continuity, momentum and energy in the absence of the viscous dissipation and radiative heat flux are given by

$$\frac{\partial u}{\partial x} + \frac{\partial v}{\partial y} = 0, \quad (2.7)$$



$$\rho \left(u \frac{\partial u}{\partial x} + v \frac{\partial u}{\partial y} \right) = -\frac{\partial p}{\partial x} + \frac{\partial S_{xx}}{\partial x} + \frac{\partial S_{xy}}{\partial y}, \quad (2.8)$$

$$\rho \left(u \frac{\partial v}{\partial x} + v \frac{\partial v}{\partial y} \right) = -\frac{\partial p}{\partial y} + \frac{\partial S_{yx}}{\partial x} + \frac{\partial S_{yy}}{\partial y}, \quad (2.9)$$

$$\rho c_p \left(u \frac{\partial T}{\partial x} + v \frac{\partial T}{\partial y} \right) = k \left(\frac{\partial^2 T}{\partial x^2} + \frac{\partial^2 T}{\partial y^2} \right), \quad (2.10)$$

where (x, y) denotes the Cartesian coordinates, u and v are the velocity components along x - and y - directions, respectively. Also, the components of extra stress tensor \mathbf{S} defined by Eq. (2.5) can be expressed as

$$S_{xx} = \left[a + b \left| 2 \left(\frac{\partial u}{\partial x} \right)^2 + 2 \left(\frac{\partial v}{\partial y} \right)^2 + \left(\frac{\partial u}{\partial y} + \frac{\partial v}{\partial x} \right)^2 \right|^{\frac{n-1}{2}} \right] \left(2 \frac{\partial u}{\partial x} \right), \quad (2.11)$$

$$S_{xy} = S_{yx} = \left[a + b \left| 2 \left(\frac{\partial u}{\partial x} \right)^2 + 2 \left(\frac{\partial v}{\partial y} \right)^2 + \left(\frac{\partial u}{\partial y} + \frac{\partial v}{\partial x} \right)^2 \right|^{\frac{n-1}{2}} \right] \left(\frac{\partial u}{\partial y} + \frac{\partial v}{\partial x} \right), \quad (2.12)$$

$$S_{yy} = \left[a + b \left| 2 \left(\frac{\partial u}{\partial x} \right)^2 + 2 \left(\frac{\partial v}{\partial y} \right)^2 + \left(\frac{\partial u}{\partial y} + \frac{\partial v}{\partial x} \right)^2 \right|^{\frac{n-1}{2}} \right] \left(2 \frac{\partial v}{\partial y} \right), \quad (2.13)$$

with $S_{xz} = S_{zx} = S_{yz} = S_{zy} = S_{zz} = 0$.

Upon using the usual boundary layer approximations after the substitution of expressions defined by Eqs. (2.11) – (2.13), Eqs. (2.8) – (2.10) take the form

$$u \frac{\partial u}{\partial x} + v \frac{\partial u}{\partial y} = -\frac{1}{\rho} \frac{\partial p}{\partial x} + \frac{a}{\rho} \frac{\partial^2 u}{\partial y^2} + \frac{b}{\rho} \frac{\partial}{\partial y} \left(\frac{\partial u}{\partial y} \left| \frac{\partial u}{\partial y} \right|^{n-1} \right), \quad (2.14)$$

$$0 = -\frac{\partial p}{\partial y}, \quad (2.15)$$

$$\rho c_p \left(u \frac{\partial T}{\partial x} + v \frac{\partial T}{\partial y} \right) = k \left(\frac{\partial^2 T}{\partial y^2} \right). \quad (2.16)$$

2.1.2 Flow Equations

Let us consider the steady, laminar and incompressible flow of Sisko fluid over an isothermal flat sheet. The sheet is stretching with non-linear velocity $U(x) = cx^s$, where c and s are non-negative real numbers. A uniform transverse magnetic field $\mathbf{B} = [0, B_0, 0]$ is applied under the assumption of very small magnetic Reynolds number. Under these assumptions the governing momentum equation for two-dimensional boundary layer flow of Sisko fluid can be expressed as (see ref. [51] for details)

$$u \frac{\partial u}{\partial x} + v \frac{\partial u}{\partial y} = \frac{a}{\rho} \frac{\partial^2 u}{\partial y^2} - \frac{b}{\rho} \frac{\partial}{\partial y} \left(-\frac{\partial u}{\partial y} \right)^n - \frac{\sigma B_0^2}{\rho} u, \quad (2.17)$$

where a , b and n (≥ 0) are the material constants, σ the electrical conductivity of the fluid, ρ the fluid density and B_0 the magnitude of applied magnetic field.

The flow is subject to the following boundary conditions

$$u(x, y) = U = cx^s, \quad v(x, y) = 0 \quad \text{at } y = 0, \quad (2.18)$$

$$u \rightarrow 0 \quad \text{as } y \rightarrow \infty. \quad (2.19)$$

Introducing the transformations [51] as

$$\eta = \frac{y}{x} \text{Re}_b^{\frac{1}{n+1}}, \quad \psi = Ux \text{Re}_b^{-\frac{1}{n+1}} f(\eta), \quad (2.20)$$

with

$$u(x, y) = U f'(\eta), \quad (2.21)$$

$$v(x, y) = -U \text{Re}_b^{-\frac{1}{n+1}} \frac{1}{n+1} [\{s(2n-1)+1\} f(\eta) + \{s(2-n)-1\} \eta f'(\eta)], \quad (2.22)$$

where ψ is the Stokes stream function.

After simplification we reach at the following problem

$$A f''' + n (-f'')^{n-1} f''' + \frac{s(2n-1)+1}{n+1} f f'' - s (f')^2 - D^2 f' = 0, \quad (2.23)$$

$$f(0) = 0, \quad f'(0) = 1, \quad f'(\infty) = 0, \quad (2.24)$$

where

$$D^2 = \frac{\sigma B_0^2}{\rho U} x, \quad A = \frac{\text{Re}_b^{\frac{2}{n+1}}}{\text{Re}_a}, \quad \text{Re}_a = \frac{\rho x U}{a} \quad \text{and} \quad \text{Re}_b = \frac{\rho x^n U^{2-n}}{b}, \quad (2.25)$$

are the non-dimensional quantities.

The significant quantity of interest from engineering point of view is the local skin-friction coefficient C_{fx} defined by [52]

$$C_{fx} = \frac{\tau_{xy}|_{y=0}}{\frac{1}{2} \rho U^2}, \quad (2.26)$$

where τ_{xy} the wall shear stress is given as

$$\tau_{xy} = \left(a + b \left| \frac{\partial u}{\partial y} \right|^{n-1} \right) \frac{\partial u}{\partial y}. \quad (2.27)$$

Upon substitution of Eq. (2.27) into Eq. (2.26) along with Eq. (2.20) the



dimensionless form of the local skin friction coefficient appears as follows:

$$\frac{1}{2} \text{Re}_b^{\frac{1}{n+1}} C_{fx} = Af''(0) - [-f''(0)]^n. \quad (2.28)$$

2.1.3 Heat Transfer Analysis

The thermal energy equation after the application of usual boundary layer approximations in the absence of heat source and dissipation with convective boundary conditions at the wall is given as

$$u \frac{\partial T}{\partial x} + v \frac{\partial T}{\partial y} = \alpha \frac{\partial^2 T}{\partial y^2}, \quad (2.29)$$

$$k \frac{\partial T(x, 0)}{\partial y} = -h_f [T_f - T(x, 0)], \quad (2.30)$$

$$T \rightarrow T_\infty \quad \text{as } y \rightarrow \infty, \quad (2.31)$$

where $T = T(x, y)$ is the temperature field, k the thermal conductivity, $\alpha = \frac{k}{\rho c_p}$ the thermal diffusivity, T_f the temperature of the hot fluid below the sheet, h_f the heat transfer parameter and T_∞ the ambient temperature of the fluid.

We introduce the non-dimensional scaled temperature θ as

$$\theta(\eta) = \frac{T - T_\infty}{T_f - T_\infty}. \quad (2.32)$$

In view of Eqs. (2.20) and (2.32), Eq. (2.29) takes the form

$$\theta'' + \frac{s(2n-1)+1}{n+1} \text{Pr} f \theta' = 0, \quad (2.33)$$



and transformed boundary conditions are

$$\theta'(0) = -\gamma [1 - \theta(0)], \quad \theta(\eta) \rightarrow 0 \quad \text{as } \eta \rightarrow \infty, \quad (2.34)$$

where prime denotes differentiation with respect to independent variable η , Pr the generalized Prandtl number and γ the generalized Biot number and are given by

$$\text{Pr} = \frac{xU}{\alpha} \text{Re}_b^{-\frac{2}{n+1}}, \quad \gamma = \frac{h_f}{k} x \text{Re}_b^{-\frac{1}{n+1}}. \quad (2.35)$$

The local Nusselt number Nu_x may be found in terms of the dimensionless temperature at the wall surface, $\theta'(0)$, that is

$$\text{Re}_b^{-\frac{1}{n+1}} Nu_x = -\theta'(0), \quad (2.36)$$

with $Nu_x = \frac{xq_w}{\kappa(T_f - T_\infty)}$ and q_w as the surface heat flux.

2.2 Solution Methodologies

2.2.1 The Homotopy Analytic Solution

The homotopy analysis method (HAM) is employed to solve non-linear governing Eqs. (2.23) and (2.33) subject to the boundary conditions (2.24) and (2.34). The analytic solutions are obtained for the velocity and temperature fields by considering the initial guesses and linear operators of the forms defined as follows:

$$f_0(\eta) = 1 - e^{-\eta}, \quad \theta_0(\eta) = \frac{\gamma e^{-\eta}}{1 + \gamma}, \quad (2.37)$$

$$\mathcal{L}_f = \frac{d^3}{d\eta^3} - \frac{d}{d\eta}, \quad \mathcal{L}_\theta = \frac{d^2}{d\eta^2} - 1. \quad (2.38)$$

The convergence of these series solutions is highly dependent on the value of the auxiliary parameter \hbar . To determine the range of acceptable values of the auxiliary parameter \hbar the idea of \hbar -curve was introduced. Recently, the concept of minimized squared residual error [53] was introduced which provides only most suitable value of the auxiliary parameter \hbar instead of picking any random value from the range of values obtained by \hbar -curve. The formula for squared residual error is given by

$$E_{f,m} = \frac{1}{N+1} \sum_{j=0}^N \left[N_f \left(\sum_{i=0}^m f_j(i\Delta\eta) \right) \right]^2. \quad (2.39)$$

Table 2.1 elucidates the convergence of the series solution. It shows that the convergence is achieved at 25th approximation in the mentioned case. Further, the same criteria is adopted to achieve the convergence in other cases.

Table 2.1: The convergence of the homotopy solutions when $n = D = A = \gamma = Pr = 1$ and $s = 0.5$ are fixed.

Order of approximation	$-f''(0)$	$-\theta'(0)$
1	0.863726	0.463171
5	0.871058	0.448468
10	0.871684	0.451261
15	0.871686	0.450955
21	0.871686	0.450998
25	0.871686	0.450995
30	0.871686	0.450995

2.2.2 The Numerical Solution

Finding the exact analytical solutions corresponding to the set of highly non-linear coupled differential Eqs. (2.23) and (2.33) with conditions (2.24) and (2.34), constituting a two-point boundary value problem, is really a very difficult and sometimes nearly impossible task. So, to overcome this problem a numerical solution is obtained by using the shooting technique combined with Runge-Kutta forth order method. For this purpose the two-point boundary value problem is converted into a set of first order ordinary differential equations by introducing new variables y_1, y_2, y_3, y_4, y_5 as follows:

$$y'_1 = y_2, \quad y'_2 = y_3, \quad y'_3 = \frac{-1}{A + n(-y_3)^{n-1}} \left[\frac{s(2n-1)+1}{n+1} y_1 y_3 - s(y_2)^2 - D^2 y_2 \right], \quad (2.40)$$

$$y'_4 = y_5, \quad y'_5 = -\frac{s(2n-1)+1}{n+1} \text{Pr} y_1 y_5, \quad (2.41)$$

with initial conditions

$$f(0) = 0, \quad f'(0) = 1, \quad f''(0) = s_1, \quad \theta(0) = s_2, \quad \theta'(0) = -\gamma[1 - \theta(0)], \quad (2.42)$$

where s_1 and s_2 are determined using the shooting technique. The set of initial value problem is then solved by using Runge-Kutta forth order method.

2.2.3 The Exact Solution for Particular Cases

In this section, we endeavor to present the exact analytical solutions for the velocity and temperature fields in some possible limiting cases. These novel solutions are much valuable since they represented a rare class of exact solutions to the boundary

layer equations for the considered flow configuration.

Case (i): As a special case of the problem for $n = 0$ and $s = 0.5$, Eqs. (2.23)

and (2.33) reduce to

$$2Af''' + ff'' - (f')^2 - 2D^2f' = 0, \quad (2.43)$$

and

$$\theta'' + \frac{\text{Pr}}{2}f\theta' = 0. \quad (2.44)$$

The exact solutions of the above equations satisfying the boundary conditions (2.24) and (2.34) are

$$f(\eta) = \frac{1}{\beta} (1 - e^{-\beta\eta}), \quad (2.45)$$

$$\theta(\eta) = \frac{2^{\frac{\text{Pr}}{2\beta^2}} e^{\frac{\text{Pr}}{2\beta^2}} \gamma \left[\Gamma \left(\frac{\text{Pr}}{2\beta^2}, 0 \right) - \Gamma \left(\frac{\text{Pr}}{2\beta^2}, \frac{\text{Pr}}{2\beta^2} e^{-\beta\eta} \right) \right]}{\beta \left(\frac{\text{Pr}}{\beta^2} \right)^{\frac{\text{Pr}}{2\beta^2}} + 2^{\frac{\text{Pr}}{2\beta^2}} e^{\frac{\text{Pr}}{2\beta^2}} \gamma \left[\Gamma \left(\frac{\text{Pr}}{2\beta^2}, 0 \right) - \Gamma \left(\frac{\text{Pr}}{2\beta^2}, \frac{\text{Pr}}{2\beta^2} \right) \right]}, \quad (2.46)$$

where $\beta = \sqrt{\frac{1+2D^2}{2A}}$ and $\Gamma(\cdot)$ the incomplete Gamma function.

Case (ii): Now for $n = 1$ and $s = 1$, Eqs. (2.23) and (2.33) become

$$(1 + A) f''' + ff'' - (f')^2 - D^2f' = 0, \quad (2.47)$$

and

$$\theta'' + \text{Pr}f\theta' = 0, \quad (2.48)$$

which possess the exact analytical solutions of the form

$$f(\eta) = \frac{1}{\beta} (1 - e^{-\beta\eta}), \quad (2.49)$$

$$\theta(\eta) = \frac{e^{\frac{\text{Pr}}{\beta^2}\gamma} \left[\Gamma\left(\frac{\text{Pr}}{\beta^2}, 0\right) - \Gamma\left(\frac{\text{Pr}}{\beta^2}, \frac{\text{Pr}}{\beta^2} e^{-\beta\eta}\right) \right]}{\beta \left(\frac{\text{Pr}}{\beta^2}\right)^{\frac{\text{Pr}}{\beta^2}} + e^{\frac{\text{Pr}}{\beta^2}\gamma} \left[\Gamma\left(\frac{\text{Pr}}{\beta^2}, 0\right) - \Gamma\left(\frac{\text{Pr}}{\beta^2}, \frac{\text{Pr}}{\beta^2}\right) \right]}, \quad (2.50)$$

when satisfying the boundary conditions (2.24) and (2.34) with $\beta = \sqrt{\frac{1+D^2}{1+A}}$.

2.3 Numerical Results and Discussion

In order to get definite perception of the physical problem, velocity profile $f'(\eta)$ and temperature profile $\theta(\eta)$ are displayed graphically for different values of the power-law index n , magnetic parameter D , stretching parameter s , generalized Prandtl number Pr and generalized Biot number γ appearing in the problem. The coupled set of Eqs. (2.23) and (2.33) with the boundary conditions (2.24) and (2.34) are solved analytically by means of the HAM and numerical solutions are obtained using the shooting technique along with forth-order Runge-Kutta method. The results of the numerical solutions for non-integer power-law index n are shown in figures 1 and 3 whereas the rest of the figures present the HAM results. Further, it is possible in some special cases to compare the results obtained by the HAM with exact solutions. Moreover, representative results for the local skin-friction coefficient and local Nusselt number illustrating the influence of various physical parameters of the flow are recorded through tables. In this entire chapter we considered $s = \text{Pr} = 0.5$, $A = \gamma = 1$ and $D = 1$ as common except the variations in the corresponding graphs and tables.

Figures 2.2 (a, b) delineate the influence of the power-law index n on velocity profile $f'(\eta)$. From these figures, it is observed that an increase in the values of n



decreases the velocity profile and hence the corresponding boundary layer thickness for power index $n \geq 1$ (i.e., for shear thickening and Newtonian fluids) whereas for $n < 1$ (i.e., shear thinning fluid) we notice two different behaviors, i.e., close to the sheet the velocity profile increases while it decreases away from the sheet with the increase of the power-law index n .

In order to illustrate the influence of the magnetic parameter D on velocity profile $f'(\eta)$ we have plotted figures 2.3 (a-d) for the power-law index $n = 0, 1, 2$ and 3. It appears from these figures that an increase in value of the magnetic parameter D decreases the velocity profile due to resistance force generated by the magnetic field. Also, we can notice that effect of the magnetic parameter D becomes less dominating as we increase value of the power-law index n and the corresponding boundary layer thickness decreases with the increase of D too. Further, these figures portray that the momentum boundary layer thickness becomes thin as we decrease the power-law index n . Moreover, these figures provide a comparison that the magnitude of velocity is larger for hydrodynamic case ($D = 0$) when compared with hydromagnetic case ($D \neq 0$).

Figures 2.4 (a-d) portray the effects of the magnetic parameter D on temperature profile $\theta(\eta)$. It is clear from these figures that the temperature profile increases with an increase of D . However, we can observe that the temperature profile is not very much sensitive to the magnetic parameter D .

Figures 2.5 (a-d) present the temperature profile $\theta(\eta)$ for different values of the stretching parameter s . We can notice from these figures that the stretching parameter has quite opposite effect on the temperature profile for $n = 0$ and $n = 1, 2, 3$. We can see that with an increase in the stretching parameter s the temperature profile

increases for $n = 0$, while for $n = 1, 2, 3$ it decreases. Further, with the increase in s the thermal boundary layer thickness increases for $n = 0$ and decreases for $n = 1, 2, 3$.

The variation of the generalized Prandtl number Pr on the temperature profile $\theta(\eta)$ is shown in figures 2.6 (a-d). It is worth noting that with the increase of Pr the temperature profile decreases. That is, an increase in generalized Prandtl number Pr represents a decrease in the thermal conductivity which as a result reduces the thermal boundary layer thickness. Additionally, it can be observed that the power-law index n plays a significant role. An increase in the power-law index n results in thinning of the thermal boundary layer.

The effect of the generalized Biot number γ on the temperature profile $\theta(\eta)$ is shown by figures 2.7 (a-d). These figures put in evidence that the effect of increasing the generalized Biot number γ is to enlarge both the temperature and thermal boundary layer thickness significantly, since increasing values of γ shows the decreasing thermal resistance of the wall and hence convective heat transfer to the fluid increases.

Figures 2.8 (a, b) correspond to the power-law index $n < 1$ and $n \geq 1$, respectively. From these figures, it is obvious that the temperature profile decreases with increase in the power-law index n . Further, these figures indicate that for a given location η , $\theta(\eta)$ decreases as the power-law index n increases, resulting in a decrease of the thermal boundary layer thickness. We can also observe that more significant effects can be seen for values of the power-law index $n < 1$, while it has small effects for the power-law index $n \geq 1$.

Figures 2.9 (a, b) and 2.10 (a, b) present a comparison between the exact, numerical and HAM solutions. These figures show that an excellent agreement between the

results exists. This leads a confidence in the HAM results reported in this section.

The numerical values of the local skin friction coefficient $\frac{1}{2} \text{Re}_b^{\frac{1}{n+1}} C_f$ and the local Nusselt number $\text{Re}_b^{-\frac{1}{n+1}} Nu_x$ for different values of A , D , s , Pr and γ are listed in tables 2.2 and 2.3. Table 2.2 shows that magnitude of the local skin friction coefficient increases for larger values of A , D and s . Table 2.3 depicts that the local Nusselt number increases for larger values of A , Pr , γ while it has opposite behavior for D for different values of the power-law index n . By increasing the stretching parameter s we observe that for $n = 0$, the local Nusselt number decreases while for $n = 1, 2$ and 3 it increases.

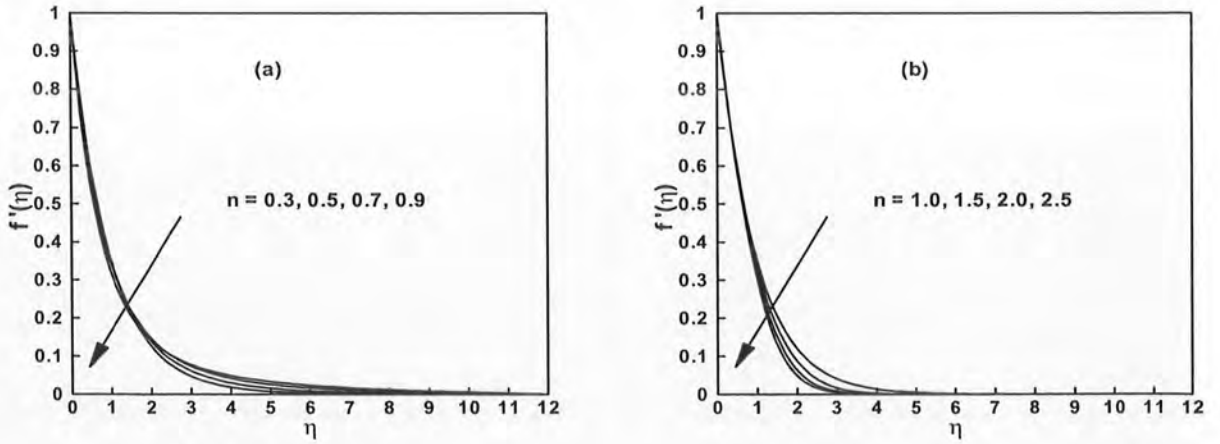


Figure 2.2: The velocity profiles $f'(\eta)$ for different values of the power-law index n .

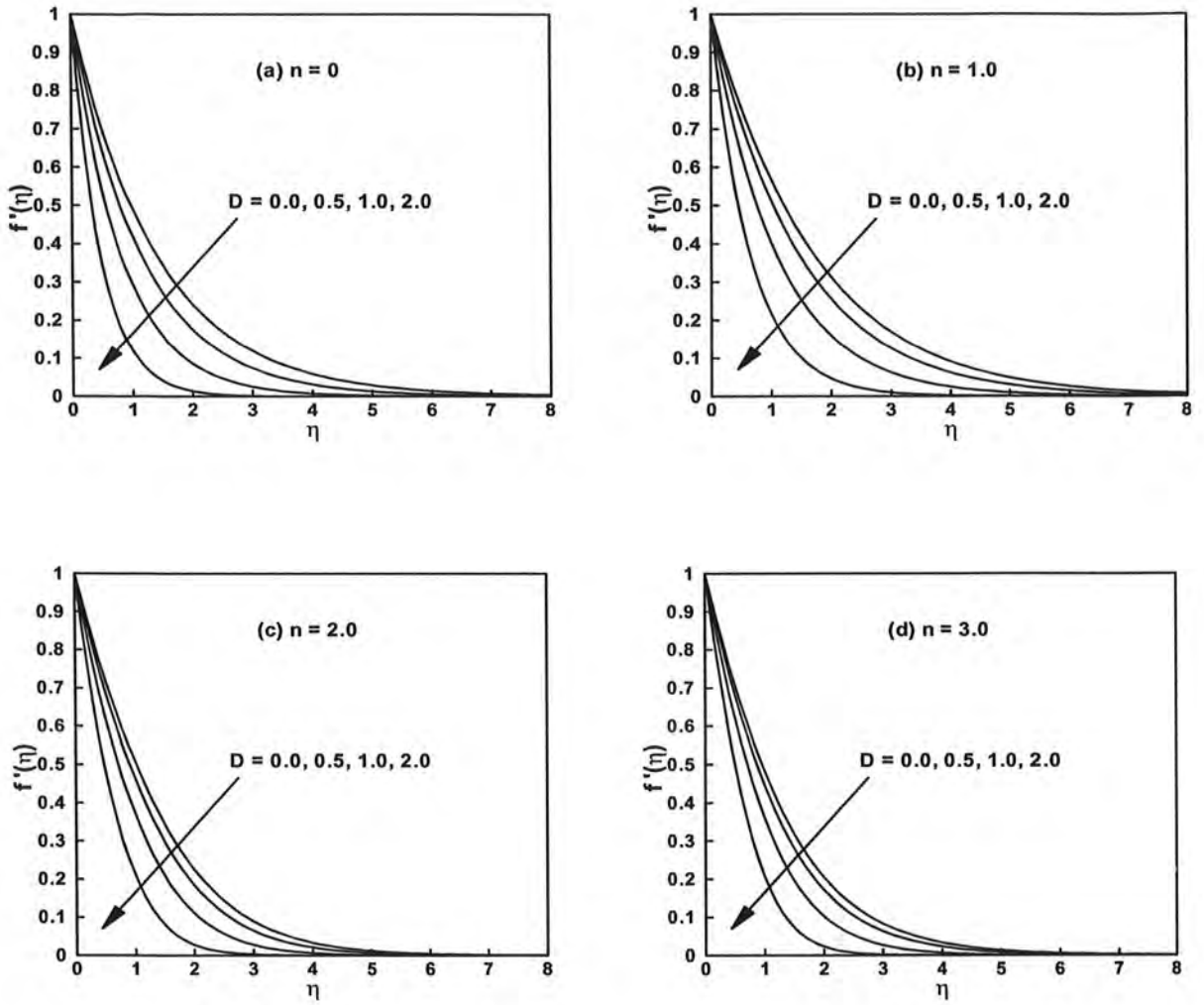


Figure 2.3: The velocity profiles $f'(\eta)$ for different values of the magnetic parameter

D .



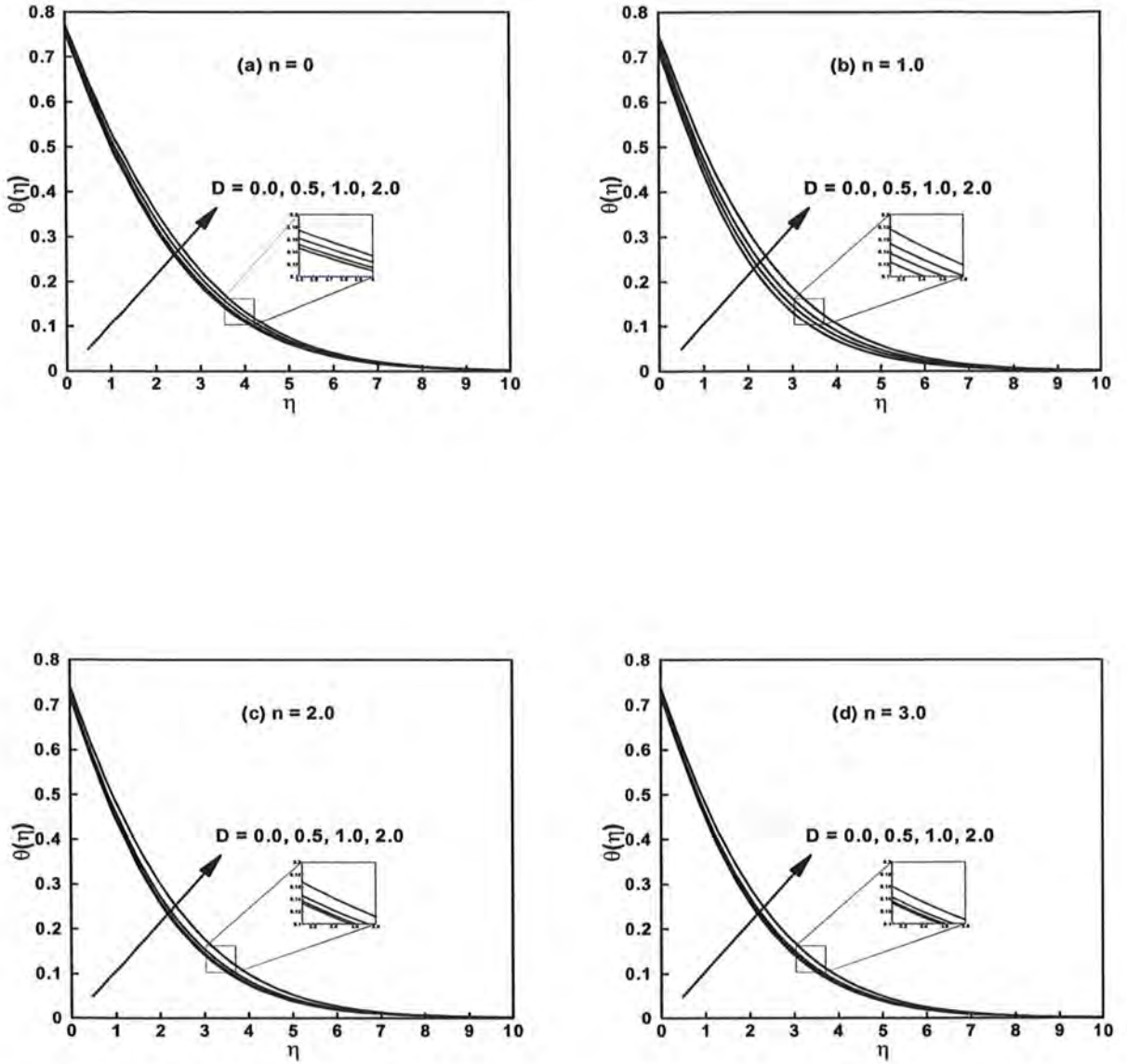


Figure 2.4: The temperature profiles $\theta(\eta)$ for different values of the magnetic parameter D .



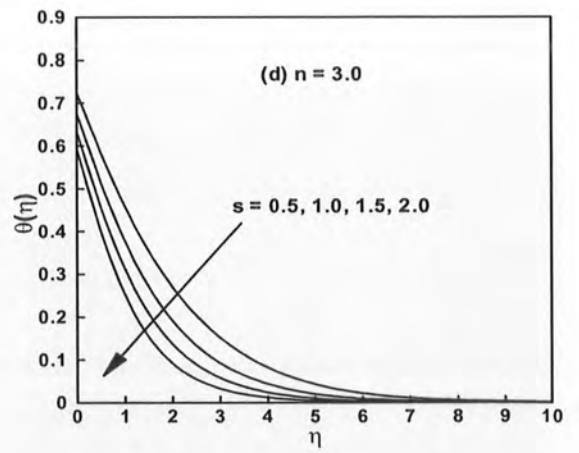
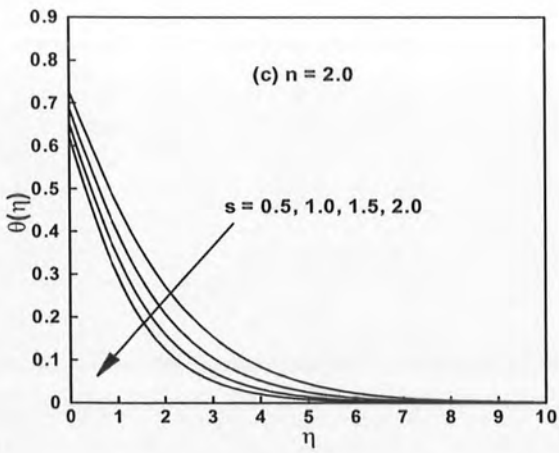
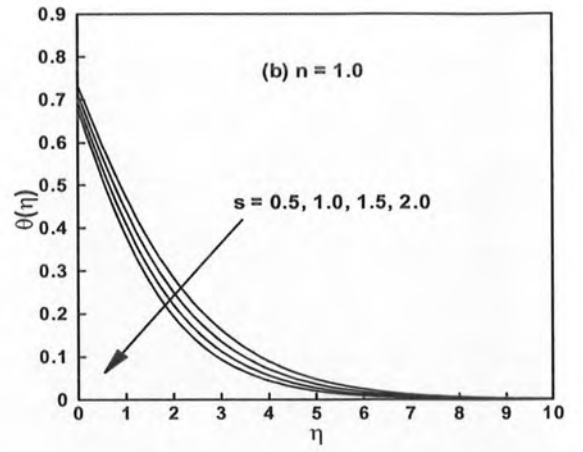
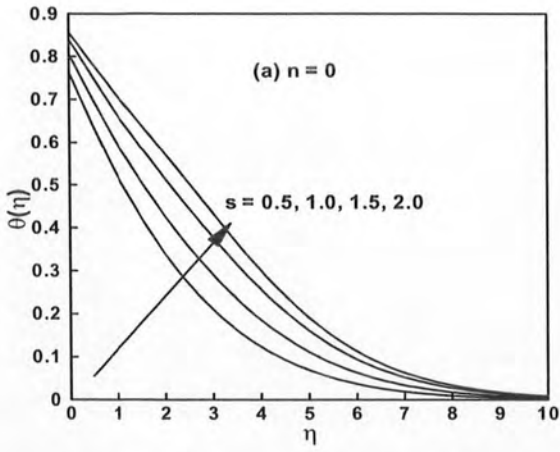


Figure 2.5: The temperature profiles $\theta(\eta)$ for different values of the stretching parameter s .

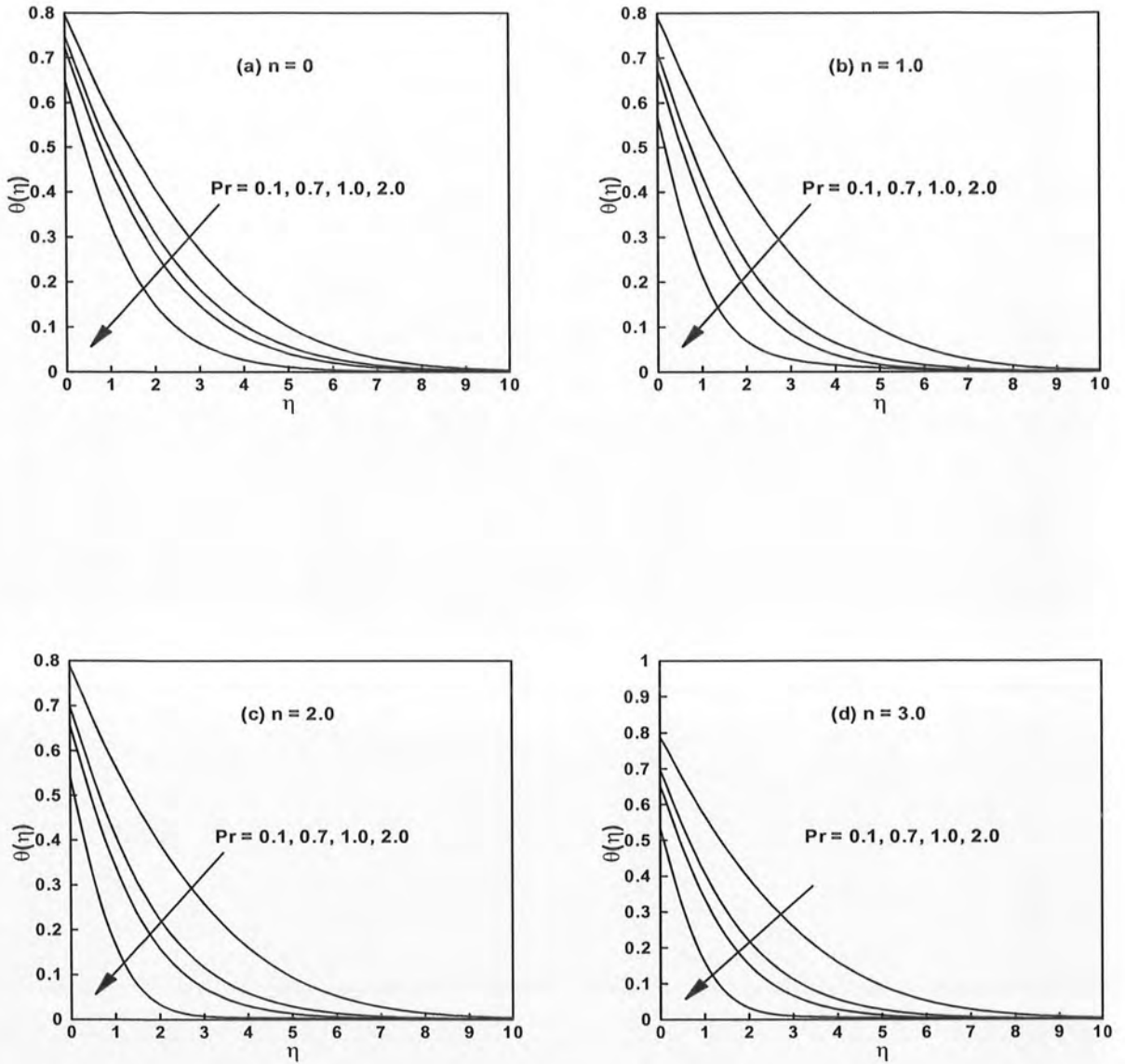


Figure 2.6: The temperature profiles $\theta(\eta)$ for different values of the generalized Prandtl number Pr .

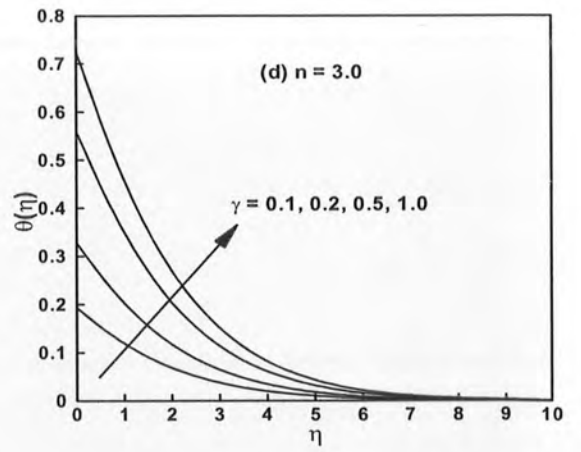
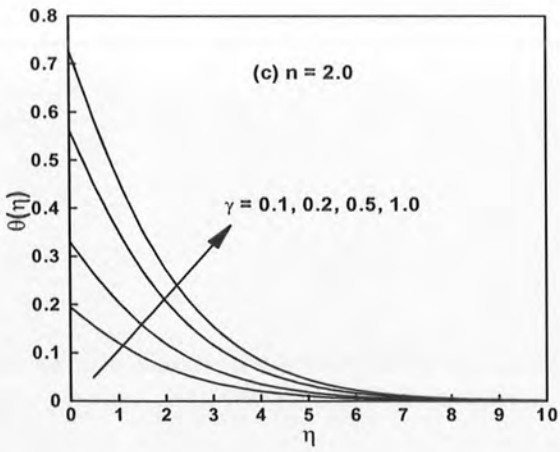
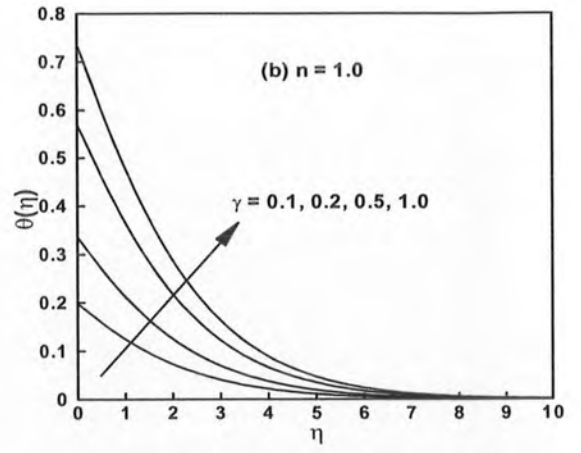
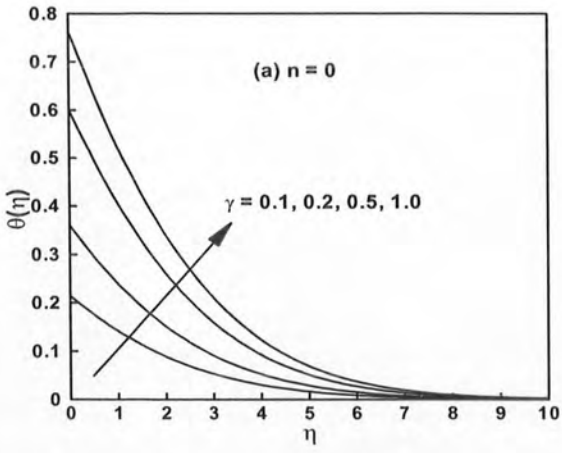


Figure 2.7: The temperature profiles $\theta(\eta)$ for different values of the generalized Biot number γ .

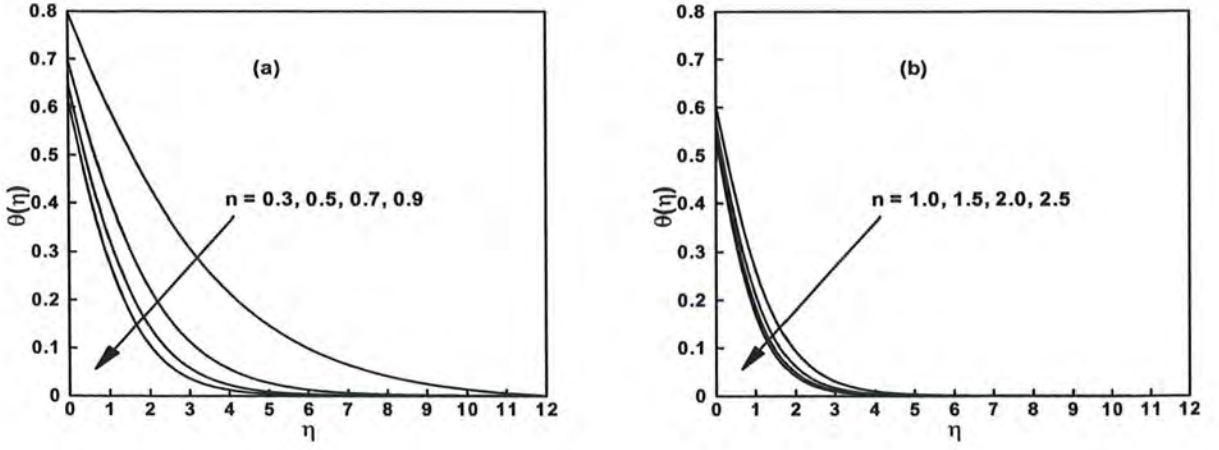


Figure 2.8: The temperature profiles $\theta(\eta)$ for different values of the power-law index n .

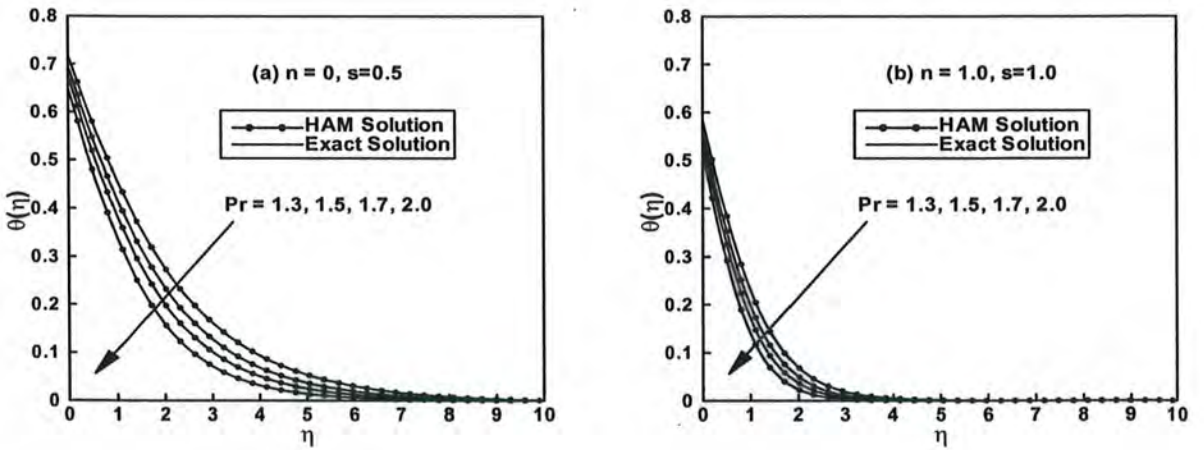


Figure 2.9: The comparison of the HAM solution with exact solution for the temperature profile $\theta(\eta)$.



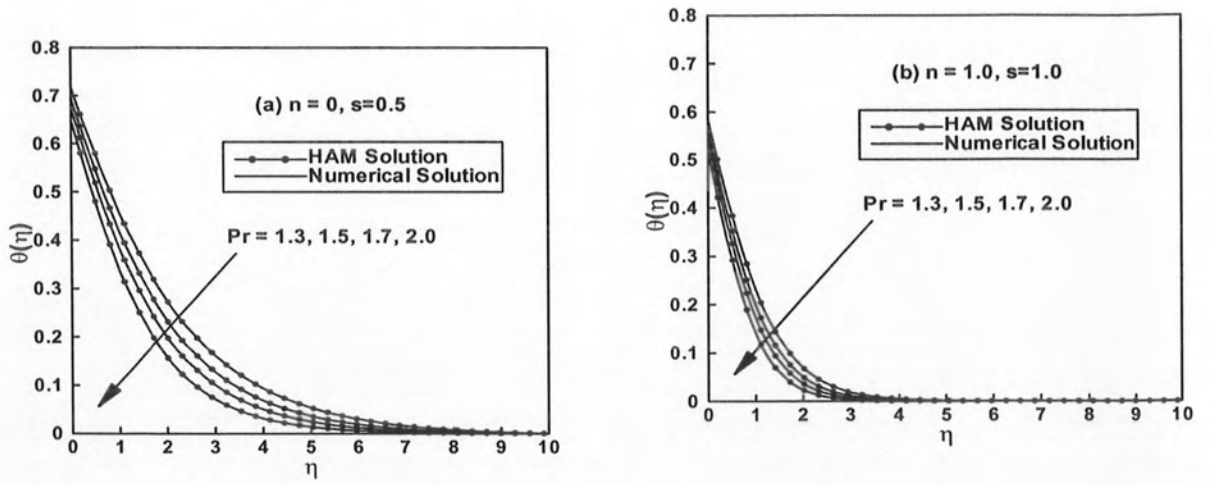


Figure 2.10: The comparison of the HAM solution with numerical solution for the temperature profile $\theta(\eta)$.

Table 2.2: Numerical values of the local skin friction coefficient $\frac{1}{2} \text{Re}_b^{\frac{1}{n+1}} C_{fx}$ for different values of physical parameters.

A	D	s	$-\frac{1}{2} \text{Re}_b^{\frac{1}{n+1}} C_{fx}$			
			n = 0	n = 1	n = 2	n = 3
0.0	1.0	0.5	1.000000	1.259683	1.168175	1.121380
1.0			2.224745	1.781461	1.631523	1.558845
2.0			2.732051	2.181835	2.024553	1.954535
3.0			3.121320	2.519366	2.366378	2.304718
1.0	0.0	0.5	1.707107	1.089465	0.962186	0.908237
		0.5	1.866025	1.296307	1.153318	1.090619
		1.0	2.224745	1.781461	1.631523	1.558845
		2.0	3.121320	3.028033	2.999168	2.981083
1.0	1.0	0.5	2.224745	1.781461	1.631523	1.558845
		1.0	2.290994	2.00000	1.914495	1.875081
		2.0	2.431934	2.376857	2.412204	2.446648
		3.0	2.573536	2.701216	2.851608	2.965925

Table 2.3: Numerical values of the local Nusselt number $\text{Re}_b^{-\frac{1}{n+1}} Nu_x$ for different values of physical parameters.

A	D	Pr	γ	s	$-\text{Re}_b^{-\frac{1}{n+1}} Nu_x$			
					$n = 0$	$n = 1$	$n = 2$	$n = 3$
1.0	1.0	1.0	1.0	0.5	0.240458	0.331260	0.340045	0.342428
					0.275129	0.346666	0.357093	0.360945
					0.291544	0.355742	0.367068	0.371748
1.0	0.0	1.0	1.0	0.5	0.291544	0.362207	0.367377	0.368707
	0.5				0.275129	0.353119	0.359256	0.360679
	1.0				0.240458	0.331260	0.340045	0.342428
0.5	1.0	0.7	1.0	0.5	0.191051	0.277793	0.284027	0.285370
		1.0			0.240458	0.353119	0.340045	0.342428
		2.0			0.349286	0.438483	0.450994	0.455287
1.0	1.0	1.0	0.1	0.5	0.075993	0.083203	0.083747	0.083891
			0.5		0.193846	0.248832	0.253757	0.255081
			1.0		0.240458	0.331260	0.340045	0.342428
1.0	1.0	1.0	1.0	0.5	0.240458	0.331260	0.340045	0.342428
				0.7	0.173867	0.347092	0.370199	0.378838
				1.0	0.024606	0.367879	0.406270	0.420928

Chapter 3

MHD Flow and Heat Transfer of Sisko Fluid over a Radially Stretching Sheet

The present chapter analyzes magnetohydrodynamics (MHD) axisymmetric flow of an electrically conducting incompressible Sisko fluid over a radially stretching surface. The analysis includes forced convective heat transfer by considering convective boundary conditions. The local-similar transformations are adopted to transform the nonlinear governing partial differential equations into ordinary differential equations. These equations are then solved analytically as well as numerically by utilizing the homotopy analysis method (HAM) and fourth order Runge-Kutta method with shooting technique, respectively, for both integer and non-integer values of the power-law index. As a result of the analysis, some exact solutions for the velocity and temperature distributions are obtained and a comparison of exact solutions and numerical solutions is made with the HAM solutions with an excellent agreement. To investigate the influence of various pertinent parameters, graphical results for the velocity and temperature fields are presented for different values of the governing parameters. It is found that inside the boundary layer the value of the power-law index affects significantly the velocity field but marginally the temperature field.

Further, our results show that the effects of the magnetic parameter on the velocity and temperature fields are quite opposite.

3.1 Formulation of the Problem

3.1.1 Geometry of the Problem

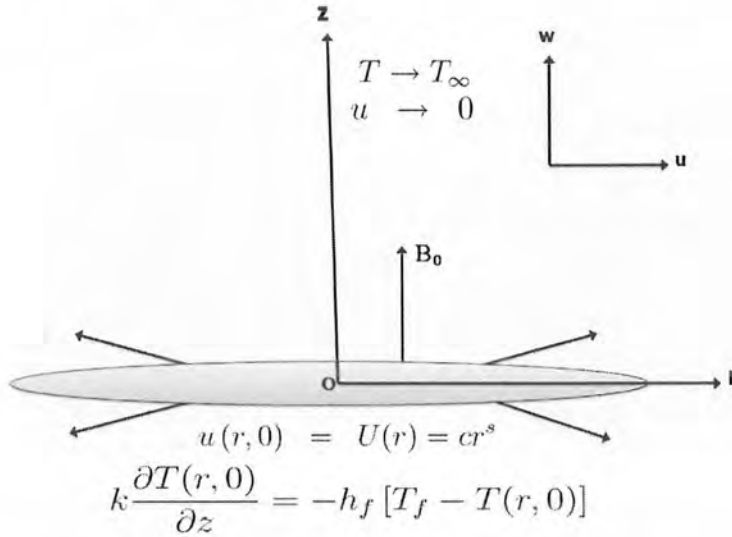


Figure 3.1: Physical model and coordinate system.

3.1.2 Flow and Heat Transfer Analysis

Consider the steady, two-dimensional convective boundary layer flow of an electrically conducting incompressible Sisko fluid over a nonlinear radially stretching sheet placed at $z = 0$. The flow is induced by stretching of the flat sheet with velocity $U = cr^s$, where c and s are non-negative real numbers. A uniform magnetic field $\mathbf{B} = [0, 0, B_0]$ perpendicular to the plane of sheet is applied under the assumption of very small magnetic Reynolds number. It is assumed that the bottom surface of the sheet is heated by convection from a hot fluid with temperature T_f which provides a

heat transfer coefficient h_f . Further, the uniform ambient fluid temperature is T_∞ . Here, for mathematical modelling we have considered cylindrical polar coordinates (r, θ, z) . For axisymmetric flow the corresponding velocity, temperature and extra stress tensor are defined as follows:

$$\mathbf{V}(r, z) = [u(r, z), 0, w(r, z)], \quad T = T(r, z), \quad \mathbf{S} = \mathbf{S}(r, z), \quad (3.1)$$

where u and w are the components of velocity in the radial and axial directions, respectively.

Under these considerations, the flow is governed by Eqs. (2.1) to (2.5). More exactly, in view of Eq. (3.1), the governing equations (2.1) to (2.3) for the problem under consideration reduce to

$$\frac{\partial u}{\partial r} + \frac{u}{r} + \frac{\partial w}{\partial z} = 0, \quad (3.2)$$

$$\rho \left(u \frac{\partial u}{\partial r} + w \frac{\partial u}{\partial z} \right) = -\frac{\partial p}{\partial r} + \frac{\partial S_{rr}}{\partial r} + \frac{\partial S_{rz}}{\partial z} + \frac{S_{rr} - S_{\theta\theta}}{r} - \frac{\sigma B_0^2}{\rho} u, \quad (3.3)$$

$$\rho \left(u \frac{\partial w}{\partial r} + w \frac{\partial w}{\partial z} \right) = -\frac{\partial p}{\partial z} + \frac{\partial S_{rz}}{\partial r} + \frac{\partial S_{zz}}{\partial z} + \frac{S_{rz}}{r}, \quad (3.4)$$

$$u \frac{\partial T}{\partial r} + w \frac{\partial T}{\partial z} = \alpha \left(\frac{\partial^2 T}{\partial r^2} + \frac{\partial^2 T}{\partial z^2} \right). \quad (3.5)$$

In view of Eq. (3.1), the momentum and thermal energy Eqs. (3.3) – (3.5) after application of the usual boundary layer approximations in the presence of a constant magnetic field take the form

$$u \frac{\partial u}{\partial r} + w \frac{\partial u}{\partial z} = \frac{a}{\rho} \frac{\partial^2 u}{\partial z^2} - \frac{b}{\rho} \frac{\partial}{\partial z} \left(-\frac{\partial u}{\partial z} \right)^n - \frac{\sigma B_0^2}{\rho} u, \quad (3.6)$$

$$u \frac{\partial T}{\partial r} + w \frac{\partial T}{\partial z} = \alpha \frac{\partial^2 T}{\partial z^2}. \quad (3.7)$$

The above equations are subjected to the following boundary conditions

$$u(r, z) = U = cr^s, \quad w(r, z) = 0, \quad k \frac{\partial T(r, z)}{\partial z} = -h_f [T_f - T(r, z)] \quad \text{at } z = 0, \quad (3.8)$$

$$u \rightarrow 0, \quad T \rightarrow T_\infty \quad \text{as } z \rightarrow \infty. \quad (3.9)$$

The governing equations (3.6) and (3.7) subject to the boundary conditions (3.8) and (3.9) can be expressed in simpler form by introducing the following local similarity transformations

$$\eta = \frac{z}{r} \text{Re}_b^{\frac{1}{n+1}}, \quad \psi = -Ur^2 \text{Re}_b^{-\frac{1}{n+1}} f(\eta), \quad (3.10)$$

where η is the independent variable and ψ the Stokes stream function such that $u = -\frac{1}{r} \frac{\partial \psi}{\partial z}$ and $v = \frac{1}{r} \frac{\partial \psi}{\partial r}$.

By employing the transformations (3.10), the above governing problem reduces to

$$Af''' + n(-f'')^{n-1} f''' + \left(\frac{s(2n-1) + n + 2}{n+1} \right) f f'' - s(f')^2 - D^2 f' = 0, \quad (3.11)$$

$$\theta'' + \left(\frac{s(2n-1) + n + 2}{n+1} \right) \text{Pr} f \theta' = 0, \quad (3.12)$$

$$f(0) = 0, \quad f'(0) = 1, \quad \theta'(0) = -\gamma [1 - \theta(0)], \quad (3.13)$$

$$f'(\eta) \rightarrow 0, \quad \theta(\eta) \rightarrow 0 \quad \text{as } \eta \rightarrow \infty. \quad (3.14)$$

In the above equations, primes denote differentiation with respect to the independent variable η . Further, A is the material parameter of the Sisko fluid, D the magnetic parameter, Re_a and Re_b the local Reynolds numbers, Pr the generalized Prandtl number and γ the generalized Biot number, which are defined as

$$D^2 = \frac{\sigma B_0^2}{\rho U} r, \quad \text{Re}_a = \frac{\rho r U}{a}, \quad \text{Re}_b = \frac{\rho r^n U^{2-n}}{b}, \quad A = \frac{\text{Re}_b^{\frac{2}{n+1}}}{\text{Re}_a}, \quad \gamma = \frac{h_f r}{k} \text{Re}_b^{-\frac{1}{n+1}}, \quad \text{Pr} = \frac{r U}{\alpha} \text{Re}_b^{-\frac{2}{n+1}}. \quad (3.15)$$

The physical quantities of pivotal interest are the local skin-friction coefficient C_{fr} and the local Nusselt number Nu_r , which are defined in dimensionless form by

$$\frac{1}{2} \text{Re}_b^{\frac{1}{n+1}} C_{fr} = A f''(0) - [-f''(0)]^n, \quad (3.16)$$

$$\text{Re}_b^{-\frac{1}{n+1}} Nu_r = -\theta'(0). \quad (3.17)$$

3.2 Solution Methodologies

3.2.1 The HAM Solution

The analytic series solutions for the velocity and temperature fields are obtained for the nonlinear equations (3.11) and (3.12) together with the boundary conditions (3.13) and (3.14) by utilizing the homotopy analysis method. The initial guesses and linear operators corresponding to the flow and heat transfer analysis are chosen as follows:

$$f_0(\eta) = 1 - e^{-\eta}, \quad \theta_0(\eta) = \frac{\gamma e^{-\eta}}{1 + \gamma}, \quad (3.18)$$

$$\mathcal{L}_f = \frac{d^3}{d\eta^3} - \frac{d}{d\eta}, \quad \mathcal{L}_\theta = \frac{d^2}{d\eta^2} - 1. \quad (3.19)$$

The convergence of these series solutions is highly dependent upon the selection of the auxiliary parameters \hbar_f and \hbar_θ and these are calculated by using the squared residual error defined through Eq. (2.39).

Table 3.1 depicts the convergence of the series solution for a specific case. Considering the most suitable value of \hbar_f and \hbar_θ the convergence is achieved at 13th and 16th order of approximations for flow and heat transfer analysis, respectively.

Table 3.1: The convergence of the series solution when $s = D = A = \gamma = \text{Pr} = 1$, $\hbar_f = -0.474652$, $\hbar_\theta = -0.685443$ and $n = 2$ are fixed.

Order of approximation	$-f''(0)$	$-\theta'(0)$
1	1.026370	0.480960
5	1.038526	0.489321
11	1.038566	0.489558
13	1.038567	0.489572
16	1.038567	0.489573
18	1.038567	0.489573
20	1.038567	0.489573
25	1.038567	0.489573

3.2.2 The Numerical Solution

The nonlinear equations (3.11) and (3.12) governing the problem along with the boundary conditions (3.13) and (3.14) form a set of boundary value problems (BVPs). These BVPs are first converted into a set of initial value problems (IVPs) and then solved numerically by utilizing the shooting method. We have converted Eqs. (3.11)

and (3.12) into system of first order equations as follows:

$$y_1' = y_2, y_2' = y_3, y_3' = -\frac{1}{A + n(-y_3)^{n-1}} \left[\left(\frac{s(2n-1) + n + 2}{n+1} \right) y_1 y_3 - s(y_2)^2 - D^2 y_2 \right], \quad (3.20)$$

$$y_4' = y_5, y_5' = -\left(\frac{s(2n-1) + n + 2}{n+1} \right) \text{Pr } y_1 y_5, \quad (3.21)$$

with boundary conditions

$$y_1(0) = 0, y_2(0) = 1, y_5(0) = -\gamma[1 - y_4(0)]. \quad (3.22)$$

To solve Eqs. (3.20) and (3.21) as initial value problems we need values for $f''(0)$ and $\theta'(0)$ which are not defined. Thus we choose values for $f''(0)$ and $\theta'(0)$ and obtain the solution by using fourth-order Runge-Kutta method. The obtained values of $f'(\eta)$ and $\theta(\eta)$ as $\eta \rightarrow \infty$, say η_∞ , are compared with the given boundary conditions $f'(\eta_\infty) = 0$ and $\theta(\eta_\infty) = 0$. Then to get better approximation for our solution $f''(0)$ and $\theta'(0)$ are adjusted using the Newton method. Here we have considered step size $h = 0.01$. Until we approach the desired accuracy of our results the process is repeated.

3.2.3 The Exact Solution

The set of Eqs. (3.11) and (3.12) subject to the boundary conditions (3.13) and (3.14) is highly nonlinear. In addition, the power-law index n is a non-negative real number and hence finding the exact solution of the system in general is a far from any routine exercise. However, exact solutions of the system are calculated for some

special cases given below.

Case (i): For $n = 0$ and $s = 1$, Eqs. (3.11) and (3.12) reduce to

$$A f''' + f f'' - (f')^2 - D^2 f' = 0, \quad (3.23)$$

$$\theta'' + \text{Pr} f \theta' = 0. \quad (3.24)$$

The exact solutions of Eqs. (3.23) and (3.24) satisfying the boundary conditions (3.13) and (3.14) are

$$f(\eta) = \frac{1}{\beta} (1 - e^{-\beta\eta}), \quad (3.25)$$

$$\theta(\eta) = \frac{e^{\frac{\text{Pr}}{\beta^2}\eta} \gamma \left[\Gamma\left(\frac{\text{Pr}}{\beta^2}, 0\right) - \Gamma\left(\frac{\text{Pr}}{\beta^2}, \frac{\text{Pr}}{\beta^2} e^{-\beta\eta}\right) \right]}{\beta \left(\frac{\text{Pr}}{\beta^2}\right)^{\frac{\text{Pr}}{\beta^2}} + e^{\frac{\text{Pr}}{\beta^2}\eta} \gamma \left[\Gamma\left(\frac{\text{Pr}}{\beta^2}, 0\right) - \Gamma\left(\frac{\text{Pr}}{\beta^2}, \frac{\text{Pr}}{\beta^2}\right) \right]}, \quad (3.26)$$

where $\beta = \sqrt{\frac{1+D^2}{A}}$ and $\Gamma(\cdot)$ is the incomplete Gamma function.

Case (ii): Next for $n = 1$ and $s = 3$, Eqs. (3.11) and (3.12) take the form

$$(1 + A) f''' + 3 f f'' - 3 (f')^2 - D^2 f' = 0, \quad (3.27)$$

$$\theta'' + 3 \text{Pr} f \theta' = 0. \quad (3.28)$$

The exact analytical solutions to Eqs. (3.27) and (3.28) together with the boundary conditions (3.13) and (3.14) are in the form

$$f(\eta) = \frac{1}{\beta} (1 - e^{-\beta\eta}), \quad (3.29)$$

$$\theta(\eta) = \frac{e^{\frac{3Pr}{\beta^2}} \gamma \left[\Gamma\left(\frac{3Pr}{\beta^2}, 0\right) - \Gamma\left(\frac{3Pr}{\beta^2}, \frac{3Pr}{\beta^2} e^{-\beta\eta}\right) \right]}{\beta \left(\frac{3Pr}{\beta^2}\right)^{\frac{3Pr}{\beta^2}} + e^{\frac{3Pr}{\beta^2}} \gamma \left[\Gamma\left(\frac{3Pr}{\beta^2}, 0\right) - \Gamma\left(\frac{3Pr}{\beta^2}, \frac{3Pr}{\beta^2}\right) \right]}, \quad (3.30)$$

with $\beta = \sqrt{\frac{3+D^2}{1+A}}$.

3.3 Results and Discussion

The non-dimensional equations of convective MHD boundary layer flow corresponding to the Sisko fluid over a radially stretching sheet are studied. The system of coupled ordinary differential equations (3.11) and (3.12) subject to the boundary conditions (3.13) and (3.14) is solved analytically using the HAM and numerically using the shooting technique with forth-order Runge-Kutta method. In addition, exact solutions for particular cases, where possible, are constructed. Further, the numerical values of the local skin-friction coefficient and local Nusselt number with varying physical parameters are recorded through tables. It is worth pointing out that the parameter which controls the power-law behavior of the fluid, called the power-law index n , appears in the equations and is a non-negative real number. The HAM results are only for integer values of the power-law index n whereas the results for non-integer values of the power-law index n are obtained numerically. In this chapter, for the entire graphical analysis the non-dimensional parameters appearing in the problem are given fixed values i.e., $D = Pr = A = \gamma = 1$ and $s = 0.5$ except when a variation for a parameter is given or specified otherwise.

Figures 3.2 and 3.3 show the influence of the power-law index n on the velocity and temperature profiles, respectively. It can be seen in these figures that inside the

boundary layer the value of n effects significantly the velocity field but marginally the temperature field. It is observed from velocity profiles presented that for $n < 1$ (pseudoplastic or shear thinning fluids), as n increases the velocity profile increases near the surface but it decreases far away from the surface. For $n > 1$ (dilatant or shear thickening fluids) as n increases the velocity profile decreases throughout the domain. This results in a decrease in the boundary layer thickness for both shear-thinning and shear-thickening fluids. However, the apparent viscosity increases for $n < 1$ and decreases for $n > 1$ and as a consequence the viscous effects are transmitted up to a greater distance from the sheet and the boundary layer thickness is thicker for $n < 1$ as compared to $n > 1$. From the temperature profile presented, it is noticed that for both $n < 1$ and $n > 1$, the temperature as well as the corresponding thermal boundary layer thickness reduce with an increase in n . In addition, a more noteworthy influence might be seen for $n < 1$ when compared with $n > 1$.

In order to visualize the development of the momentum and thermal boundary layers for Sisko fluid, the velocity and temperature profiles for different values of the magnetic parameter D are plotted in figures 3.4 and 3.5, respectively. Figure 3.4 tracks the evolution of the velocity profile for varying values of the power-law index n . It can be observed from this figure that an increment in value of the magnetic parameter D resulted in reduction of the velocity as well as the boundary layer thickness. This is because of the resistance of the drag force produced by the magnetic field. Besides, these figures reveal a correlation that the magnitude of the velocity is larger for hydrodynamic case ($D = 0$) when contrasted with hydromagnetic case ($D \neq 0$). Figure 3.5 tracks the evolution of the temperature profile for different values of the magnetic parameter D . It is quite clear from these figures that the

effects of the magnetic parameter D on the temperature field and thermal boundary layer are quite opposite to those for velocity. These figures, apart from demonstrating the effects of the magnetic parameter, also show that the influence of the magnetic parameter D gets less overwhelming as we go on increasing value of the power-law index n .

The effects of the generalized Prandtl number Pr on the temperature profile are shown in figure 3.6. It can be seen that as the generalized Prandtl number increases the temperature profile decreases. This is because of the fact that the fluids with higher Prandtl number possess low thermal conductivity which reduces the conduction and hence the thermal boundary layer thickness.

Figure 3.7 shows the influence of the generalized Biot number γ on the temperature profile. For $\gamma = 0$, the bottom side of the sheet with the hot fluid is totally insulated and as a result no convective heat transfer to the cold fluid above the sheet takes place. It is observed from the profiles presented in these figures that as the generalized Biot number γ increases, the temperature profile increases significantly. This further results in an increase in the thermal boundary layer thickness. This is because of the fact that the increase in the Biot number resulting in an increase in convection which reduces the sheet thermal resistance.

The effect of the material parameter A on the temperature field is shown in figure 3.8. These figures also provide a comparison of the temperature profiles of the Sisko fluid ($A \neq 0$) with those of the power-law fluid ($A = 0, n \neq 1$) and the Newtonian fluid ($A = 0, n = 1$). It is seen that as A increases, the temperature profile and corresponding thermal boundary layer thickness decrease for $n = 0, 1, 2$ and 3 . Hence, we conclude from these figures that the temperature of Newtonian fluid is

higher than that of the Sisko fluid. Further, the temperature for the power-law fluid is also higher than that of the Sisko fluid.

Figures 3.9 and 3.10 as well as tables 3.2 and 3.3 show the comparison of temperature field, the local skin-friction coefficient $\frac{1}{2} \text{Re}_b^{\frac{1}{n+1}} C_{fr}$ and the local Nusselt number $\text{Re}_b^{-\frac{1}{n+1}} Nu_r$ amongst the exact, HAM and numerical results. Here, it is seen that the comparison is in very good agreement and thus gives us confidence to the accuracy of the HAM results. Further, the variation of the local skin-friction coefficient and the local Nusselt number is shown in tables 3.4 and 3.5, respectively. These tables show that the magnitude of the local skin-friction coefficient and local Nusselt number is larger for Sisko fluid when compared to the power-law fluid as well as Newtonian fluid. Additionally, by comparing the hydrodynamic case with hydromagnetic case, we can see that the magnitude of the local skin-friction coefficient is larger in the later case whereas for the local Nusselt number results are opposite qualitatively. Also, it is seen that the local skin-friction coefficient is an increasing function of A , D and s while it decreases with the increasing values of the power-law index n . Additionally, the local Nusselt number shows an increasing behavior for A , Pr , γ and s and decreasing behavior for D .

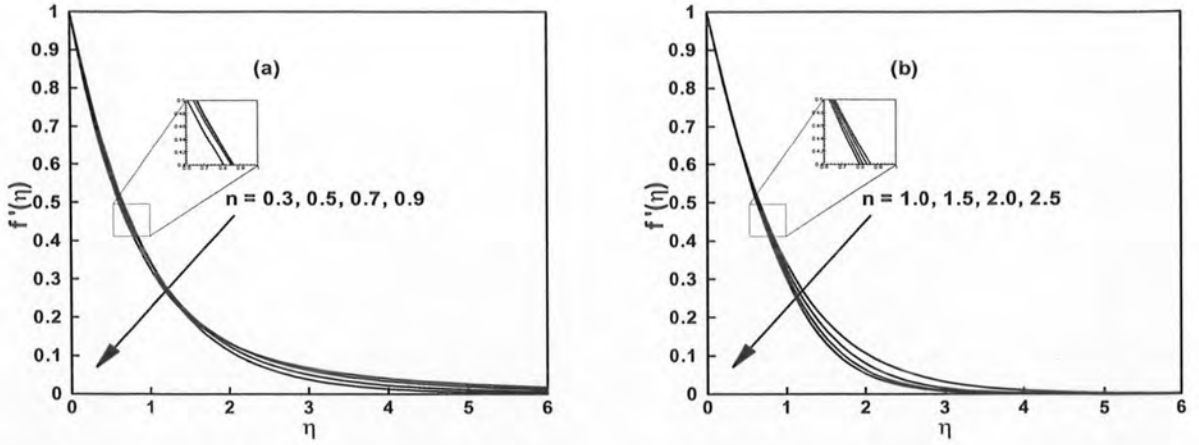


Figure 3.2: The velocity profiles $f'(\eta)$ for different values of the power-law index n .

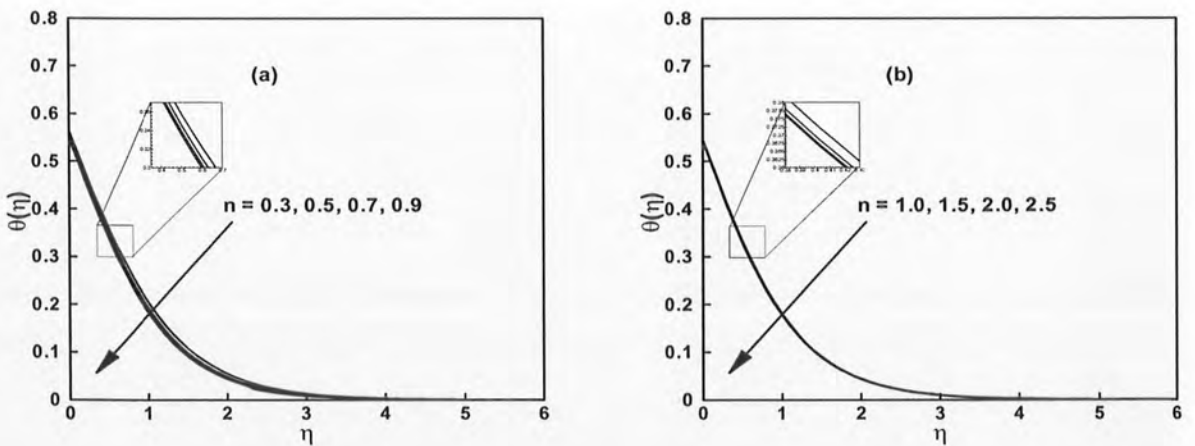


Figure 3.3: The temperature profiles $\theta(\eta)$ for different values of the power-law index n .

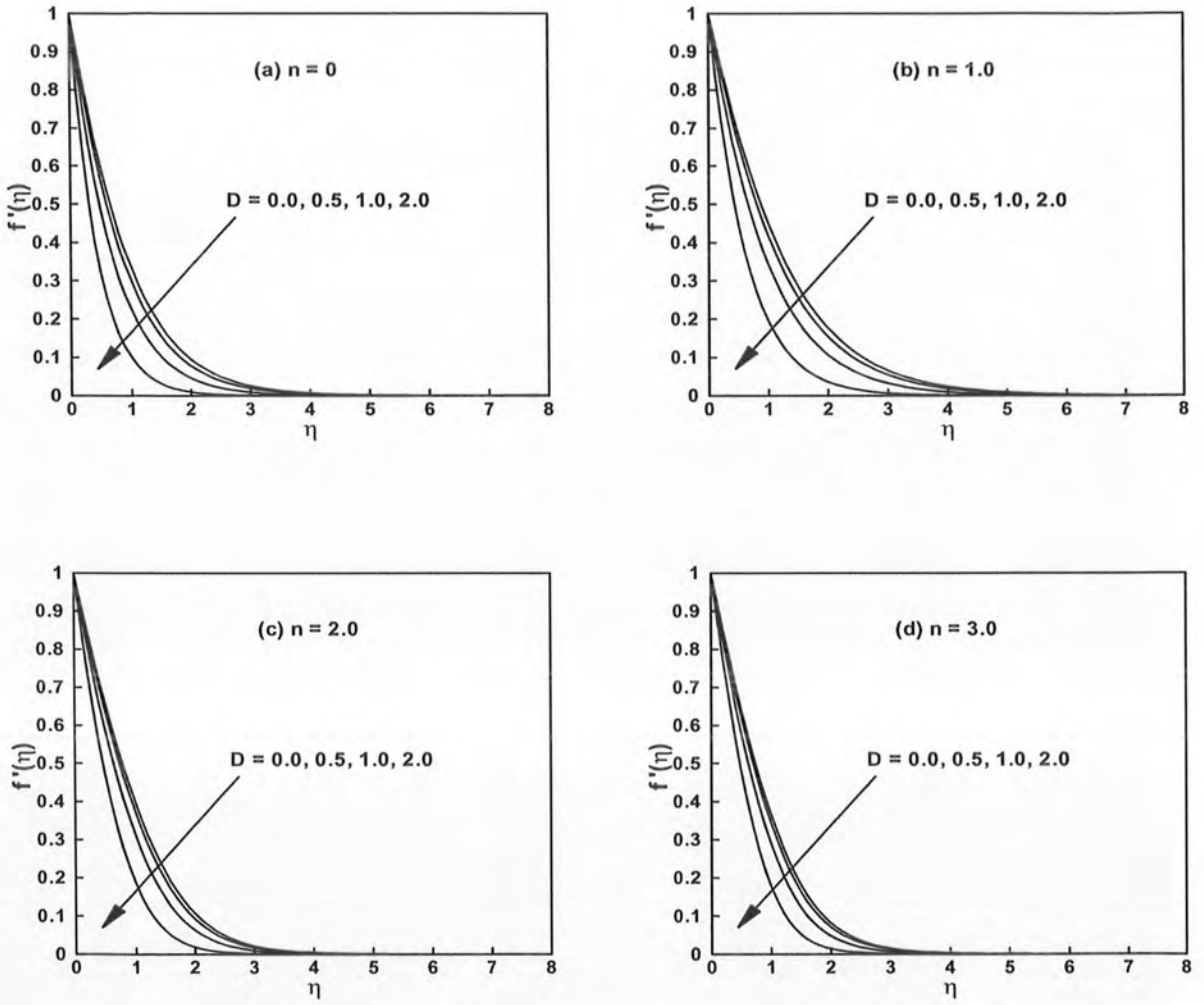


Figure 3.4: The velocity profiles $f'(\eta)$ for different values of the magnetic parameter

D .

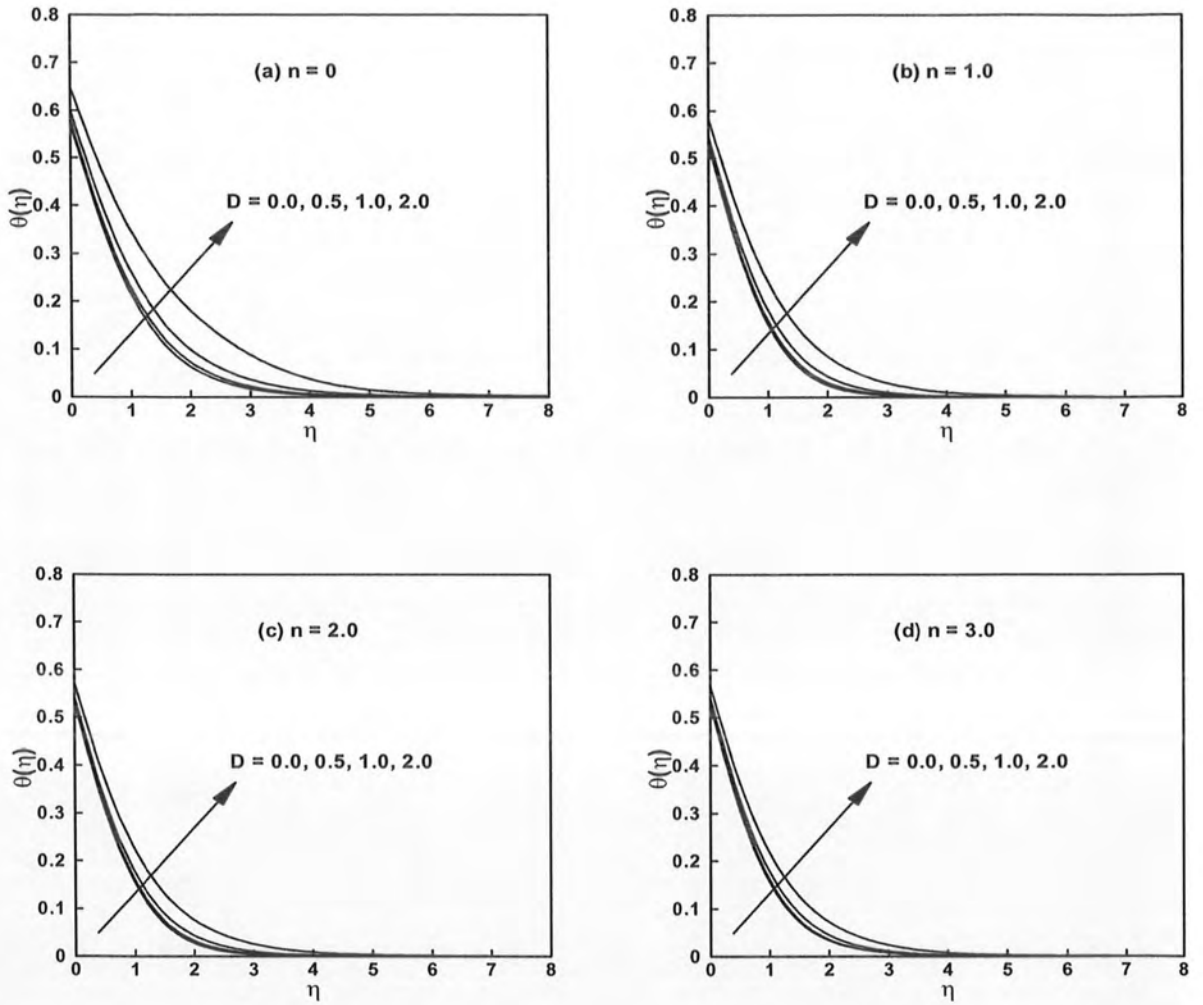


Figure 3.5: The temperature profiles $\theta(\eta)$ for different values of the magnetic parameter D .

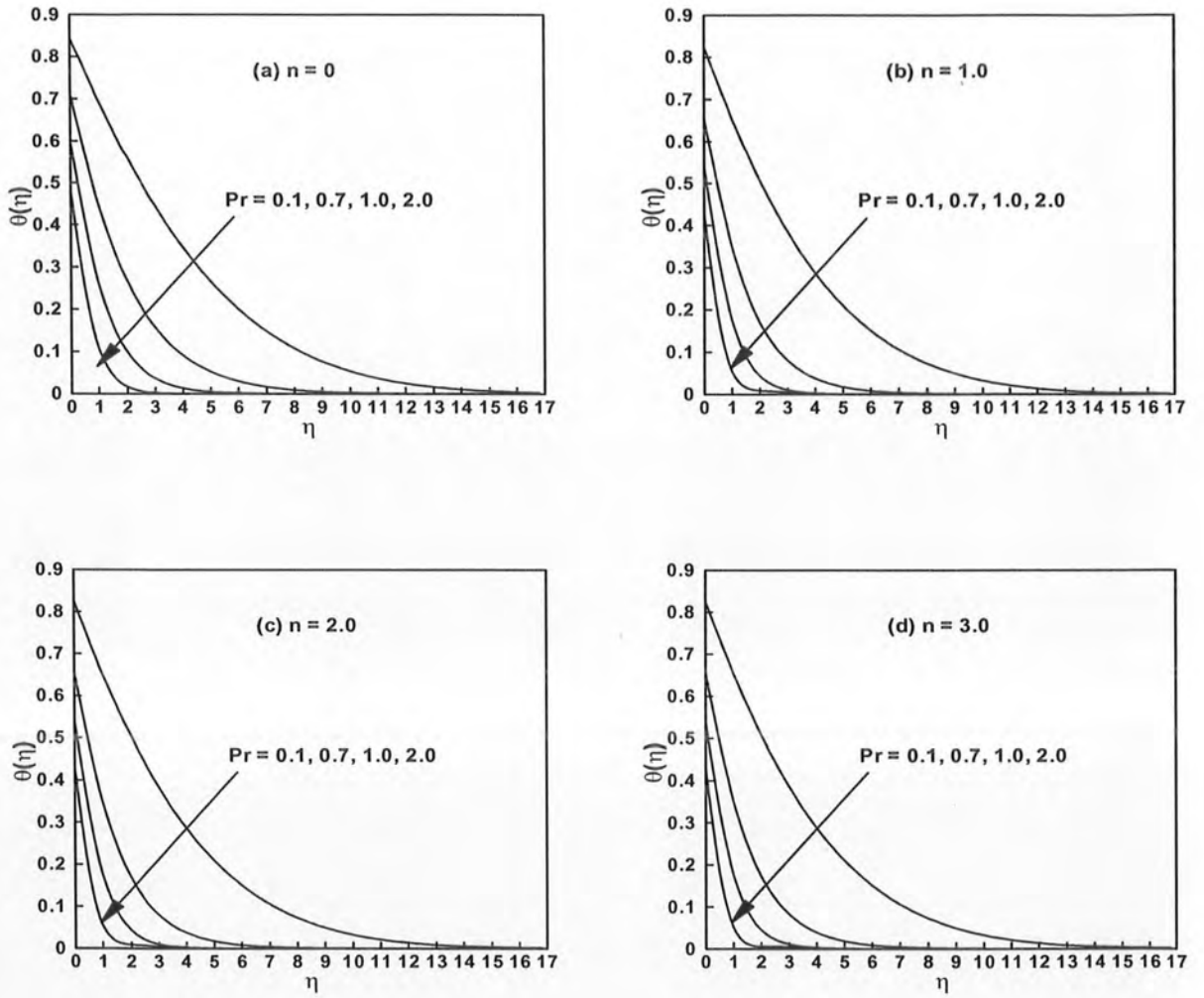


Figure 3.6: The temperature profiles $\theta(\eta)$ for different values of the generalized Prandtl number Pr .

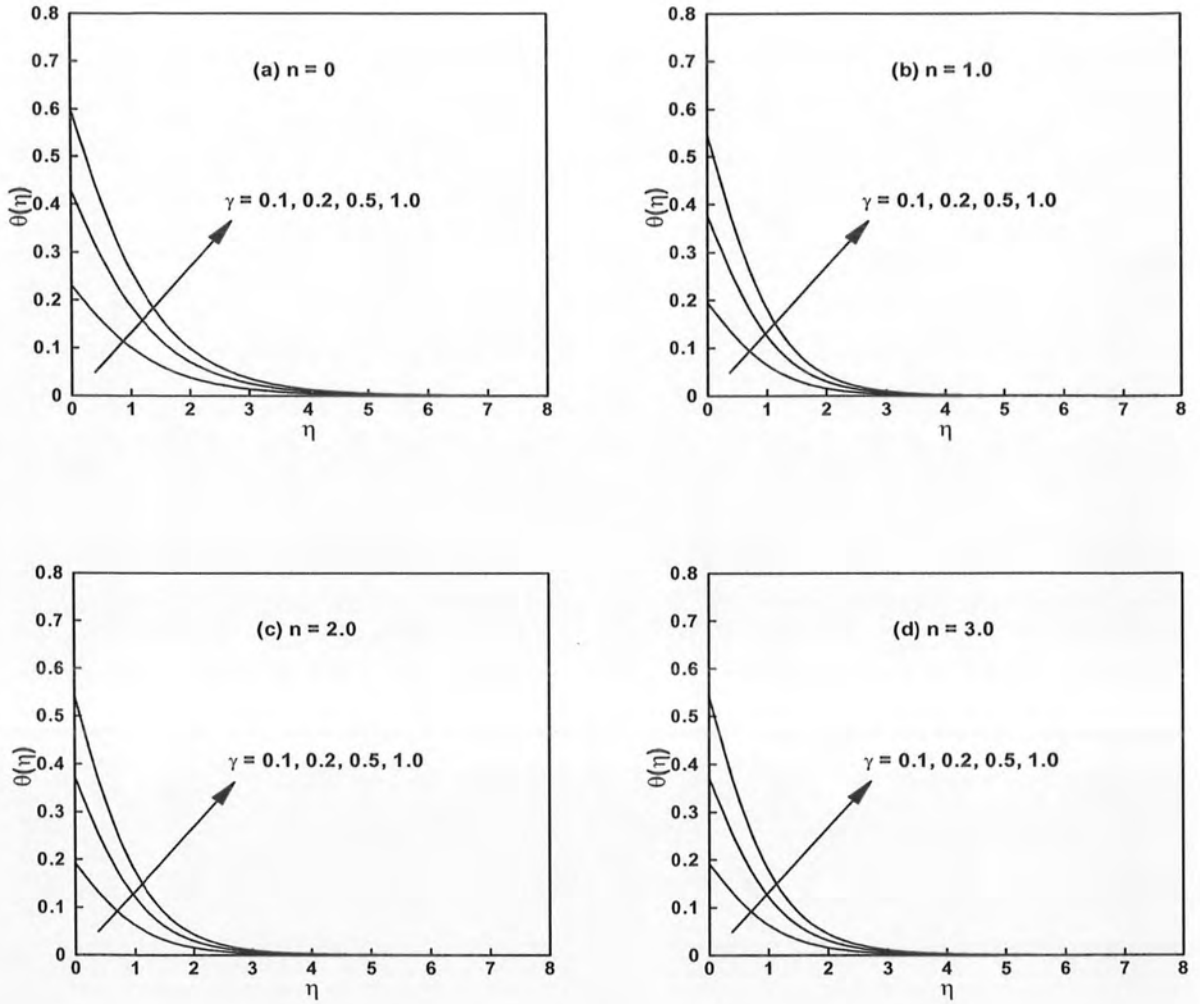


Figure 3.7: The temperature profiles $\theta(\eta)$ for different values of the generalized Biot number γ .

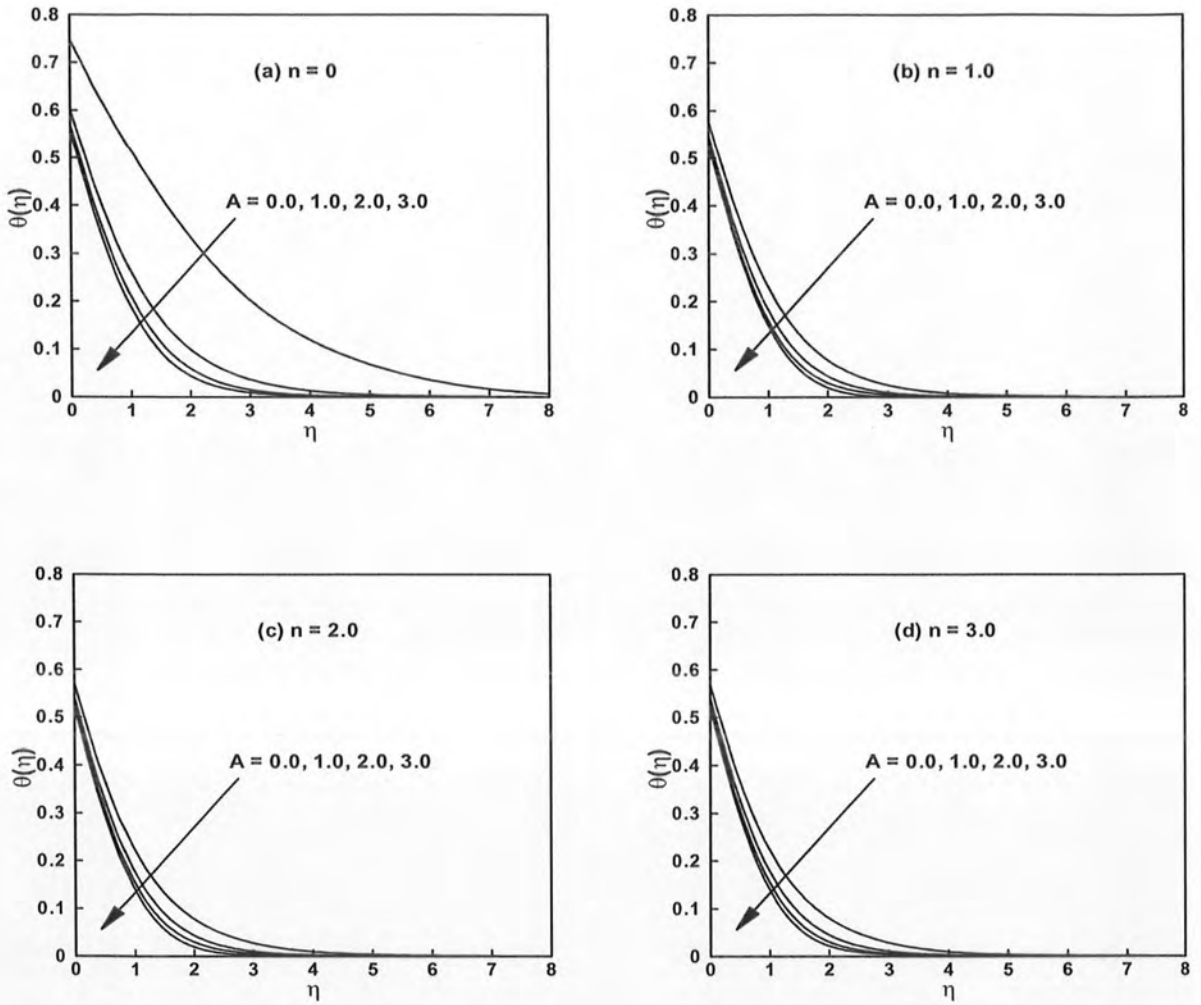


Figure 3.8: The temperature profiles $\theta(\eta)$ for different values of the material parameter A .

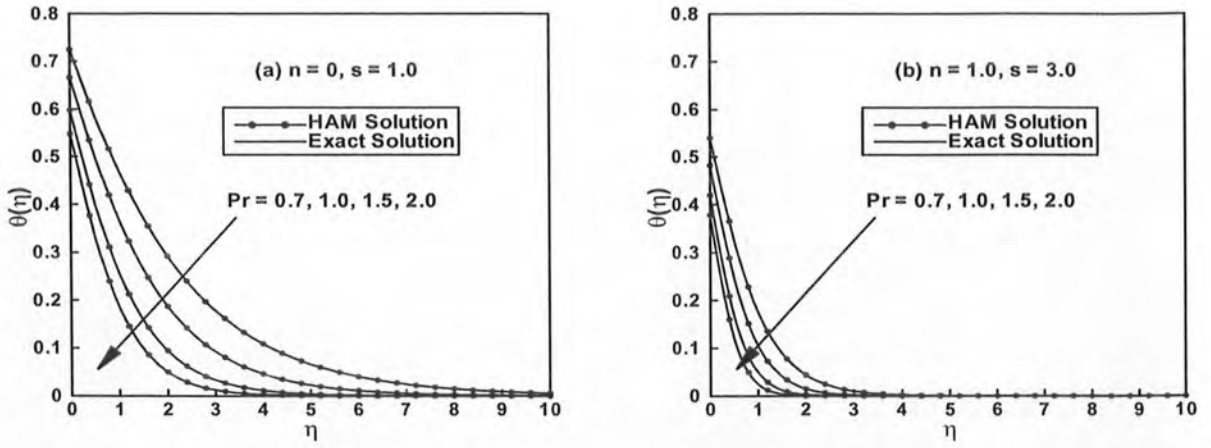


Figure 3.9: A comparison of the HAM and exact solutions for the $\theta(\eta)$.

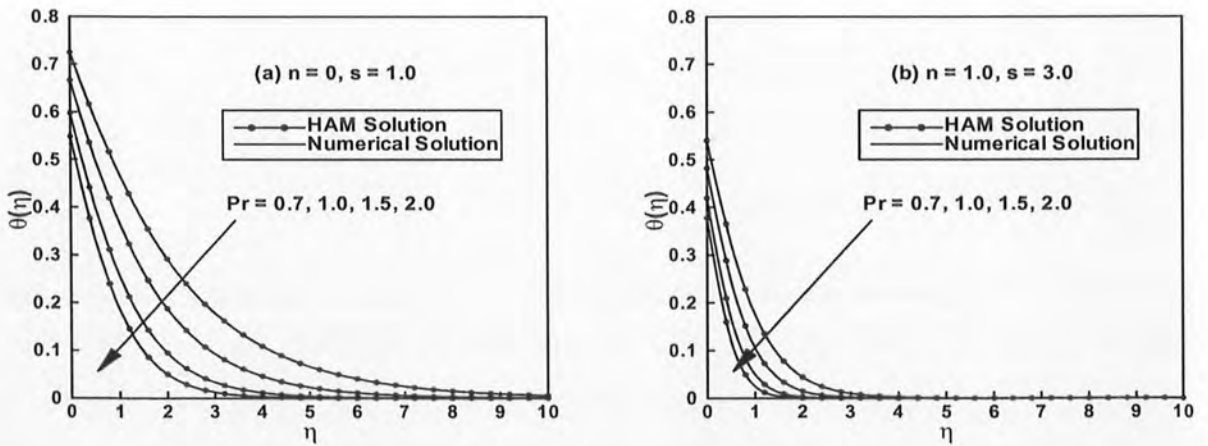


Figure 3.10: A comparison of the HAM and numerical solutions for the $\theta(\eta)$.

Table 3.2: A comparison between the HAM and exact solutions for the skin friction coefficient.

D	A	$-\frac{1}{2} \text{Re}_b^{\frac{1}{n+1}} C_{fr}$			
		$n = 0, s = 1.0$		$n = 1, s = 3.0$	
		Exact solution	HAM solution	Exact solution	HAM solution
1.0	0.0	1.000000	1.000000	2.000000	2.000000
1.0	0.5	2.000000	2.000000	2.449489	2.449489
1.0	1.0	2.414213	2.414213	2.828427	2.828427
1.0	1.5	2.732050	2.732050	3.162277	3.162277
1.0	2.0	3.000000	3.000000	3.464101	3.464101
2.0	0.0	1.000000	1.000000	2.645751	2.645751
2.0	0.5	2.581138	2.581138	3.240370	3.240370
2.0	1.0	3.236067	3.236067	3.741657	3.741657
2.0	1.5	3.738612	3.738612	4.183300	4.183300
2.0	2.0	4.162277	4.162277	4.582575	4.582575

Table 3.3: A comparison between the HAM and exact solutions for the local

Nusselt number.

A	D	Pr	γ	$-\text{Re}_b^{-\frac{1}{n+1}} Nu_r$			
				$n = 0, s = 1.0$		$n = 1.0, s = 3.0$	
				Exact solution	HAM solution	Exact solution	HAM solution
1.0	1.0	1.0	0.1	0.083367	0.083367	0.091490	0.091490
1.0	1.0	1.0	0.2	0.142959	0.142959	0.168632	0.168632
1.0	1.0	1.0	0.5	0.250312	0.250312	0.341291	0.341291
1.0	1.0	1.0	1.0	0.333888	0.333888	0.518121	0.518121
1.0	1.0	2.0	0.1	0.089166	0.089166	0.094278	0.094278
1.0	1.0	2.0	0.2	0.160900	0.160900	0.178353	0.178353
1.0	1.0	2.0	0.5	0.311041	0.311041	0.383607	0.383607
1.0	1.0	2.0	1.0	0.451465	0.451465	0.622343	0.622343

Table 3.4: Numerical values of the skin friction coefficient $\frac{1}{2} \text{Re}_b^{\frac{1}{n+1}} C_{fr}$ for different values of physical parameters.

A	D	s	$-\frac{1}{2} \text{Re}_b^{\frac{1}{n+1}} C_{fr}$			
			$n = 0$	$n = 1.0$	$n = 2.0$	$n = 3.0$
0.0	1.0	0.5	1.000000	1.395883	1.369854	1.357321
1.0			2.362506	1.974077	1.852944	1.790524
2.0			2.926875	2.417741	2.273963	2.203414
1.0	0.0	0.5	1.939180	1.399534	1.280257	1.220124
	1.0		2.362506	1.974077	1.852944	1.790524
	2.0		3.200468	3.139790	3.145211	3.149431
1.0	1.0	0.5	2.362506	1.974077	1.852944	1.790524
		1.0	2.414214	2.171823	2.117189	2.092716
		2.0	2.527525	2.521496	2.590447	2.645556

Table 3.5: Numerical values of the local Nusselt number $\text{Re}_b^{-\frac{1}{n+1}} Nu_r$ for different values of physical parameters.

A	D	Pr	γ	s	$-\text{Re}_b^{-\frac{1}{n+1}} Nu_r$				
					$n = 0$	$n = 1.0$	$n = 2.0$	$n = 3.0$	
0.0	1.0	1.0	1.0	0.5	0.252262	0.422551	0.428277	0.429523	
					1.0	0.399606	0.452675	0.456642	0.457250
					2.0	0.430592	0.465420	0.469661	0.470823
1.0	0.0	1.0	1.0	0.5	0.427702	0.470063	0.471092	0.470521	
					0.5	0.419895	0.465321	0.467117	0.466791
					1.0	0.399606	0.452675	0.456642	0.457250
1.0	1.0	0.7	1.0	0.5	0.338044	0.395301	0.397475	0.397133	
					1.0	0.399606	0.452675	0.456642	0.457250
					2.0	0.516778	0.559069	0.564852	0.566769
1.0	1.0	1.0	0.1	0.5	0.086938	0.089213	0.089366	0.089390	
					0.5	0.285513	0.311615	0.313489	0.313776
					1.0	0.399606	0.452675	0.456642	0.457250
1.0	1.0	1.0	1.0	0.5	0.399606	0.452675	0.456642	0.457250	
					1.0	0.333889	0.468686	0.489573	0.498138
					2.0	0.028896	0.495793	0.537845	0.554844

Chapter 4

Mixed Convective Heat Transfer to Sisko Fluid over a Radially Stretching Sheet

In this chapter, the mixed convective heat transfer to Sisko fluid over a radially stretching surface in the presence of convective boundary conditions is investigated. The viscous dissipation and thermal radiation effects are also taken into account. The suitable local-similarity transformations are applied to convert the governing partial differential equations into a set of coupled nonlinear ordinary differential equations. The analytical solution of the governing problem is obtained by using the homotopy analysis method (HAM). Additionally, these analytical results are compared with the numerical results obtained by the shooting technique. The obtained results for the velocity and temperature are analyzed graphically for several physical parameters for the assisting and opposing flows. It is found that the effect of the buoyancy parameter is more prominent in case of the assisting flow as compared to the opposing flow. Additionally, a careful observation reveals that the temperature profile is larger in case of opposing flow as compared to assisting flow. Consequently, the thermal boundary layer thickness is larger in case of assisting flow when comparing with the opposing flow. Further, in tabular form the numerical values are given for the

local skin friction coefficient and local Nusselt number. A remarkable agreement is noticed by comparing the present results with the results reported in the literature as a special case.

4.1 Problem Formulation

4.1.1 Geometry of the Problem

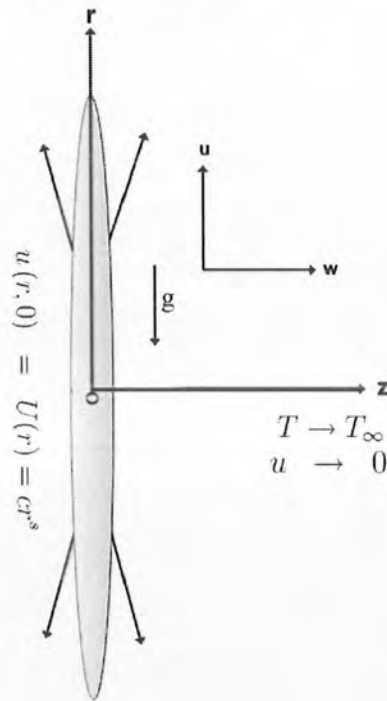


Figure 4.1: Physical model and coordinate system.

Consider the steady, two-dimensional mixed convective flow of Sisko fluid induced by a radially stretching sheet situated at plane $z = 0$ with power-law velocity. The viscous dissipation and thermal radiation effects are also considered. The choice of coordinate system is made such that r measures the distance along the sheet and the distance perpendicular to the sheet is measured by z . A heated fluid under the sheet with temperature T_f is used to change the temperature of the sheet by convective

heat transfer mode, which provides us the heat transfer coefficient h_f . Under these assumptions along with the Boussinesq and boundary layer approximations the system of equations which governs the mixed convection boundary layer flow, given by Eqs. (2.1) – (2.3), takes form

$$\frac{\partial u}{\partial r} + \frac{u}{r} + \frac{\partial w}{\partial z} = 0, \quad (4.1)$$

$$u \frac{\partial u}{\partial r} + w \frac{\partial u}{\partial z} = \frac{a}{\rho} \frac{\partial^2 u}{\partial z^2} - \frac{b}{\rho} \frac{\partial}{\partial z} \left(-\frac{\partial u}{\partial z} \right)^n \pm g\beta(T - T_\infty), \quad (4.2)$$

$$u \frac{\partial T}{\partial r} + w \frac{\partial T}{\partial z} = \alpha \frac{\partial^2 T}{\partial z^2} + \frac{1}{\rho c_p} \left[a \left(\frac{\partial u}{\partial z} \right)^2 + b \left(-\frac{\partial u}{\partial z} \right)^{n+1} \right] - \frac{1}{\rho c_p} \frac{\partial q_r}{\partial z}. \quad (4.3)$$

The appropriate boundary conditions for the velocity and temperature fields in the present problem are as follows:

$$u(r, z) = U = cr^s, \quad w(r, z) = 0, \quad k \frac{\partial T(r, z)}{\partial z} = -h_f [T_f - T(r, z)] \quad \text{at } z = 0, \quad (4.4)$$

$$u \rightarrow 0, \quad T \rightarrow T_\infty \quad \text{as } z \rightarrow \infty. \quad (4.5)$$

Here u and w denote the components of velocity parallel and perpendicular to the sheet, respectively, β and g represent the volumetric thermal expansion coefficient and gravitational acceleration, respectively. The sign \pm of the buoyancy term represents the upward and downward flow of free stream, respectively.

By using the Rosseland approximation for radiation [54], the radiative heat flux q_r is simplified as

$$q_r = -\frac{4\sigma^*}{3k^*} \frac{\partial T^4}{\partial z}, \quad (4.6)$$

where σ^* and k^* are the Stefan–Boltzmann constant and mean absorption coefficient,

respectively. By expressing the term T^4 as a linear function of the temperature using the Taylor's series expansion about T_∞ and neglecting higher-order terms, one has

$$q_r = -\frac{16\sigma^*T_\infty^3}{3k^*} \frac{\partial T}{\partial z}. \quad (4.7)$$

In view of Eqs. (4.6) and (4.7), the energy equation (4.3) becomes

$$u \frac{\partial T}{\partial r} + v \frac{\partial T}{\partial z} = \left(\alpha + \frac{16\sigma^*T_\infty^3}{3\rho c_p k^*} \right) \frac{\partial^2 T}{\partial z^2} + \frac{a}{\rho c_p} \left(\frac{\partial u}{\partial z} \right)^2 + \frac{b}{\rho c_p} \left(-\frac{\partial u}{\partial z} \right)^{n+1}. \quad (4.8)$$

Introducing stream function ψ , variable η and dimensionless temperature θ as

$$\psi = -r^2 U \text{Re}_b^{-\frac{1}{n+1}} f(\eta), \quad \eta = \frac{z}{r} \text{Re}_b^{\frac{1}{n+1}}, \quad \theta = \frac{T - T_\infty}{T_f - T_\infty}. \quad (4.9)$$

In perspective of Eq. (4.9), Eqs. (4.2), (4.4), (4.5) and (4.8) are reduced to the following two-point boundary value problem:

$$A f''' + n (-f'')^{n-1} f''' + \left(\frac{s(2n-1) + n + 2}{n+1} \right) f f'' - s (f')^2 + \lambda \theta = 0, \quad (4.10)$$

$$(1 + R_d) \theta'' + \text{Pr} \left(\frac{s(2n-1) + n + 2}{n+1} \right) f \theta' + \text{Pr} Ec \left[A (f'')^2 + (-f'')^{n+1} \right] = 0, \quad (4.11)$$

$$f(0) = 0, \quad f'(0) = 1, \quad \theta'(0) = -\gamma [1 - \theta(0)], \quad (4.12)$$

$$f'(\infty) \rightarrow 0, \quad \theta(\infty) \rightarrow 0. \quad (4.13)$$

In the above, primes denote the differentiation with respect to η and λ represents the mixed convection parameter. Other non-dimensional parameters appearing in the above equations are R_d and Ec and they denote the thermal radiation parameter

and Eckert number, respectively. These parameters are defined mathematically as

$$\lambda = \pm \frac{g\beta r(T_f - T_\infty)}{U^2}, \quad R_d = \frac{16\sigma^* T_\infty^3}{3k^*k}, \quad Ec = \frac{U^2}{c_p(T_f - T_\infty)}. \quad (4.14)$$

It is pertinent to mention that the uniform surface temperature boundary condition is recovered for a very large generalized Biot number (i.e., $\gamma \rightarrow \infty$).

The skin friction coefficient C_{fr} and the local Nusselt number Nu_r characterize the surface drag and heat transfer rate, respectively, and are defined as

$$C_{fr} = \frac{\tau_{rz}|_{z=0}}{\frac{1}{2}\rho U^2}, \quad Nu_r = \frac{r q_w|_{z=0}}{K(T_f - T_\infty)}, \quad (4.15)$$

where τ_{rz} and q_w are the shear stress and heat flux at the sheet ($z = 0$), respectively, and are defined as

$$\tau_{rz} = \left(a + b \left| \frac{\partial u}{\partial z} \right|^{n-1} \right) \frac{\partial u}{\partial z}, \quad q_w = -K \left(\frac{\partial T}{\partial z} \right). \quad (4.16)$$

The dimensionless surface drag and transfer rate are thus given by

$$\frac{1}{2} \text{Re}_b^{\frac{1}{n+1}} C_{fr} = Af''(0) - [-f''(0)]^n, \quad \text{Re}_b^{-\frac{1}{n+1}} Nu_r = -\theta'(0). \quad (4.17)$$

4.2 Solution Methodologies

In this section we briefly state the solution methodologies.

4.2.1 The HAM Solution

The transformed governing momentum and thermal boundary layer equations (4.10) and (4.11) with the boundary conditions (4.12) and (4.13) are solved analytically by using the homotopy analysis method (HAM). For such analytic solution corresponding to the flow and heat transfer the appropriate initial guesses and linear operators are chosen as follows:

$$f_0(\eta) = 1 - e^{-\eta}, \quad \theta_0(\eta) = \frac{\gamma e^{-\eta}}{1 + \gamma}, \quad (4.18)$$

$$\mathcal{L}_f = \frac{d^3}{d\eta^3} - \frac{d}{d\eta}, \quad \mathcal{L}_\theta = \frac{d^2}{d\eta^2} - 1. \quad (4.19)$$

The obtained analytic solution of the velocity and temperature fields are highly dependent on the auxiliary parameters \hbar_f and \hbar_θ . The propitious values of these auxiliary parameters are calculated by minimizing squared residual error defined by Eq. (2.39). Figures 4.1 (a, b) represent the range of values of \hbar_f and \hbar_θ . From these ranges we have further selected the most propitious value of $\hbar_f = \hbar_\theta = -0.659219$ by minimizing the squared residual error for this specific case. Table 4.1 indicates that the series solution converges at 17th order of approximation for heat transfer analysis while at 20th order of approximation for flow analysis for some specific values of the pertinent parameters.

4.2.2 The Numerical Solution

The governing two-point boundary value problem is also solved by using the Runge-Kutta fourth order technique along with shooting method. First of all, higher order

non-linear governing differential equations are converted into simultaneous linear differential equations of first order as

$$y_1' = y_2, \quad y_2' = y_3, \quad y_3' = \frac{-1}{[A + n(-f'')^{n-1}]} \left[\left(\frac{s(2n-1) + n + 2}{n+1} \right) y_1 y_3 - s(y_2)^2 + \lambda y_4 \right], \quad (4.20)$$

$$y_4' = y_5, \quad y_5' = \frac{-Pr}{(1 + R_d)} \left[\left(\frac{s(2n-1) + n + 2}{n+1} \right) y_1 y_5 + Ec \{ A(y_3)^2 + (-y_3)^{n+1} \} \right], \quad (4.21)$$

with initial conditions

$$y_1(0) = 0, \quad y_2(0) = 1, \quad y_3(0) = s_1, \quad y_4(0) = \frac{y_5(0)}{\gamma} + 1, \quad y_5(0) = s_2, \quad (4.22)$$

where s_1 and s_2 are determined by applying the shooting technique. Then the set of initial value problem is solved using the Runge-Kutta fourth order method. The more pertinent values of the initially predicted $f''(0)$ and $\theta'(0)$, which satisfy the conditions at infinity are determined by the secant method. The iterative process continue until the desired accuracy with the tolerance less than 10^{-5} is achieved.

4.3 Graphical Results and Discussion

Extensive analytical computations have been performed to analyze the influence of the thermophysical parameters namely mixed convection parameter λ , generalized Prandtl number Pr , thermal radiation parameter R_d , generalized Biot number γ , Eckert number Ec , material parameter of the Sisko fluid A and stretching parameter s and depicted graphically through figures (4.3) to (4.10). Table 4.2 reports a comparison between present results and previously reported results and authenticate the

validity of the present solutions. Moreover, the dimensionless surface drag C_{f_r} and heat transfer rate Nu_r are reported through table 4.3. In this section, for graphical representation we have restricted default values for the pertinent parameters such as $s = A = R_d = 0.5$, $\gamma = 0.1$, $Ec = 0.2$ and $Pr = 2.0$ except for the variations or specified otherwise.

The impact of the mixed convection buoyancy parameter λ on the velocity $f'(\eta)$ and temperature $\theta(\eta)$ distributions, respectively, is depicted through figures 4.3 (a, b) for the assisting and opposing flows, respectively, with two different values of the power-law index. It should be noticed that $\lambda > 0$ relates to assisting flow (heated fluid or cooled surface), $\lambda < 0$ relates to opposing flow (cooled fluid or heated surface) and $\lambda = 0$ relates to the forced convection flow. It is anticipated by these figures that the velocity distribution increases and temperature distribution diminishes as λ increases for the assisting flow. Physically, for the assisting flow, when $\lambda (> 0)$ increases the temperature difference and impact of convective cooling increases. Consequently, the fluid flow is accelerated and the temperature diminishes. Whereas, for the opposing flow when $\lambda < 0$, an increase in λ is in negative direction corresponds to the decreasing velocity and increasing temperature profiles due to retarding influence of downward buoyancy-induced flow to that of the upward external forced flow. Further, we can notice that the effect of mixed convection parameter is more prominent in the case of assisting flow as compared to the opposing flow.

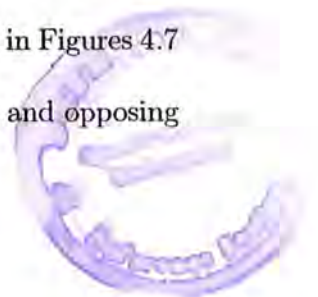
Figures 4.4 (a, b) reveal the effect of the stretching parameter s on velocity $f'(\eta)$ and temperature $\theta(\eta)$ distributions corresponding to the assisting and opposing flows. These figures show a diminishing behavior of the velocity and temperature for larger stretching parameter for both the cases. Whereas, we can observe that the thermal

boundary layer thickness is larger in case of assisting flow when comparing with the opposing flow.

Figures 4.5 (a, b) are depicted for the variation of material parameter of the Sisko fluid A to velocity $f'(\eta)$ and temperature $\theta(\eta)$ distributions for the power-law index $n = 1, 2$ corresponding to assisting ($\lambda > 0$) and opposing ($\lambda < 0$) flows. Apparently, the velocity and temperature profiles increase with the increasing values of A for both the cases. Also, a comparison of both assisting and opposing flows reveals that the temperature profile is larger in the case of opposing flow as compared to the assisting flow.

Figures 4.6 (a, b) show the velocity and temperature distributions variation for different power-law index n (for shear thinning and shear thickening fluids) corresponding to the assisting and opposing flows. These figures reveal that the velocity profile decreases for larger values of the power-law index n for both cases (i.e., shear thinning and shear thickening fluids) when taking into account the assisting flow. In case of opposing flow velocity profile decreases for shear thickening fluid, but for shear thinning fluid near the sheet the velocity profile increases while it decreases far away from the sheet. For both the assisting and opposing flows for shear thinning and shear thickening fluids temperature is a decreasing function of the power-law index; however, the effect is more prominent in case of shear thinning fluid. Also, the temperature profile is larger in case of opposing flow when compared to the assisting flow.

The variation in non-dimensional temperature distribution with the increment for a few sets of values of the thermal radiation parameter R_d is illustrated in Figures 4.7 (a, b) for the power-law index $n = 1, 2$ corresponding to the assisting and opposing



flows, respectively. It is straightforwardly appeared from these figures that the fluid temperature builds up for stronger thermal radiation. This happens because of the way that the surface heat flux increases under the influence of thermal radiation which results in increasing temperature profile inside the boundary layer region. It is also observed that thermal boundary layer thickness increases with increasing values of R_d .

The case when $Ec > 0$ ($T_f > T_\infty$) is discussed in figures 4.8 (a, b) for assisting and opposing flows. These figures reveal that the temperature distribution enhances for larger values of viscous dissipation parameter (Ec). This behavior is physically justifiable and occurs as heat energy is stored in the fluid due to frictional heating. On the other hand a decrease in the temperature distribution is revealed through figures 4.9 (a, b) for increasing values of generalized Prandtl number Pr in both the cases (assisting and resisting flows) for the power-law index $n = 1, 2$. Physically, an increase in value of the Prandtl number represents the slow rate of thermal diffusion which as a result reduces the thermal boundary layer thickness. Also, we can compare these figures to affirm that the temperature is larger in case of the opposing flow as compared to the assisting flow.

For larger values of the generalized Biot number γ the process of convective heating increases which is delineated by figures 4.10 (a, b). Physically, a larger Biot number simulates a strong surface convection which as a result provides more heat to the surface of the sheet. Further, a careful observation reveals that the temperature profile is larger in case of opposing flow compared to the assisting flow which is justifiable physically. Additionally, in these figures we have compared the analytical (HAM solution) and numerical solutions and this comparison leads us to affirmation

of the validity of the HAM results.

In table 4.2 we have presented a comparison of the present results and previously reported results for the rate of heat transfer while considering the Newtonian fluid. An observation of this table leads us to the affirmation of the present results. Table 4.3 shows the numerical values of the skin friction coefficient and Nusselt number for the power-law index $n = 1$ and 2. It can be seen straightforwardly from table 4.3 that the magnitude of the skin friction coefficient increases with increasing values of the material parameter of Sisko fluid A , stretching parameter s and the generalized Prandtl number Pr and reverse effects can be observed for the buoyancy parameter λ , thermal radiation parameter R_d , Eckert number Ec and generalized Biot number γ . Further, the magnitude of Nusselt number is an increasing function of A , s , Pr and γ whereas it decreases for λ , R_d and Ec .

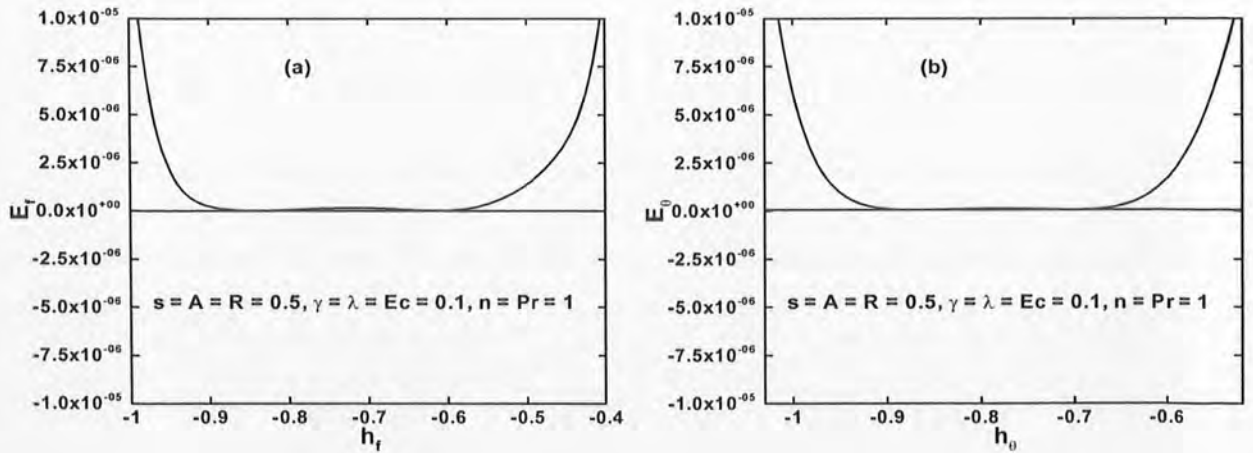


Figure 4.2: The h_f and h_θ -curves for the residual error E_f and E_θ .

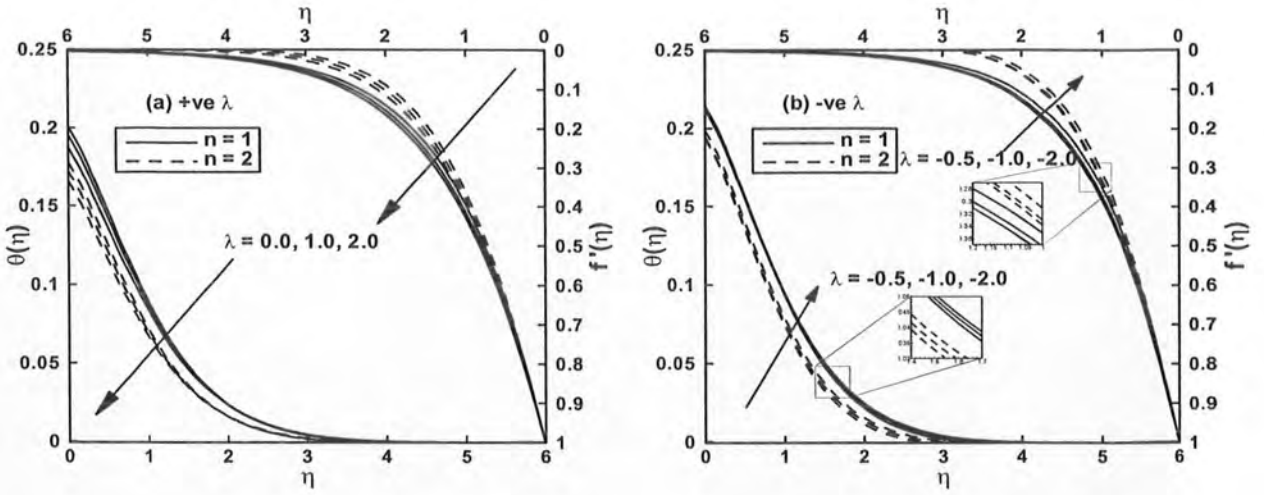


Figure 4.3: The velocity and temperature profiles for various values of λ .

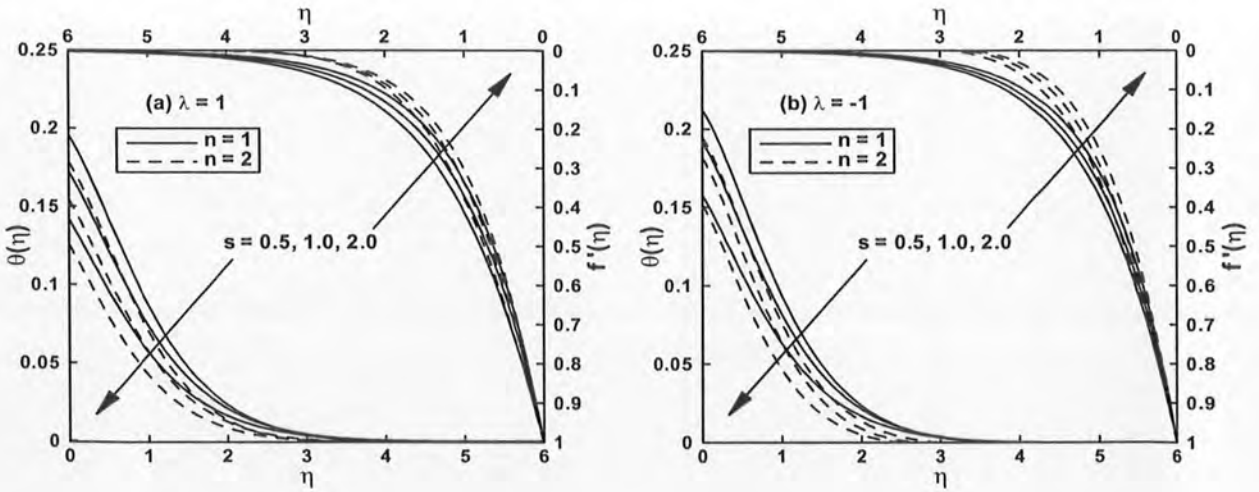


Figure 4.4: The velocity and temperature profiles for various values of s .

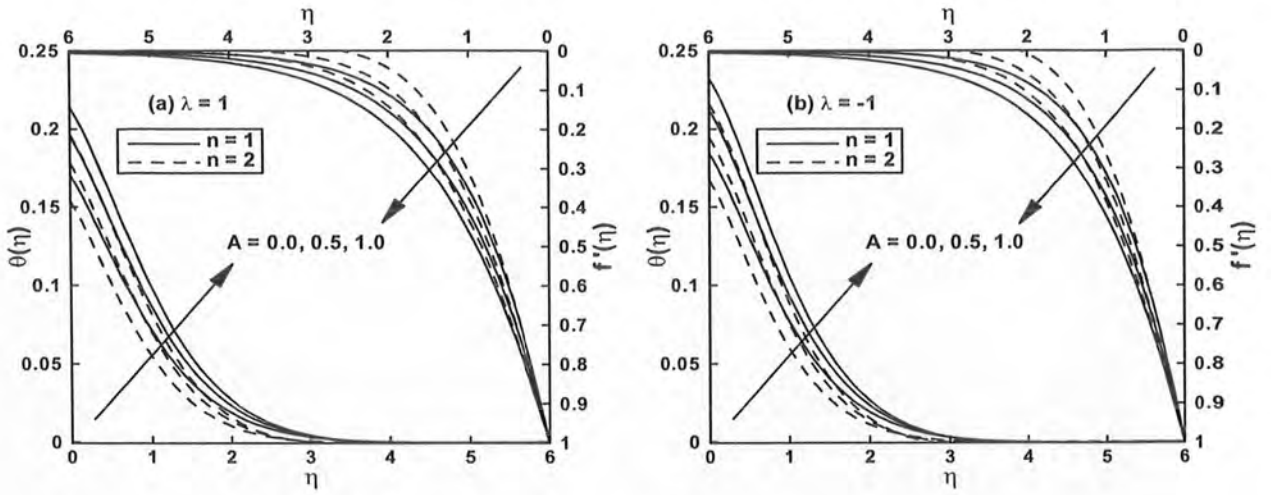


Figure 4.5: The velocity and temperature profiles for various values of A .

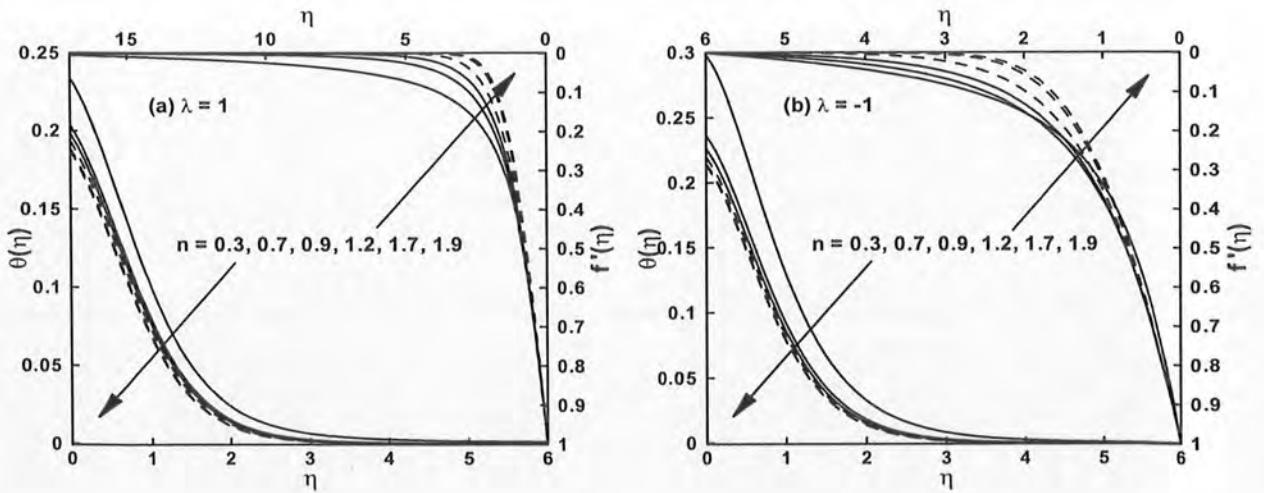


Figure 4.6: The velocity and temperature profiles for various values of n .

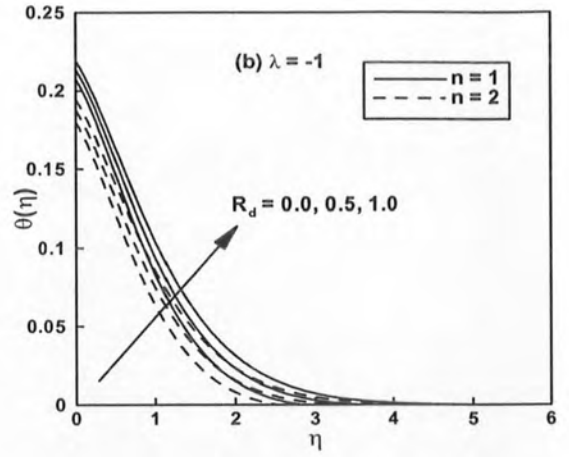
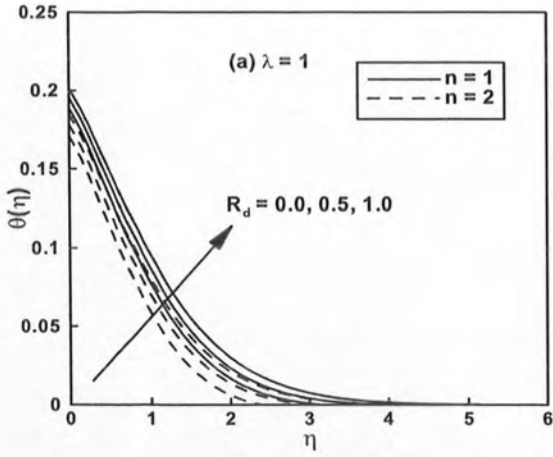


Figure 4.7: The temperature profile for various values of R_d .

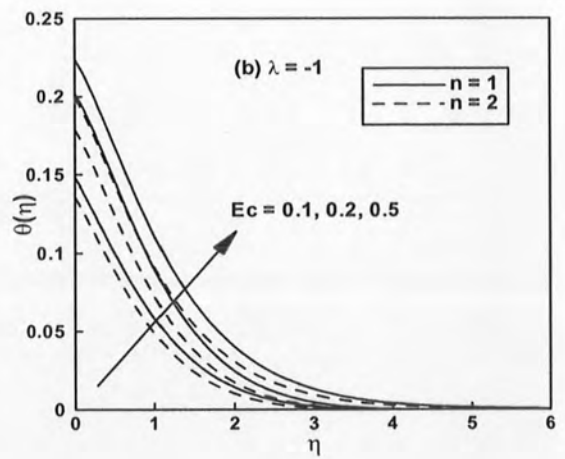
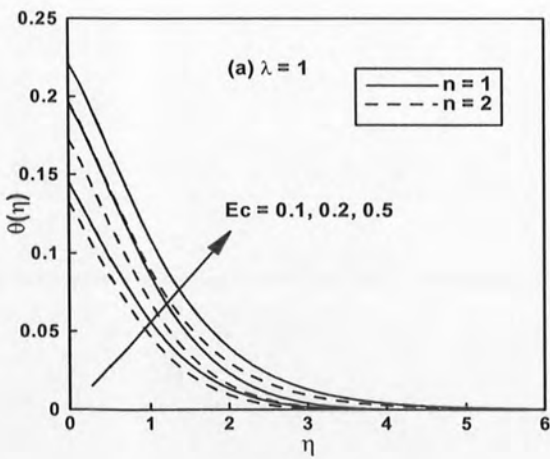


Figure 4.8: The temperature profile for various values of E_c .

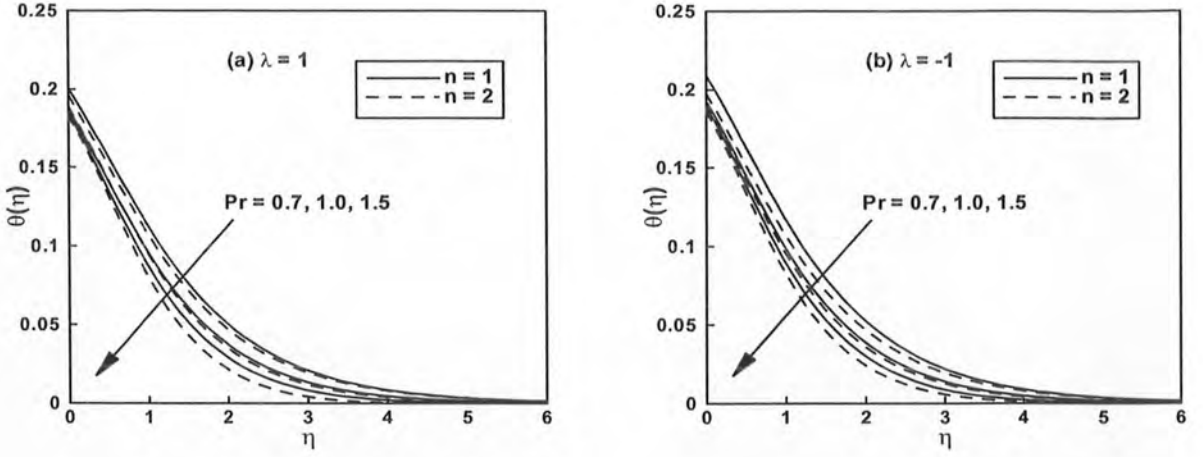


Figure 4.9: The temperature profile for various values Pr .

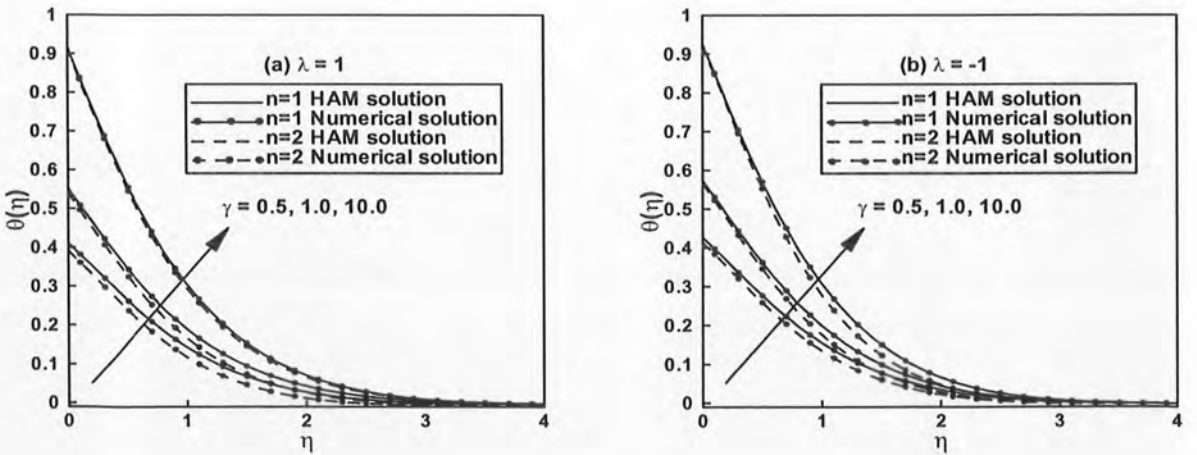


Figure 4.10: The temperature profile for various values of γ .

Table 4.1: The convergence of the homotopy solutions when $n = 1$, $s = A = R_d = 0.5$, $\gamma = Ec = \lambda = 0.1$ and $Pr = 1$ are fixed.

Order of approximation	$-f''(0)$	$-\theta'(0)$
1	0.7885170	0.0849594
5	0.8005151	0.0820715
10	0.7999408	0.0820775
12	0.7999499	0.0820763
15	0.7999398	0.0820766
17	0.7999420	0.0820765
20	0.7999416	0.0820765
22	0.7999416	0.0820765

Table 4.2: A comparison of the present results for local Nusselt number $-\theta'(0)$ for the case of Newtonian fluid ($A = \lambda = R_d = Ec = 0$, $n = s = 1$, $\gamma \rightarrow \infty$).

Pr	Present results	Khan and Pop [55]	Wang [56]	Gorla and Sidawi [57]
0.70	0.45392	0.4539	0.4539	0.5349
2.00	0.91135	0.9113	0.9114	0.9114
7.00	1.89543	1.8954	1.8954	1.8905
20.0	3.35395	3.3539	3.3539	3.3539

Table 4.3: The numerical values of $\frac{1}{2} \text{Re}_b^{\frac{1}{n+1}} C_{fr}$ and $\text{Re}_b^{-\frac{1}{n+1}} Nu_r$ for different values of physical parameters.

A	s	λ	Pr	R_d	Ec	γ	$-\frac{1}{2} \text{Re}_b^{\frac{1}{n+1}} C_{fr}$		$-\text{Re}_b^{-\frac{1}{n+1}} Nu_r$	
							n = 1	n = 2	n = 1	n = 2
0.0	0.5	0.1	1.0	0.5	0.1	0.1	0.977414	0.952207	0.081673	0.081445
	0.5						1.199913	1.092754	0.082077	0.082189
	1.0						1.387224	1.267128	0.082201	0.082481
0.5	0.5	0.1	1.0	0.5	0.1	0.1	1.199913	1.092754	0.082077	0.082189
	1.0						1.426709	1.390425	0.082188	0.083108
	2.0						1.801633	1.896802	0.082494	0.084401
0.5	0.5	0.0	1.0	0.5	0.1	0.1	1.212032	1.106874	0.081987	0.082075
		0.1					1.199913	1.092754	0.082077	0.082189
		0.5					1.153258	1.039462	0.082405	0.082597
0.5	0.5	0.1	0.7	0.5	0.1	0.1	1.195907	1.086913	0.079603	0.079407
			1.0				1.199913	1.092754	0.082077	0.082189
			2.0				1.204231	1.098648	0.085198	0.085709
0.5	0.5	0.1	1.0	0.0	0.1	0.1	1.202838	1.096813	0.084137	0.084514
				0.5			1.199913	1.092754	0.082077	0.082189
				1.0			1.196818	1.088257	0.080135	0.080003

0.5	0.5	0.1	1.0	0.5	0.0	0.1	1.203932	1.097130	0.086888	0.086682
					0.1		1.199913	1.092754	0.082077	0.082189
					0.5		1.184217	1.075842	0.063247	0.0646987
0.5	0.5	0.1	1.0	0.5	0.1	0.1	1.199913	1.092754	0.082077	0.082189
					0.5		1.182718	1.072341	0.269933	0.269067
					1.0		1.172903	1.060844	0.378441	0.376320

Chapter 5

Forced Convective Heat Transfer to Sisko Fluid Flow past a Stretching Cylinder

In this chapter, the numerical solutions are endeavored to establish for the forced convective heat transfer resulting from MHD flow of an electrically conducting Sisko fluid over an impermeable continuously stretching cylinder in its axial direction. The convective boundary conditions along with the viscous dissipation are considered. The governing equations are transformed using the local-similarity transforms and then solved numerically by using shooting technique. The results pertaining to the present study reveal that all the parameters affect the flow field and heat transfer significantly. Particularly, it is found from the analysis that the temperature is smaller in case of flow over a flat plate than that of cylinder. Further, influence of the pertinent parameters is more prominent for the shear thinning fluid when compared to the shear thickening fluid. The validation of these numerical results is affirmed by presenting a comparison with the series solutions obtained by the homotopy analysis method.



5.1 Mathematical Description of the Problem

5.1.1 Boundary Layer Equations

The mathematical modeling of governing equations for the steady axisymmetric flow of an incompressible Sisko fluid in cylindrical coordinates is discussed in this section in detail. For this purpose, we have employed the law of conservation of mass and linear momentum defined by Eqs. (2.1) and (2.2), respectively, along with the extra stress tensor for an incompressible Sisko fluid which is defined through Eq. (2.5). For an axisymmetric flow, the velocity and stress fields have the form

$$\mathbf{V} = [v(r, x), 0, u(r, x)], \quad \mathbf{S} = \mathbf{S}(r, x), \quad (5.1)$$

where (r, x) denotes the cylindrical coordinate, u and v are the velocity components along x - and r - directions, respectively.

In view of Eqs. (2.1), (2.2) and (5.1), in the absence of the body forces, one has

$$\frac{\partial(ru)}{\partial x} + \frac{\partial(rv)}{\partial r} = 0, \quad (5.2)$$

$$\rho \left(v \frac{\partial u}{\partial r} + u \frac{\partial u}{\partial x} \right) = -\frac{\partial p}{\partial x} + \frac{1}{r} \frac{\partial(rS_{rx})}{\partial r} + \frac{\partial S_{xx}}{\partial x}, \quad (5.3)$$

$$\rho \left(v \frac{\partial v}{\partial r} + u \frac{\partial v}{\partial x} \right) = -\frac{\partial p}{\partial r} + \frac{\partial S_{rr}}{\partial x} + \frac{\partial S_{rx}}{\partial r} + \frac{S_{rr} - S_{\theta\theta}}{r}. \quad (5.4)$$

Also, the components of extra stress tensor \mathbf{S} defined by Eq. (5.1) can be expressed as

$$S_{rr} = \left[\left\{ a + b \left| 2 \left(\frac{\partial v}{\partial r} \right)^2 + 2 \left(\frac{\partial u}{\partial x} \right)^2 + \left(\frac{\partial v}{\partial x} + \frac{\partial u}{\partial r} \right)^2 \right|^{\frac{n-1}{2}} \right\} \left(2 \frac{\partial v}{\partial r} \right) \right], \quad (5.5)$$

$$S_{xx} = \left[\left\{ a + b \left| 2 \left(\frac{\partial v}{\partial r} \right)^2 + 2 \left(\frac{\partial u}{\partial x} \right)^2 + \left(\frac{\partial v}{\partial x} + \frac{\partial u}{\partial r} \right)^2 \right|^{\frac{n-1}{2}} \right\} \left(2 \frac{\partial u}{\partial x} \right) \right], \quad (5.6)$$

$$S_{\theta\theta} = \left[\left\{ a + b \left| 2 \left(\frac{\partial v}{\partial r} \right)^2 + 2 \left(\frac{\partial u}{\partial x} \right)^2 + \left(\frac{\partial v}{\partial x} + \frac{\partial u}{\partial r} \right)^2 \right|^{\frac{n-1}{2}} \right\} \left(2 \frac{v}{r} \right) \right], \quad (5.7)$$

$$S_{xr} = S_{rx} = \left[\left\{ a + b \left| 2 \left(\frac{\partial v}{\partial r} \right)^2 + 2 \left(\frac{\partial u}{\partial x} \right)^2 + \left(\frac{\partial v}{\partial x} + \frac{\partial u}{\partial r} \right)^2 \right|^{\frac{n-1}{2}} \right\} \left(\frac{\partial v}{\partial x} + \frac{\partial u}{\partial r} \right) \right], \quad (5.8)$$

with $S_{r\theta} = S_{\theta r} = S_{\theta x} = S_{x\theta} = 0$.

Equations (5.3) and (5.4), after the substitution of expressions defined through Eqs. (5.5) – (5.8), take the form

$$\begin{aligned} \rho \left(v \frac{\partial v}{\partial r} + u \frac{\partial v}{\partial x} \right) &= -\frac{\partial p}{\partial r} + a \left(\frac{\partial^2 v}{\partial r^2} + \frac{\partial^2 v}{\partial x^2} + \frac{\partial}{\partial r} \left(\frac{v}{r} \right) \right) + 2b \frac{\partial}{\partial r} \left(\frac{\partial v}{\partial r} J \right) \\ &\quad + b \frac{\partial}{\partial x} \left\{ \left(\frac{\partial v}{\partial x} + \frac{\partial u}{\partial r} \right) J \right\} + 2bJ \frac{\partial}{\partial r} \left(\frac{v}{r} \right), \end{aligned} \quad (5.9)$$

$$\begin{aligned} \rho \left(v \frac{\partial u}{\partial r} + u \frac{\partial u}{\partial x} \right) &= -\frac{\partial p}{\partial x} + a \left(\frac{\partial^2 u}{\partial r^2} + \frac{\partial^2 u}{\partial x^2} + \frac{1}{r} \frac{\partial u}{\partial r} \right) + 2b \frac{\partial}{\partial x} \left\{ \frac{\partial u}{\partial x} J \right\} \\ &\quad + b \frac{\partial}{\partial r} \left\{ \left(\frac{\partial v}{\partial x} + \frac{\partial u}{\partial r} \right) J \right\} + \frac{b}{r} \left(\frac{\partial v}{\partial x} + \frac{\partial u}{\partial r} \right) J, \end{aligned} \quad (5.10)$$

where

$$J = \left| 2 \left(\frac{\partial v}{\partial r} \right)^2 + 2 \left(\frac{\partial u}{\partial x} \right)^2 + \left(\frac{\partial v}{\partial x} + \frac{\partial u}{\partial r} \right)^2 \right|^{\frac{n-1}{2}}. \quad (5.11)$$

The implementation of the usual boundary layer approximations to Eqs. (5.9) and (5.10) leads us to the following equations

$$\rho \left(v \frac{\partial u}{\partial r} + u \frac{\partial u}{\partial x} \right) = -\frac{\partial p}{\partial x} + a \frac{\partial^2 u}{\partial r^2} + \frac{b}{\rho r} \frac{\partial}{\partial r} \left(r \frac{\partial u}{\partial r} \left| \frac{\partial u}{\partial r} \right|^{n-1} \right), \quad (5.12)$$

$$0 = -\frac{\partial p}{\partial r}. \quad (5.13)$$

5.1.2 Geometry of the Problem

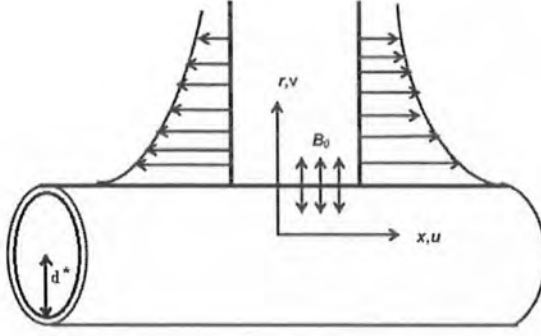


Figure 5.1: Physical model and coordinate system.

5.1.3 Governing Equations

Consider the steady axisymmetric flow of an incompressible non-Newtonian Sisko fluid along a horizontal impermeable stretching cylinder of radius d^* in the presence of uniform magnetic field. The x and r are the cylindrical polar coordinates measuring the distance in axial and radial directions, respectively. It is assumed that a uniform magnetic field of intensity B_0 acts in the radial direction. The magnetic Reynolds number is assumed to be small so that the induced magnetic field is negligible in comparison with the applied magnetic field. The above assumptions along with the usual boundary layer approach lead us to the continuity, momentum and energy equations (2.1) to (2.5) (in the presence of viscous dissipation) of the form of Eq.

(5.2) and the equations given as follows:

$$u \frac{\partial u}{\partial x} + v \frac{\partial u}{\partial r} = \frac{a}{\rho r} \frac{\partial}{\partial r} \left(r \frac{\partial u}{\partial r} \right) - \frac{b}{\rho r} \left(-\frac{\partial u}{\partial r} \right)^n + \frac{bn}{\rho} \left(-\frac{\partial u}{\partial r} \right)^{n-1} \frac{\partial^2 u}{\partial r^2} - \frac{\sigma B_0^2}{\rho} u, \quad (5.14)$$

$$u \frac{\partial T}{\partial x} + v \frac{\partial T}{\partial r} = \alpha \left[\frac{\partial^2 T}{\partial r^2} + \frac{1}{r} \frac{\partial T}{\partial r} \right] + \frac{a}{\rho c_p} \left(\frac{\partial u}{\partial r} \right)^2 + \frac{b}{\rho c_p} \left(-\frac{\partial u}{\partial r} \right)^{n+1}. \quad (5.15)$$

Here the last two terms on the right side of Eq. (5.15) are appearing due to viscous dissipation, i.e., the rate at which mechanical energy of the flow is converted to heat.

5.1.4 Boundary Conditions

The appropriate boundary conditions for the velocity and temperature fields in the present problem are

$$u(r, x) = U = cx, \quad v(r, x) = 0, \quad k \frac{\partial T(r, x)}{\partial r} = -h_f [T_f - T(r, x)] \quad \text{at } r = d^*, \quad (5.16)$$

$$u \rightarrow 0, \quad T \rightarrow T_\infty \quad \text{as } r \rightarrow \infty, \quad (5.17)$$

where c is a positive real number and d^* the radius of the cylinder.

5.1.5 Transformed Problem

The incompressibility condition (5.2) is automatically satisfied by the stream function

ψ such that $u = \frac{1}{r} \frac{\partial \psi}{\partial r}$, $v = -\frac{1}{r} \frac{\partial \psi}{\partial x}$. Introducing the local-similarity transforms as

follows:

$$\eta = \frac{r^2 - d^{*2}}{2d^*x} \text{Re}_b^{\frac{1}{n+1}}, \quad \psi = -Ud^*x \text{Re}_b^{-\frac{1}{n+1}} f(\eta), \quad \theta(\eta) = \frac{T - T_\infty}{T_f - T_\infty}. \quad (5.18)$$

Upon the substitution of the local-similarity transformations (5.18), the above governing equations (5.14) – (5.15) along with the boundary conditions (5.16) and (5.17) reduce to

$$(1 + 2\eta M)Af''' + 2MAf'' - M(1 + n)(1 + 2\eta M)^{\frac{n-1}{2}} (-f'')^n + \frac{2n}{n+1}ff'' - (f')^2 + n(1 + 2\eta M)^{\frac{n+1}{2}} (-f'')^{n-1} f''' - D^2f' = 0, \quad (5.19)$$

$$(1 + 2\eta M)\theta'' + 2M\theta' + (1 + 2\eta M)A\text{EcPr}(-f'')^2 + (1 + 2\eta M)^{\frac{n+1}{2}} \text{EcPr}(-f'')^{n+1} + \frac{2n}{n+1} \text{Pr}f\theta' = 0, \quad (5.20)$$

$$f(0) = 0, \quad f'(0) = 1, \quad \theta'(0) = -\gamma[1 - \theta(0)], \quad (5.21)$$

$$f'(\eta) \rightarrow 0, \quad \theta(\eta) \rightarrow 0 \text{ as } \eta \rightarrow \infty. \quad (5.22)$$

In the above transformed equations, differentiation with respect to η is represented by primes. Further, for Sisko fluid, the material parameter A , the magnetic parameter D , the curvature parameter M , Re_a and Re_b the local Reynolds numbers corresponding to Newtonian and power-law fluids, the generalized Prandtl number Pr and the generalized Biot number γ appearing in above equations are defined as



follows:

$$\begin{aligned} \text{Re}_a &= \frac{\rho x U}{a}, \quad \text{Re}_b = \frac{\rho x^n U^{2-n}}{b}, \quad A = \frac{\text{Re}_b^{\frac{2}{n+1}}}{\text{Re}_a}, \quad D^2 = \frac{\sigma B_0^2}{\rho U} x, \\ M &= \frac{x}{d^*} \text{Re}_b^{-\frac{1}{n+1}}, \quad \gamma = \frac{h_f}{k} x \text{Re}_b^{-\frac{1}{n+1}}, \quad \text{Pr} = \frac{x U}{\alpha} \text{Re}_b^{-\frac{2}{n+1}}. \end{aligned} \quad (5.23)$$

5.1.6 Physical Quantities

The surface drag and rate of heat transfer characterized by the skin friction coefficient C_{fx} and the local Nusselt number Nu_x are defined as

$$C_{fx} = \frac{\tau_{rx}|_{r=d^*}}{\frac{1}{2}\rho U^2}, \quad Nu_x = \frac{x q_w|_{r=d^*}}{k (T_f - T_\infty)}, \quad (5.24)$$

where τ_{rx} and q_w are defined as

$$\tau_{rx} = \left(a + b \left| \frac{\partial u}{\partial r} \right|^{n-1} \right) \frac{\partial u}{\partial r}, \quad q_w = -k \left(\frac{\partial T}{\partial r} \right), \quad (5.25)$$

where a and b are the material constants of Sisko fluid representing the viscosity at high shear rate and consistency index, respectively.

The dimensionless form of the local skin friction and heat transfer rate are given as

$$\frac{1}{2} \text{Re}_b^{\frac{1}{n+1}} C_{fx} = A f''(0) - [-f''(0)]^n, \quad \text{Re}_b^{-\frac{1}{n+1}} Nu_x = -\theta'(0). \quad (5.26)$$

5.2 Solution Methodologies

5.2.1 The Numerical Solution

The local-similar non-linear coupled ordinary differential equations (5.19) and (5.20) subject to boundary conditions (5.21) and (5.22) are solved by utilizing the shooting technique, by transforming the boundary value problem (BVP) into set of initial value problems (IVPs). We have introduced the new set of dependent variables y_1 , y_2 , y_3 , y_4 , y_5 and set the following system of five first order ordinary differential equations

$$y_1' = y_2, y_2' = y_3, y_3' = - \left[\frac{2MAy_3 - M(1+n)(1+2\eta M)^{\frac{n-1}{2}} (-y_3)^n + \frac{2n}{n+1} y_1 y_3 - (y_2)^2 - D^2 y_2}{(1+2\eta M)A + n(1+2\eta M)^{\frac{n+1}{2}} (-y_3)^{n-1}} \right], \quad (5.27)$$

$$y_4' = y_5, y_5' = - \frac{1}{(1+2\eta M)} \left[(1+2\eta M)A Ec Pr (-y_3)^2 + (1+2\eta M)^{\frac{n+1}{2}} Ec Pr (-y_3)^{n+1} + 2M y_4' + \frac{2n}{n+1} Pr y_1 y_4' \right], \quad (5.28)$$

with boundary conditions

$$y_1(0) = 0, y_2(0) = 1, y_5(0) = -\gamma[1 - y_4(0)]. \quad (5.29)$$

To solve Eqs. (5.27) and (5.28) subject to conditions (5.29) as an IVP we need values for $y_3(0)$ and $y_5(0)$ but these value are not defined in the problem under consideration. The initial guesses for $y_3(0)$ and $y_5(0)$ are chosen and then the solution is obtained by applying the Runge-Kutta method. The better approximation for solution is obtained by adjusting the initial guesses using the Newton's method.

5.2.2 The Homotopic Solution

The homotopy analysis method proposed by Liao [58] is based on the fundamental concept of topology called homotopy. When a function/equation can be deformed into another function/equation continuously then these functions/equations are called homotopic. Nowadays, this method is widely used to solve highly non-linear problems. This method gives us huge freedom to choose initial guesses and linear operators as follows:

$$f_0(\eta) = 1 - e^{-\eta}, \quad \theta_0(\eta) = \frac{\gamma e^{-\eta}}{1 + \gamma}, \quad (5.30)$$

$$\mathcal{L}_f = \frac{d^3}{d\eta^3} - \frac{d}{d\eta}, \quad \mathcal{L}_\theta = \frac{d^2}{d\eta^2} - 1, \quad (5.31)$$

which satisfy the conditions

$$\mathcal{L}_f [C_1 + C_2 e^\eta + C_3 e^{-\eta}] = 0, \quad (5.32)$$

$$\mathcal{L}_\theta [C_4 e^\eta + C_5 e^{-\eta}] = 0. \quad (5.33)$$

To ensure the convergence of these series solutions the idea of diagramming \hbar -curves was introduced, which provides an acceptable range of values of auxiliary parameter. However, instead of choosing a random value from this whole range the idea of minimized squared residual error (ch. Chapter 2, Eq. (2.39)) was introduced which provides only one most appropriate value of the auxiliary parameter.

5.3 Results and Discussion

The numerical computation has been carried out for different values of the magnetic parameter D , the curvature parameter M , the generalized Prandtl number Pr , the generalized Biot number γ and the Eckert number Ec . In order to get a clear insight into the physical problem, the velocity and temperature profiles for both shear thinning ($n < 1$) and thickening ($n > 1$) cases are discussed when considering the flow past the cylinder as well as flat plate. The numerical results are shown graphically through figures 5.2 to 5.7. The influence of the pertinent parameters on the skin friction, i.e., drag experienced by the surface and the wall temperature gradient, i.e., the rate of heat transfer from surface to fluid for shear thinning and thickening cases are tabulated in tables 5.1 and 5.2.

The impact of the power-law index n on the velocity profile is depicted through figures 5.2 (a, b) corresponding to shear thinning ($n < 1$) and shear thickening ($n > 1$) fluids, respectively. Also, a comparison between flow past a flat plate ($M = 0$) and a cylinder ($M = 0.5$) is performed. The observation of these figures leads us to the fact that velocity profile decreases with increasing values of the power-law index n . Further, the momentum boundary layer thickness is larger in case of shear thinning fluid as compared to the shear thickening fluid.

Figures 5.3 (a, b) exhibit the temperature distribution corresponding to the power-law index $n < 1$ and $n > 1$ for both the cases of flat plate ($M = 0$) and cylinder ($M = 0.5$), respectively. A careful observation reveals that the temperature decreases with increasing values of the power-law index n . Additionally, the magnitude of temperature is larger in case of the shear thinning fluid than the shear

thickening fluid. Also, the thermal boundary layer is larger in the case of cylinder when compared to flat plate.

In figures 5.4 (a, b) the influence of viscous dissipation parameter i.e., Eckert number Ec , on the temperature profile is exhibited for shear thinning and shear thickening fluids, respectively. The Eckert number represents the relationship between the enthalpy and the kinetic energy in the flow. It expresses the transformation of kinetic energy into internal energy due to work done against the viscous fluid stresses. It can be seen from these figures that the effect of viscous dissipation leads to an increase in the temperature profiles in case of shear thinning as well as shear thickening fluids. Moreover, it is noticed that the thermal boundary layer thickness is larger for the shear thinning fluid as compared to the shear thickening fluid. Further, the influence of Ec is more prominent for the cylinder when compared to the flat plate.

The variation of temperature $\theta(\eta)$ with η for different values of the generalized Biot number γ is presented through figures 5.5 (a, b) corresponding to shear thinning and shear thickening fluids. An observation reveals that the temperature field increases rapidly near the boundary for larger Biot number. Physically, an increasing γ represents the hot fluid convection resistance decreases and consequently the surface temperature along with the thermal boundary layer thickness increases. Also, we can observe that the temperature profile is smaller in case of flat plate when compared to the stretching cylinder case.

It is observed that with increasing generalized Prandtl number Pr the temperature diminishes (figures 5.6 (a, b)). An increment in the value of the Prandtl number reduces the thermal boundary layer thickness. The physical reason behind temper-

ature diminishing with increasing Pr is that the higher Prandtl number fluids have lower thermal conductivity (or a higher viscosity) which results in thinning the thermal boundary layer and consequently, higher heat transfer rate at the surface. It is likewise observed that more prominent effects of Pr can be seen for stretching cylinder when compared to flat plate. The Prandtl number signifies the ratio of the momentum diffusivity to thermal diffusivity. Fluids having lower Prandtl number will possess higher thermal conductivities and hence thicker thermal boundary layer structures so that heat can diffuse from the wall faster than for the fluids with higher Pr . Thus, Prandtl number can be utilized to control the rate of cooling in conducting flows.

The impact of the curvature parameter M on the temperature distribution is elucidated through figure 5.7 (a) for both the cases, i.e., shear thinning and shear thickening fluids. The transverse curvature parameter represents the geometrical property of a cylinder. An increase in the transverse curvature parameter M shows that the cylinder radius is decreasing i.e., cylinder is getting slender. It is clear from this figure that increasing curvature parameter increases the temperature profile which is justifiable physically. Further, the magnitude of temperature is larger for the shear thinning fluid when compared to the shear thickening fluid. The obtained numerical results are compared graphically with the HAM results through figure 5.7 (b) by which the validity of numerical results is affirmed.

Tables 5.1 and 5.2 are numeric representation of the skin friction and heat transfer coefficients, respectively. It appears from table 5.1 that magnitude of the skin friction increases with increasing values of the material parameter A of Sisko fluid, curvature parameter M and magnetic parameter D for shear thinning ($n = 0.5$) and shear

thickening ($n = 1.5$) fluids, respectively. From table 5.2 an assisting behavior is observed for the rate of heat transfer with the increasing values of A , M , Pr and γ . The reverse behavior can be seen for the parameters D and Ec for both the shear thinning and thickening fluids. Further, it can be noticed that the rate of heat transfer is larger in shear thickening fluid as compared to the shear thinning fluid.

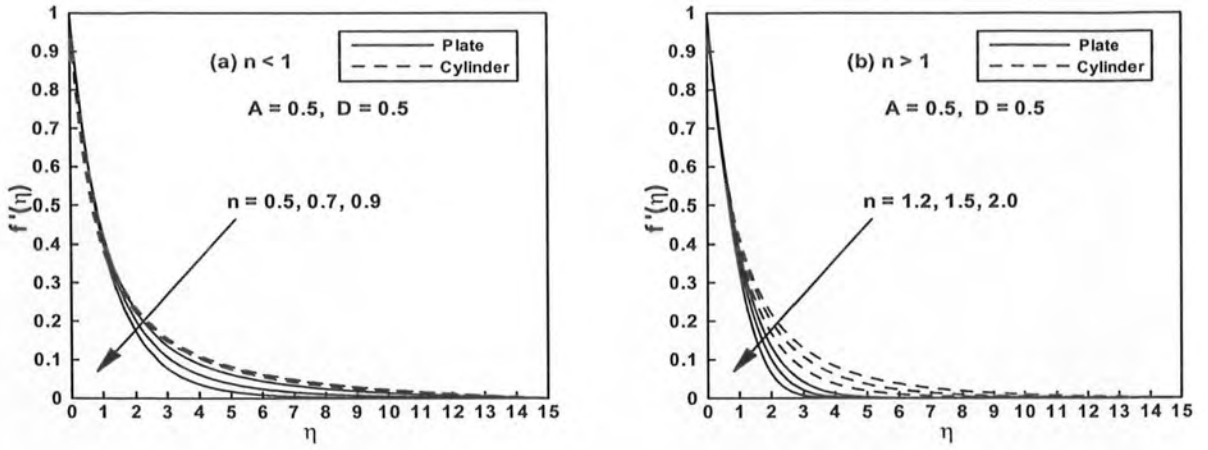


Figure 5.2: The velocity profiles $f'(\eta)$ for different values of the power-law index n .

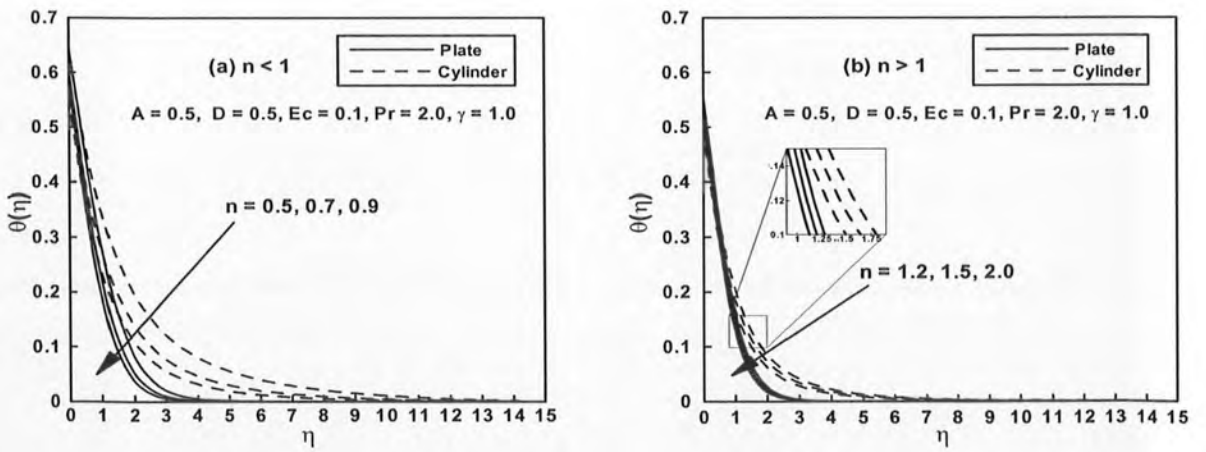


Figure 5.3: The temperature profiles $\theta(\eta)$ for different values of the power-law index

n .

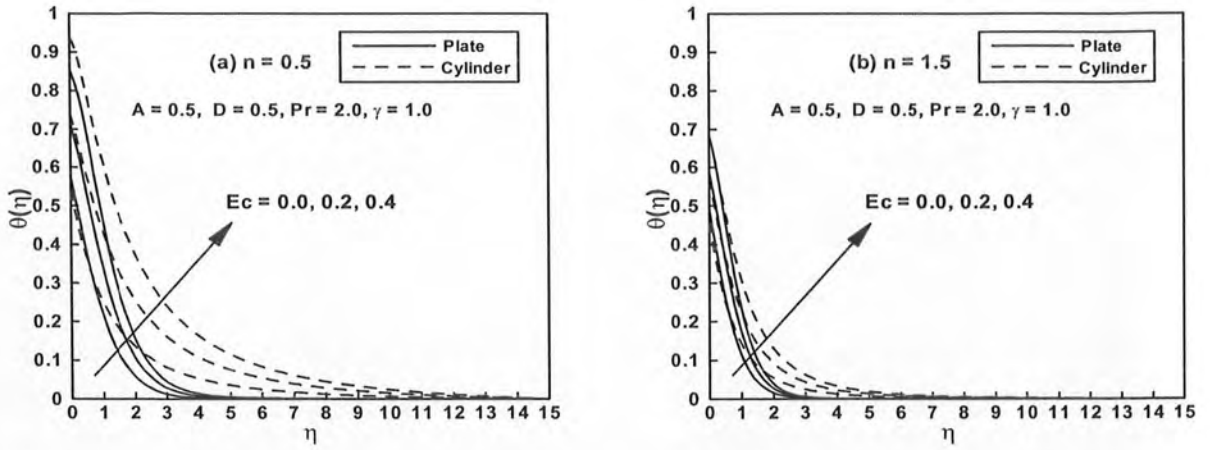


Figure 5.4: The temperature profiles $\theta(\eta)$ for different values of the Eckert number Ec .

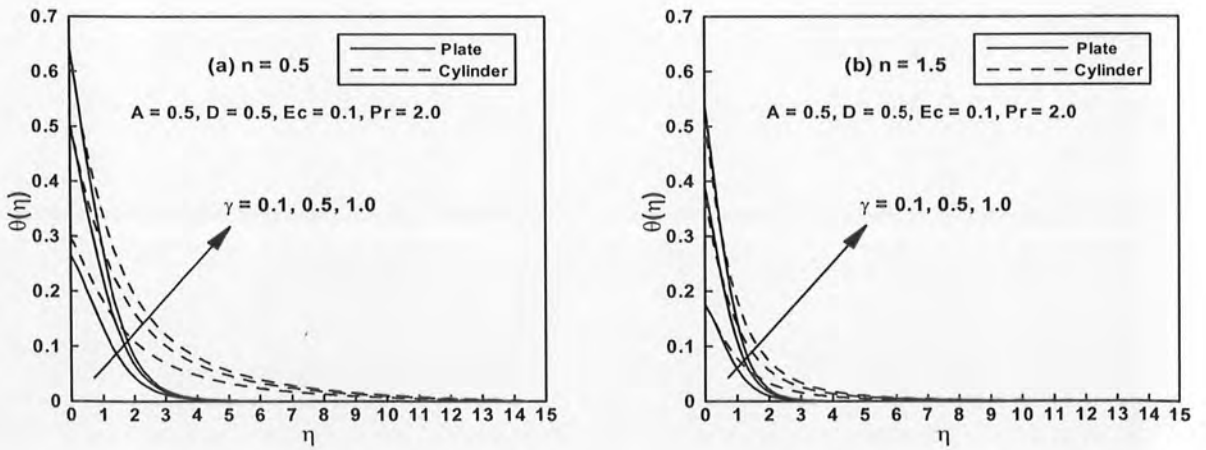


Figure 5.5: The temperature profiles $\theta(\eta)$ for different values of the generalized Biot number γ .

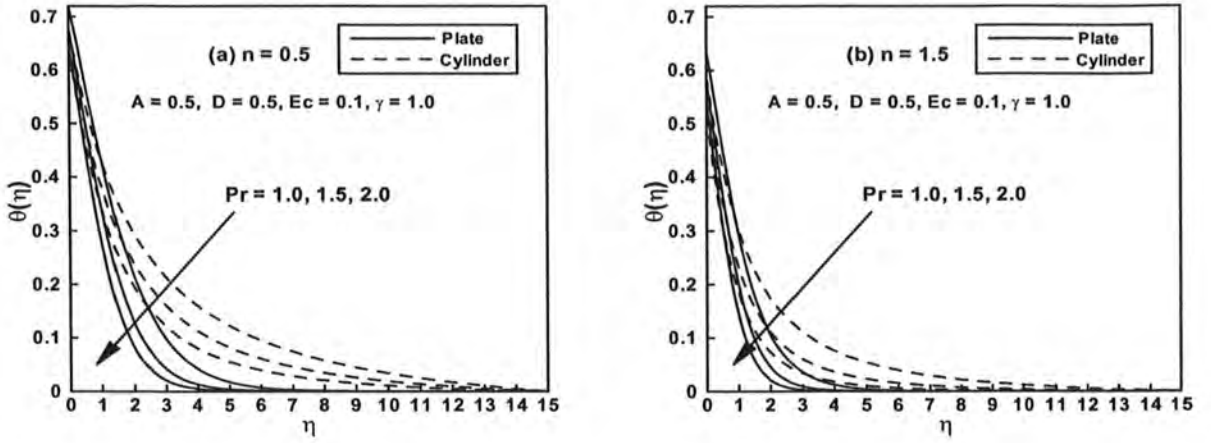


Figure 5.6: The temperature profiles $\theta(\eta)$ for different values of the generalized Prandtl number Pr .

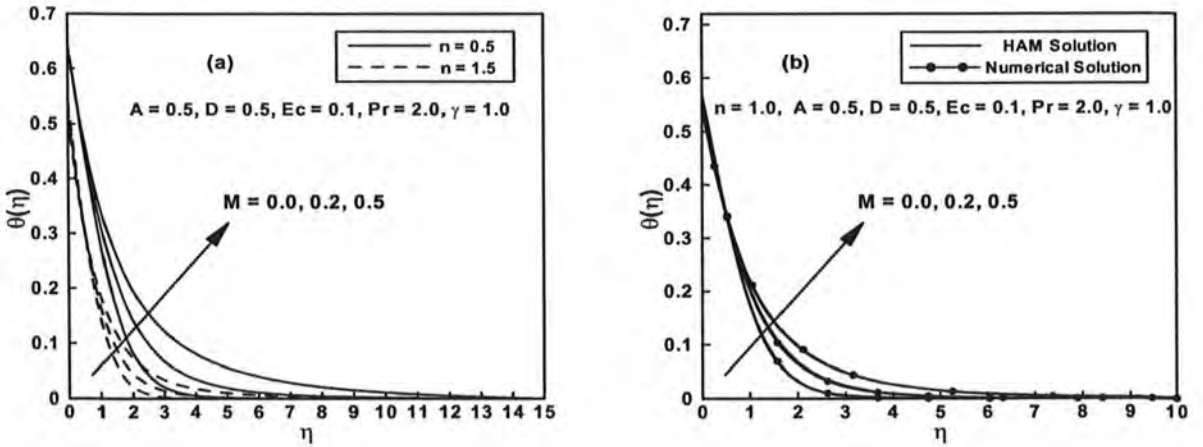


Figure 5.7: The temperature profiles $\theta(\eta)$ for different values of the curvature parameter M .



Table 5.1: Numerical values of the skin friction coefficient $\frac{1}{2} \text{Re}_b^{\frac{1}{n+1}} C_{fx}$ for different values of physical parameters.

A	M	D	$-\frac{1}{2} \text{Re}_b^{\frac{1}{n+1}} C_{fx}$	
			$n = 0.5$	$n = 1.5$
0.0	0.5	0.5	1.383363	1.266408
0.2			1.573023	1.395741
0.5			1.814601	1.582075
0.5	0.0	0.5	1.468768	1.322765
	0.5		1.814601	1.582075
	1.0		2.112396	1.827893
0.5	0.5	0.0	1.680884	1.415256
		0.5	1.814601	1.582075
		1.0	2.131422	1.998189



Table 5.2: Numerical values of the local Nusselt number $\text{Re}_b^{-\frac{1}{n+1}} Nu_x$ for different values of physical parameters.

A	M	D	γ	Pr	Ec	$-\text{Re}_b^{-\frac{1}{n+1}} Nu_x$	
						$n = 0.5$	$n = 1.5$
0.0	0.5	0.5	1.0	2.0	0.1	0.354105	0.483021
						0.358524	0.484596
						0.361048	0.484924
0.5	0.0	0.5	1.0	2.0	0.1	0.354322	0.457980
						0.361048	0.484924
						0.382701	0.509606
0.5	0.5	0.0	1.0	2.0	0.1	0.380822	0.498058
						0.361048	0.484924
						0.313702	0.451704
0.5	0.5	1.0	0.1	2.0	0.1	0.070281	0.082577
						0.247346	0.314604
						0.361048	0.484924
0.5	0.5	1.0	1.0	0.7	0.1	0.305194	0.375966
						0.320799	0.410927
						0.361048	0.484924
0.5	0.5	0.5	1.0	2.0	0.0	0.459688	0.541380
						0.262408	0.428467
						0.065130	0.315556

Chapter 6

Nonlinear Radiative Heat Transfer to Stagnation-Point Flow of Sisko Fluid past a Stretching Cylinder

In the present chapter, we endeavor to perform a numerical analysis in connection with the non-linear radiative stagnation-point flow and heat transfer to Sisko fluid past a stretching cylinder in the presence of convective boundary conditions. In energy equation the radiative heat flux term was introduced by using the non-linear Rosseland approximation. This gives rise to an additional parameter known as the temperature ratio parameter by which the temperature and heat transfer characteristics are highly affected. The numerical solutions of transformed governing equations are calculated through the fourth order Runge-Kutta method using shooting technique. With the help of graphs and tables, the influence of non-dimensional parameters on the velocity and temperature along with the local skin friction and Nusselt number is discussed. The results reveal that the temperature and corresponding thermal boundary layer increase; however, heat transfer from the surface of cylinder decreases with increasing values of the thermal radiation and temperature ratio parameters. Moreover, the authenticity of numerical solutions is validated by finding their good agreement with the HAM solutions.

6.1 Problem Formulation

6.1.1 Physical Model

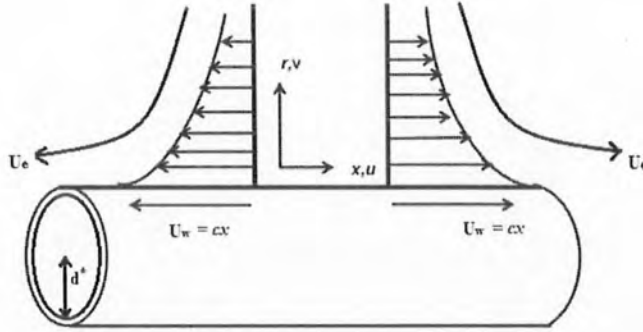


Figure 6.1: Sketch of the physical model and coordinate system.

6.1.2 Governing Equations

Let us assume the steady two-dimensional stagnation-point flow of an incompressible Sisko fluid past a horizontal cylinder of radius d^* stretching with linear velocity along the axis of the cylinder (see figure 6.1). The x and r measure the distance along axial and radial directions, respectively. Let the surface of cylinder is being heated by the hot fluid having temperature T_f which provides heat transfer coefficient h_f . Implementing the boundary layer approach along with the above mentioned assumptions the continuity, momentum and energy equations (2.1) to (2.3) along with Eqs. (2.4) and (2.5) in the absence of viscous dissipation take the form:

$$\frac{\partial(rv)}{\partial r} + \frac{\partial(ru)}{\partial x} = 0, \quad (6.1)$$

$$u \frac{\partial u}{\partial x} + v \frac{\partial u}{\partial r} = -\frac{1}{\rho} \frac{\partial p}{\partial x} + \frac{a}{\rho r} \frac{\partial}{\partial r} \left(r \frac{\partial u}{\partial r} \right) + \operatorname{sgn} \left[\frac{d}{c} - 1 \right] \frac{b}{\rho r} \left\{ \operatorname{sgn} \left[\frac{d}{c} - 1 \right] \frac{\partial u}{\partial y} \right\}^n + \frac{bn}{\rho} \left\{ \operatorname{sgn} \left[\frac{d}{c} - 1 \right] \frac{\partial u}{\partial r} \right\}^{n-1} \frac{\partial^2 u}{\partial r^2}, \quad (6.2)$$

$$u \frac{\partial T}{\partial x} + v \frac{\partial T}{\partial r} = \alpha \left(\frac{\partial^2 T}{\partial r^2} + \frac{1}{r} \frac{\partial T}{\partial r} \right) - \frac{1}{\rho c_p} \frac{\partial q_r}{\partial r}. \quad (6.3)$$

Here $\operatorname{sgn}[\cdot]$ represents the sign function and q_r the non-linear radiative heat flux.

The non-linear radiative heat flux q_r via Rosseland's approximation is given as

$$q_r = -\frac{4\sigma^*}{3k^*} \frac{\partial T^4}{\partial r} = -\frac{16\sigma^*}{3k^*} T^3 \frac{\partial T}{\partial r}, \quad (6.4)$$

where the σ^* and k^* are the Stefan-Boltzmann constant and the mean absorption coefficient, respectively. In view of Eq. (6.4), Eq. (6.3) after simplification takes the form

$$u \frac{\partial T}{\partial x} + v \frac{\partial T}{\partial r} = \alpha \left(\frac{\partial^2 T}{\partial r^2} + \frac{1}{r} \frac{\partial T}{\partial r} \right) + \frac{16\sigma^*}{3k^* \rho c_p} \left(T^3 \frac{\partial^2 T}{\partial r^2} + 3T^2 \left(\frac{\partial T}{\partial r} \right)^2 \right). \quad (6.5)$$

6.1.3 Boundary Conditions

The associated boundary conditions for the velocity and temperature fields for the problem under consideration are

$$u(r, x) = U_w = cx, \quad v(r, x) = 0, \quad k \frac{\partial T(r, x)}{\partial r} = -h_f [T_f - T(r, x)] \quad \text{at } r = d^*, \quad (6.6)$$

$$u = U_e = dx, \quad T \rightarrow T_\infty \quad \text{as } r \rightarrow \infty. \quad (6.7)$$

Here c and d are positive real numbers, U_e and U_w represent the free stream

velocity and velocity of fluid at the boundary, respectively.

6.1.4 Local-Similarity Transformations

The local-similarity transformations are given as follows:

$$\eta = \frac{r^2 - d^{*2}}{2d^*x} \text{Re}_b^{\frac{1}{n+1}}, \quad \psi = -U_w d^* x \text{Re}_b^{-\frac{1}{n+1}} f(\eta), \quad \theta(\eta) = \frac{T - T_\infty}{T_f - T_\infty}. \quad (6.8)$$

The substitution of introduced local-similarity transformations (6.8) into Eqs. (6.1), (6.2) and (6.5) leads to the governing ordinary differential equations as given below:

$$(1 + 2\eta M) A f''' + 2M A f'' + \text{sgn} \left[\frac{d}{c} - 1 \right] M(1 + n)(1 + 2\eta M)^{\frac{n-1}{2}} \left(\text{sgn} \left[\frac{d}{c} - 1 \right] f'' \right)^n + \frac{2n}{n+1} f f'' - (f')^2 + n(1 + 2\eta M)^{\frac{n+1}{2}} \left(\text{sgn} \left[\frac{d}{c} - 1 \right] f'' \right)^{n-1} f''' + \frac{d^2}{c^2} = 0, \quad (6.9)$$

$$\left[\{1 + R_d(1 + (\theta_w - 1)\theta)^3\} (1 + 2\eta M)\theta' \right]' + \frac{2n}{n+1} \text{Pr} f \theta' = 0, \quad (6.10)$$

along with the associated boundary conditions

$$f(0) = 0, \quad f'(0) = 1, \quad \theta'(0) = -\gamma[1 - \theta(0)], \quad (6.11)$$

$$f'(\eta) = d/c, \quad \theta(\eta) \rightarrow 0 \text{ as } \eta \rightarrow \infty. \quad (6.12)$$

Here $\theta_w \left(= \frac{T_f}{T_\infty} > 1 \right)$ represents the temperature ratio parameter and $R_d \left(= \frac{16\sigma^* T_\infty^3}{kk^*} \right)$ the thermal radiation parameter.

6.1.5 Physical Quantities

The physical quantities of interest which need to be investigated are the local skin friction coefficient C_{fx} (i.e., surface drag) and the local Nusselt number Nu_x (i.e., rate of heat transfer). They may be obtained in the dimensionless form as

$$\frac{1}{2} \text{Re}_b^{\frac{1}{n+1}} C_{fx} = Af''(0) + \left\{ \text{sgn} \left[\frac{d}{c} - 1 \right] f''(0) \right\}^n, \quad (6.13)$$

$$\text{Re}_b^{-\frac{1}{n+1}} Nu_x = - (1 + R_d \theta_w^3) \theta'(0). \quad (6.14)$$

6.2 Solution Methodology

It can be seen that Eqs. (6.9) and (6.10) representing the governing equations of the concerned problem are highly non-linear. Oftenly, exact solutions to such type of equations cannot be obtained. So, to tackle these kind of problems we can utilize some numerical techniques to obtain approximate solutions. Here, we have used the shooting technique to obtain the numerical solutions. For this purpose, firstly the third order equation in $f(\eta)$ and second order equation in $\theta(\eta)$ are converted into set of five initial value problems by introducing the new set of dependent variables y_1, y_2, y_3, y_4 and y_5 as:

$$\begin{aligned} f &= y_1, y_1' = y_2, y_2' = y_3, \\ y_3' &= - \frac{1}{\left[(1 + 2\eta M)A + n(1 + 2\eta M)^{\frac{n+1}{2}} \left(\text{sgn} \left[\frac{d}{c} - 1 \right] y_3 \right)^{n-1} \right]} \left[2MAy_3 + \frac{2n}{n+1} y_1 y_3 \right. \\ &\quad \left. - y_2^2 + \text{sgn} \left[\frac{d}{c} - 1 \right] M(1+n)(1 + 2\eta M)^{\frac{n-1}{2}} \left(\text{sgn} \left[\frac{d}{c} - 1 \right] y_3 \right)^n + d^2/c^2 \right] \end{aligned} \quad (6.15)$$

$$\begin{aligned}\theta &= y_4, y'_4 = y_5, \\ y'_5 &= -\frac{1}{(1+2\eta M)[1+R_d(1+(\theta_w-1)y_4)^3]} \left[MR_d(1+(\theta_w-1)y_4)^3 y_5 + \frac{2n}{n+1} \text{Pr} y_1 y_5 \right. \\ &\quad \left. + 3R_d(1+2\eta M)(\theta_w-1)(1+(\theta_w-1)y_4)^2 (y_5)^2 + 2M y_5 \right],\end{aligned}\quad (6.16)$$

with boundary conditions

$$y_1(0) = 0, y_2(0) = 1, y'_5(0) = -\gamma[1 - y_4(0)], \quad (6.17)$$

which are then solved by using shooting technique.

6.3 The Homotopy Solution and Validity

The local-similar governing ordinary differential equations (6.9) and (6.10) along with associated boundary conditions (6.11) and (6.12) are appeared to be highly non-linear and solutions are obtained numerically. To prove the authenticity of these numerical results obtained by the shooting technique, same problem is solved by the homotopy analysis method (HAM) to obtain analytic series solutions. The convergence of these series solutions is very sensitive to the choice of auxiliary parameter. For this purpose the minimized squared residual error (ch. Chapter 2, Eq. (2.39)) is utilized to obtain the most appropriate value of the auxiliary parameter. Further, it is feasible in some cases to compare the outcomes of the Runge-Kutta shooting technique with those of the HAM solutions. A remarkable agreement between these results presented in figure 6.2 proves the authenticity of the present results and accuracy of the numerical technique.

6.4 Results and Discussion

In this section, numerically calculated results for the velocity and temperature profiles have been displayed graphically for several set of values of the physical parameters like the power-law index n , curvature parameter M , generalized Prandtl number Pr , generalized Biot number γ , temperature ratio parameter θ_w and thermal radiation parameter R_d . The fourth order Runge-Kutta method along with shooting technique is utilized to obtain the numerical solution of the partially coupled set of Eqs. (6.9) and (6.10) along with the boundary conditions (6.11) and (6.12). In all these figures a comparison is made between the flow over a cylinder when $M = 0.5$ and the flow over a flat plate when $M = 0$. Additionally, illustrative outcomes for the skin-friction coefficient and the local Nusselt number outlining the impact of different physical parameters of the flow are recorded through tables.

Figures 6.3 and 6.4 are plotted for shear thinning ($n < 1$) and shear thickening ($n > 1$) fluids. These figures also delineate the influence of the power-law index n on the velocity profile $f'(\eta)$ for the velocity ratio $d/c < 1$ and $d/c > 1$, respectively. From these figures, it is visible that the velocity profile decreases by enlarging the power-law index and thereby reduces the boundary layer thickness for both $n < 1$ (shear thinning fluid) and $n > 1$ (shear thickening fluid). The effect of the power-law index on the temperature profile $\theta(\eta)$ are shown graphically in figures 6.5 and 6.6. These figures highlight the fact that the temperature also diminishes for increasing the power-law index. Qualitatively, same trends are visualized in both the cases i.e., $d/c < 1$ and $d/c > 1$, whereas quantitatively, the boundary layer thickness is larger in case of $d/c < 1$ as compared to $d/c > 1$. Moreover, the boundary layer

thickness is much larger for the shear thinning fluid than that of shear thickening fluid. Additionally, thickness shrinks for the flow over a flat plate ($M = 0$) when compared to the flow over a cylinder ($M = 0.5$).

Figure 6.7 represents the variation of the temperature profile $\theta(\eta)$ in response to change in the values of the generalized Prandtl number Pr for the velocity ratio $d/c < 1$ (which results from the fact that the stretching velocity cx of the plate exceeds the free stream velocity dx). It is worth noting that at a fixed value of η the temperature profile decreases for increasing values of the generalized Prandtl number. This is due to the fact that the fluids with higher Prandtl number have low thermal conductivity which reduces the conduction and hence the thermal boundary layer thickness. Also, it might be seen that the power-law index n assumes a significant part. An increment in value of the power-law index brings about diminishing of the thermal boundary layer. Additionally, a comparison shows that the thermal boundary layer is larger in case of the flow over a cylinder ($M = 0.5$) when compared to the flow over a flat plate ($M = 0$). The influence of the generalized Biot number γ on the temperature profile $\theta(\eta)$ for the flow over cylinder as well as flat plate can be found from figure 6.8. This figure put in confirmation that the effect of increasing the generalized Biot number is to enlarge the temperature profile and hence the thermal boundary layer thickness significantly. This is because of small diffusion resistance relative to the convection resistance.

Figures 6.9 and 6.10 illustrate the nature of the temperature distribution with the temperature ratio parameter θ_w and the radiation parameter R_d , respectively for both the shear thinning and shear thickening fluids. The increasing values of $\theta_w (> 1)$ indicates that the fluid temperature T_f is much higher than the ambient temperature

T_∞ which increases the thermal state of the fluid and results in an increase in the temperature profile. It is noteworthy here that the temperature profile close to the linear radiative heat flux is represented when $\theta_w \approx 1$. Figure 6.9 illustrates the temperature response to the change in the radiation parameter R_d . From this figure, it is noted that an increase in R_d enhances the heat flux from the surface which give rise to the fluid temperature. This also results in an enhancement in the thermal boundary layer thickness. Additionally, a careful observation leads to the fact that the magnitude of temperature is larger in the case of a shear thinning fluid ($n < 1$) as compared to a shear thickening fluid ($n > 1$).

The curvature parameter M significantly affects the temperature profile which is evident from figure 6.11. It is clear from this figure that with increasing values of the curvature parameter the temperature profile decreases in the immediate neighborhood of surface of the cylinder and rises dramatically afterwards. This behavior come into view due to the fact that as a result of decrease in the radius of cylinder, the surface area which is in contact with the fluid also shrinks down. This is because of the fact that the heat transfer by conduction at the surface and convection in the region $\eta > 0$. Thus, less heat energy is transferred by conduction as the surface area of the cylinder reduces which results in a slight fall in the temperature near the surface whereas due to enhanced convection process more heat transfers within the fluid which as a result increases the temperature.

Tables 6.1 and 6.2 are recorded to display the influence of non-dimensional governing parameters on the local friction factor $\frac{1}{2} \text{Re}_b^{\frac{1}{n+1}} C_{fx}$ and local Nusselt number $\text{Re}_b^{-\frac{1}{n+1}} Nu_x$ for fixed values of the Sisko fluid parameter A . It appears from table 6.1 that magnitude of the friction factor rises with curvature parameter for velocity ratio

parameter $d/c < 1$ as well as $d/c > 1$ for shear thinning and shear thickening fluids. Further, a rise in values of the curvature parameter M , generalized Biot number γ , generalized Prandtl number Pr , thermal radiation parameter R_d and temperature ratio parameter θ_w enhances the magnitude of heat transfer rate. Also, a keen observation leads to the fact that more heat transfer takes place in case of shear thickening fluid as compared to shear thinning fluid.

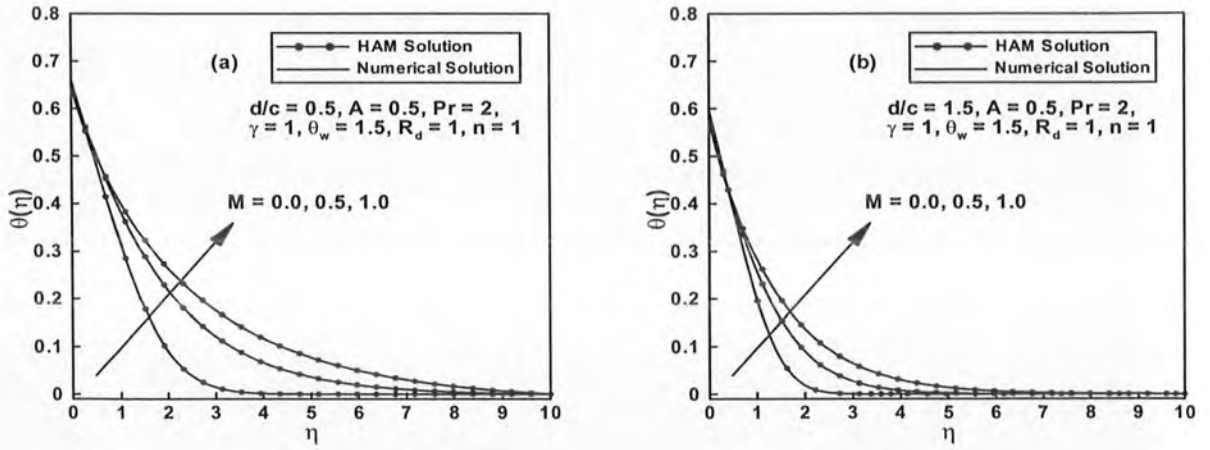


Figure 6.2: A comparison of temperature profiles $\theta(\eta)$ between numerical and HAM solutions for different values of the curvature parameter M when $d/c < 1$ and $d/c > 1$.

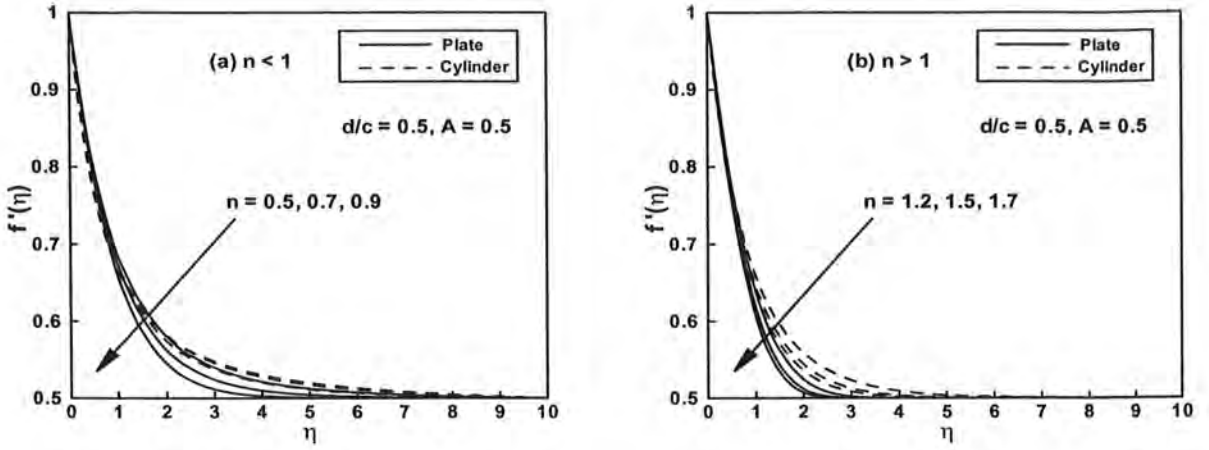


Figure 6.3: The velocity profiles $f'(\eta)$ for different values of the power-law index n when $d/c < 1$.

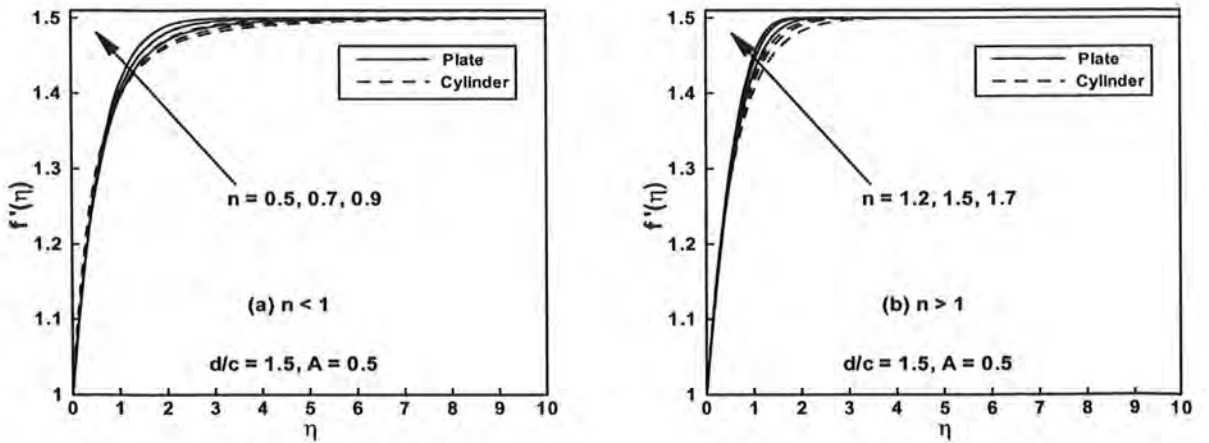


Figure 6.4: The velocity profiles $f'(\eta)$ for different values of the power-law index n when $d/c > 1$.



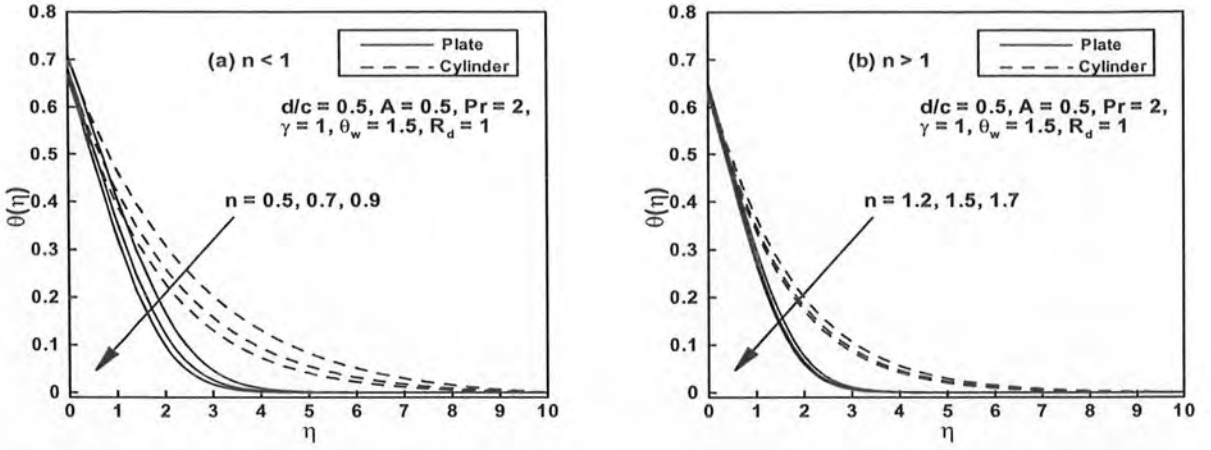


Figure 6.5: The temperature profiles $\theta(\eta)$ for different values of the power-law index n when $d/c < 1$.

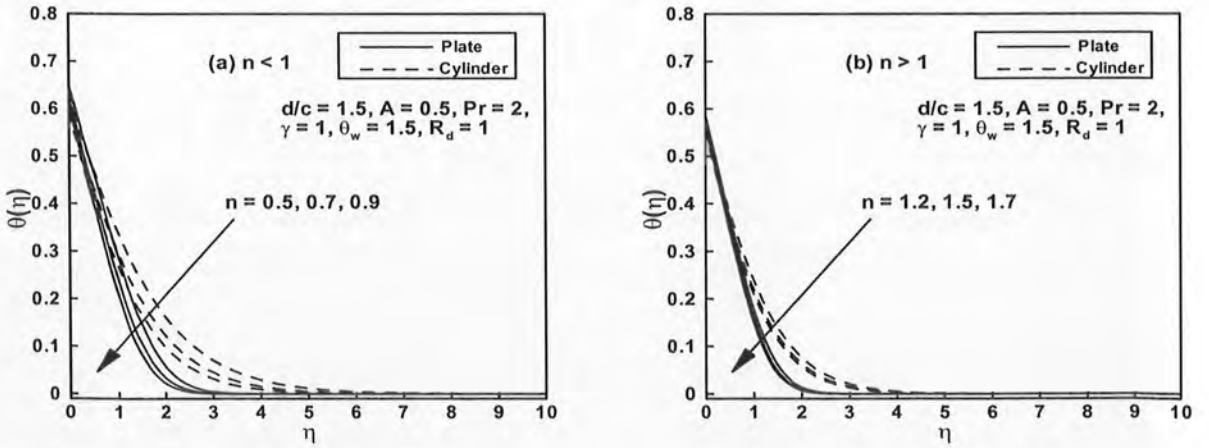


Figure 6.6: The temperature profiles $\theta(\eta)$ for different values of the power-law index n when $d/c > 1$.

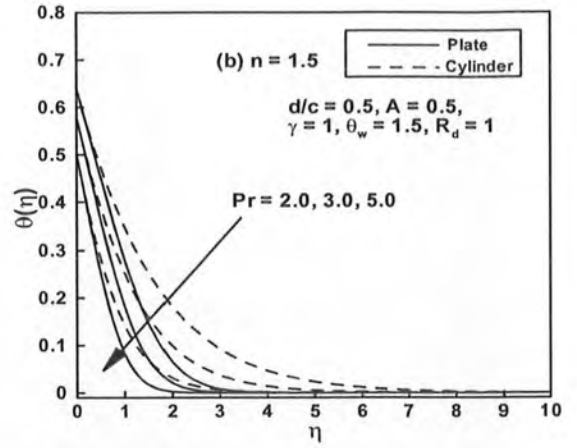
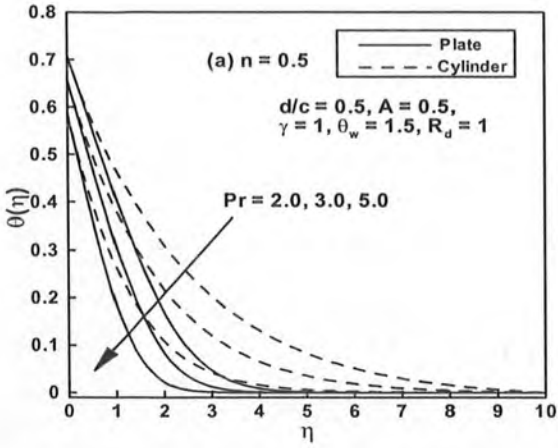


Figure 6.7: The temperature profiles $\theta(\eta)$ for different values of the generalized Prandtl number Pr when $d/c < 1$.

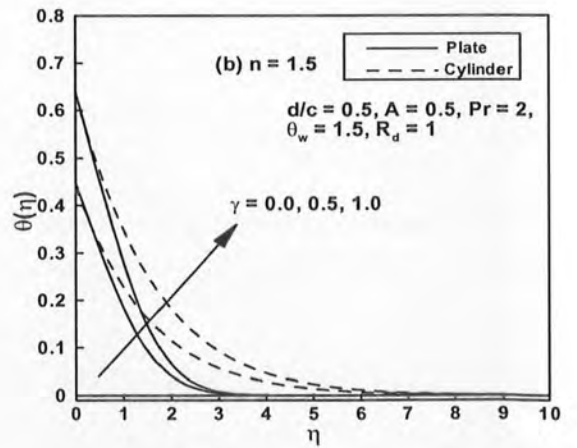
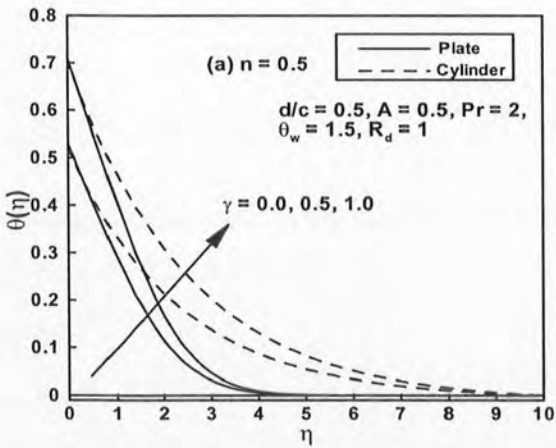


Figure 6.8: The temperature profiles $\theta(\eta)$ for different values of the generalized Biot number γ when $d/c < 1$.

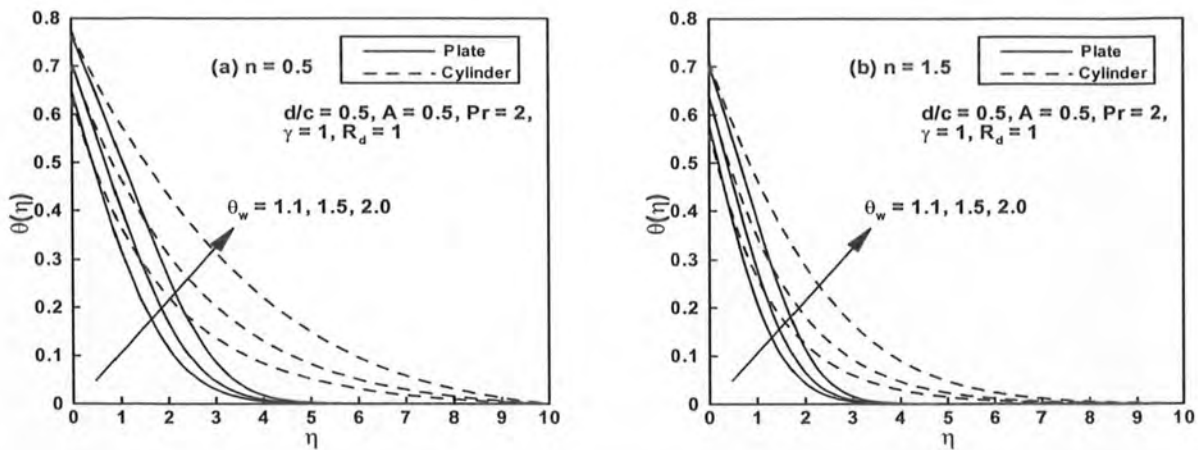


Figure 6.9: The temperature profiles $\theta(\eta)$ for different values of the temperature ratio parameter θ_w when $d/c < 1$.

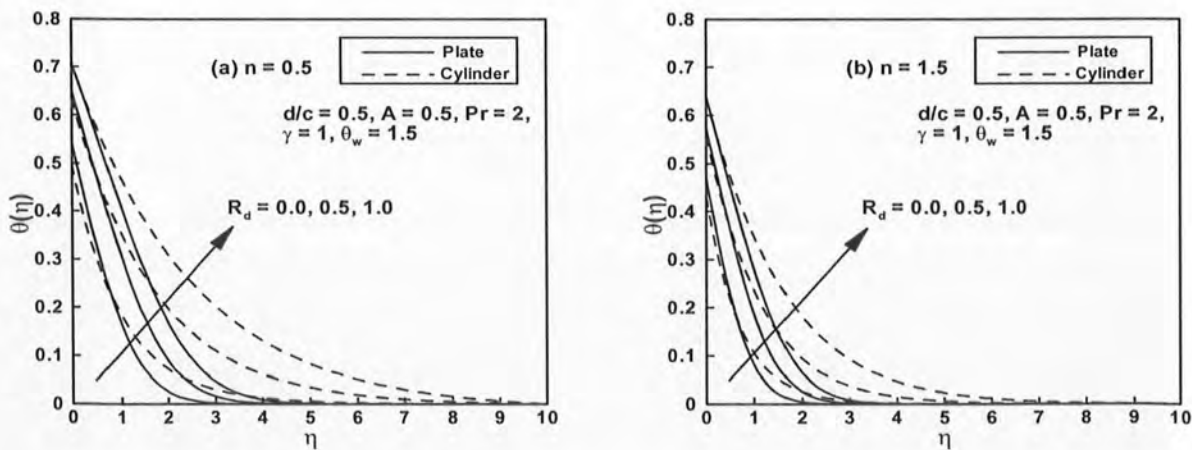


Figure 6.10: The temperature profiles $\theta(\eta)$ for different values of the thermal radiation parameter R_d when $d/c < 1$.

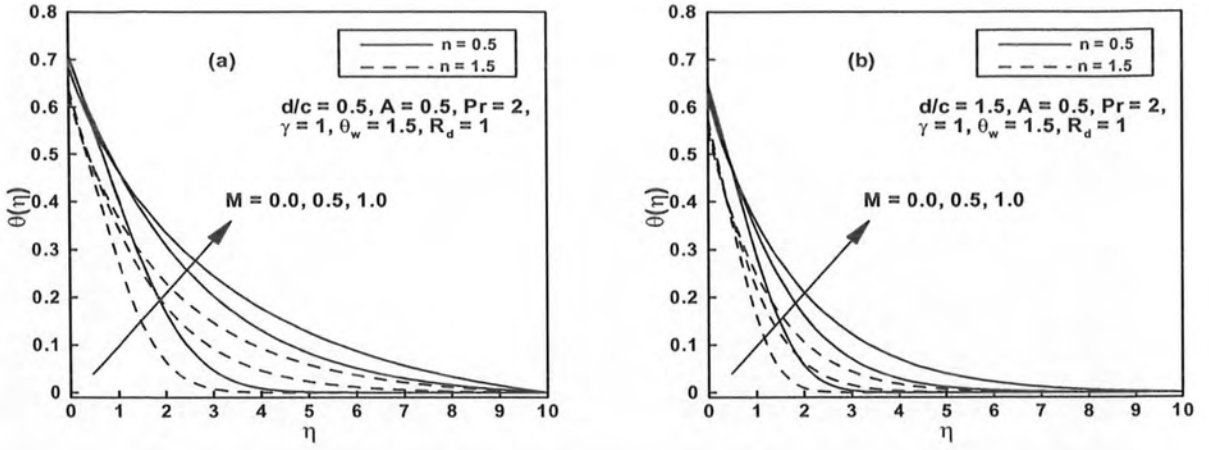


Figure 6.11: The temperature profiles $\theta(\eta)$ for different values of the curvature parameter M when $d/c < 1$ and $d/c > 1$.

Table 6.1: Numerical values of the skin friction coefficient $\frac{1}{2} \text{Re}_b^{\frac{1}{n+1}} C_{fx}$ for different values of physical parameters when $A = 2$ is kept fixed.

d/c	M	$\frac{1}{2} \text{Re}_b^{\frac{1}{n+1}} C_{fx}$	
		$n = 0.5$	$n = 1.5$
0.5	0.0	-0.118643	-0.560765
0.5	0.5	-0.311415	-0.650731
0.5	1.0	-0.498294	-0.723726
1.5	0.0	1.735727	1.501382
1.5	0.5	2.156033	1.814598
1.5	1.0	2.519295	2.099006



Table 6.2: Numerical values of the local Nusselt number $\text{Re}_b^{-\frac{1}{n+1}} Nu_x$ for different values of physical parameters when $A = 0.5$ is kept fixed.

M	γ	Pr	R_d	θ_w	$\text{Re}_b^{-\frac{1}{n+1}} Nu_x$			
					$d/c = 0.5$		$d/c = 1.5$	
					$n = 0.5$	$n = 1.5$	$n = 0.5$	$n = 1.5$
0.0	1.0	2.0	1.0	1.5	1.271146	1.579377	1.537390	1.866250
0.5					1.281567	1.588947	1.595448	1.912811
1.0					1.372046	1.637115	1.659789	1.962965
0.5	0.0	2.0	1.0	1.5	0.000000	0.000000	0.000000	0.000000
	0.5				1.042397	1.220478	1.219366	1.378584
	1.0				1.281567	1.588947	1.595448	1.912811
0.5	1.0	2.0	1.0	1.5	1.281567	1.588947	1.595448	1.912811
		3.0			1.493616	1.845874	1.811187	2.139855
		5.0			1.805237	2.185677	2.096465	2.428697
0.5	1.0	2.0	0.0	1.5	0.502580	0.5677559	0.551235	0.608100
			0.5		0.983804	1.186581	1.166589	1.355853
			1.0		1.281567	1.588947	1.595448	1.912811
0.5	1.0	2.0	1.0	1.1	0.845331	1.005706	0.997784	1.153383
				1.5	1.281567	1.588947	1.595448	1.912811
				2.0	2.026871	2.586664	2.66986	3.326263

Chapter 7

Forced Convective Heat Transfer to Sisko Nanofluid past a Stretching Cylinder in the Presence of Variable Thermal Conductivity

This chapter investigates the influence of variable thermal conductivity on the heat transfer to Sisko nanofluid past a horizontally stretching cylinder affected by the thermophoresis and Brownian motion in the presence of convective boundary and nanoparticles flux conditions. The local-similarity transformation is used to transfer the governing partial differential equations into the ordinary differential equations. Further, these higher order differential equations are converted into seven first order differential equations which are then solved numerically by employing the shooting technique. Graphical and tabular modes of presentation of the computed results illustrated the details of the heat and mass transfer characteristics and their dependence on some physical parameters appearing in the problem. Interestingly, the analysis reveals that the temperature and concentration profiles are larger in case of flow past a cylinder as compared to the flat plate. Also, with the increasing Brownian motion parameter the concentration profile decreases but the temperature profile



remains unaffected. To prove the authenticity of the obtained numerical results a comparison is made with the HAM results.

7.1 Problem Formulation

7.1.1 Governing Equations

Consider a steady and axisymmetric boundary layer flow of an incompressible Sisko nanofluid along a continuously stretching horizontal cylinder of radius d^* with velocity $U = cx$. The cylinder is being stretched and nanofluid is being moved along the axial direction x . The radial coordinate r is measured perpendicular to the cylinder axis. An assumption is made that the cylinder is in contact with a hot fluid at temperature T_f which provides a heat transfer coefficient h_f . The field equations for total mass and momentum are given by Eqs. (2.1) and (2.2), respectively. Whereas, for thermal energy and nanoparticles field equations are given as follows

$$\frac{\partial T}{\partial t} + (\mathbf{V} \cdot \nabla) T = \frac{1}{\rho c_p} [\nabla \cdot (K(T) \nabla T)] + \tau^* \left[D_B (\nabla \cdot C) (\nabla \cdot T) + \frac{D_T}{T_\infty} (\nabla \cdot T) (\nabla \cdot T) \right], \quad (7.1)$$

$$\frac{\partial C}{\partial t} + (\mathbf{V} \cdot \nabla) C = D_B (\nabla^2 C) + \frac{D_T}{T_\infty} (\nabla^2 T), \quad (7.2)$$

where C represents the concentration of the species. We have denoted the ratio of effective heat capacity of the nanoparticle material to the heat capacity of the fluid by τ^* , the Brownian diffusion coefficient by D_B , thermophoresis diffusion coefficient by D_T , and the thermal conductivity of the fluid by $K(T)$.

Here, the concentration of nanoparticles on the boundary is controlled by new condition $D_B \frac{\partial C}{\partial r} + \frac{D_T}{T_\infty} \frac{\partial T}{\partial r} = 0$ which shows zero nanoparticles concentration at the

boundary. At free stream nanoparticle concentration is taken to be constant, i.e., C_∞ . Under these assumptions along with the usual boundary layer approximations, the governing partial differential equations of the problem under consideration are as follows:

$$\frac{\partial(rv)}{\partial r} + \frac{\partial(ru)}{\partial x} = 0, \quad (7.3)$$

$$u \frac{\partial u}{\partial x} + v \frac{\partial u}{\partial r} = \frac{a}{\rho} \frac{\partial^2 u}{\partial r^2} - \frac{b}{\rho r} \left(-\frac{\partial u}{\partial r} \right)^n + \frac{bn}{\rho} \left(-\frac{\partial u}{\partial r} \right)^{n-1} \frac{\partial^2 u}{\partial r^2}, \quad (7.4)$$

$$u \frac{\partial T}{\partial x} + v \frac{\partial T}{\partial r} = \frac{1}{\rho c_p} \frac{1}{r} \frac{\partial}{\partial r} \left[K(T) r \frac{\partial T}{\partial r} \right] + \tau^* \left[D_B \frac{\partial C}{\partial r} \frac{\partial T}{\partial r} + \frac{D_T}{T_\infty} \left(\frac{\partial T}{\partial r} \right)^2 \right], \quad (7.5)$$

$$u \frac{\partial C}{\partial x} + v \frac{\partial C}{\partial r} = D_B \frac{1}{r} \frac{\partial}{\partial r} \left[r \frac{\partial C}{\partial r} \right] + \frac{D_T}{T_\infty} \frac{1}{r} \frac{\partial}{\partial r} \left[r \frac{\partial T}{\partial r} \right]. \quad (7.6)$$

Here the thermal conductivity of the fluid $K(T)$ is assumed to vary linearly with temperature in the form

$$K(T) = k_\infty \left(1 + \varepsilon \left(\frac{T - T_\infty}{\Delta T} \right) \right), \quad (7.7)$$

where k_∞ represents the thermal conductivity of the fluid far away from the cylinder surface, $\Delta T = T_f - T_\infty$ and ε a small parameter known as thermal conductivity parameter.

7.1.2 Boundary Conditions

The associated boundary conditions are given as

$$u = U = cx, \quad v = 0, \quad k \frac{\partial T}{\partial r} = -h_f [T_f - T], \quad D_B \frac{\partial C}{\partial r} + \frac{D_T}{T_\infty} \frac{\partial T}{\partial r} = 0 \quad \text{at } r = d^*, \quad (7.8)$$

$$u \rightarrow 0, T \rightarrow T_\infty, C \rightarrow C_\infty \text{ as } r \rightarrow \infty. \quad (7.9)$$

Here the new condition for concentration field describes zero nanoparticle flux at the boundary. In many physical situations, due to rapid movement of nanoparticles from high to low concentration and from hot to cold surface, it is not so realistic to consider constant nanoparticles concentration at the boundary. Thus, the new condition is more realistic and powerful.

7.1.3 Local-Similarity Transformations

The local-similarity transforms are introduced as follows

$$\eta = \frac{r^2 - d^{*2}}{2d^*x} \text{Re}_b^{\frac{1}{n+1}}, \psi = -Ud^*x \text{Re}_b^{-\frac{1}{n+1}} f(\eta), \theta(\eta) = \frac{T - T_\infty}{T_f - T_\infty}, \phi = \frac{C - C_\infty}{C_\infty}. \quad (7.10)$$

The incompressibility condition (7.3) upon substitution of the local-similarity transformations (7.10) is identically satisfied by the stream function ψ such that $u = \frac{1}{r} \frac{\partial \psi}{\partial r}$, $v = -\frac{1}{r} \frac{\partial \psi}{\partial x}$ and governing equations (7.4) – (7.6) along with the boundary conditions (7.8) and (7.9) take the form

$$(1 + 2\eta M)Af''' + 2MAf'' - M(1 + n) [1 + 2\eta M]^{\frac{n-1}{2}} (-f'')^n + \frac{2n}{n+1} ff'' - (f')^2 + n [1 + 2\eta M]^{\frac{n+1}{2}} (-f'')^{n-1} f''' = 0, \quad (7.11)$$

$$(1 + \varepsilon\theta)(1 + 2\eta M)\theta'' + 2M(1 + \varepsilon\theta)\theta' + \varepsilon(1 + 2\eta M) (\theta')^2 + \frac{2n}{n+1} \text{Pr} f \theta' + N_b(1 + 2\eta M)\theta'\phi' + N_t(1 + 2\eta M)(\theta')^2 = 0, \quad (7.12)$$

$$(1 + 2\eta M)\phi'' + 2M\phi' + \text{Pr} Le \left(\frac{2n}{n+1} \right) f\phi' + \frac{N_t}{N_b}(1 + 2\eta M)\theta'' + 2\frac{N_t}{N_b}M\theta' = 0, \quad (7.13)$$

$$f(0) = 0, \quad f'(0) = 1, \quad \theta'(0) = -\gamma[1 - \theta(0)], \quad N_b\phi'(0) + N_t\theta'(0) = 0, \quad (7.14)$$

$$f'(\eta) \rightarrow 0, \quad \theta(\eta) \rightarrow 0, \quad \phi(\eta) \rightarrow 0 \quad \text{as } \eta \rightarrow \infty, \quad (7.15)$$

where in the above equations, ε denotes the variable thermal conductivity parameter, $N_t \left(= \frac{\tau^* D_T (T_f - T_\infty)}{T_\infty \alpha} \right)$ and $N_b \left(= \frac{\tau^* D_B C_\infty}{\alpha} \right)$ the thermophoresis and Brownian motion parameters, respectively, and $Le \left(= \frac{\alpha}{D_B} \right)$ the Lewis number.

7.1.4 Physical Quantities

From physical point of view, the important characteristics of flow are the skin friction coefficient C_{fx} , the local Nusselt number Nu_x and the local Sherwood number Sh_x which are defined as

$$C_{fx} = \frac{\tau_{rx}|_{r=d^*}}{\frac{1}{2}\rho U^2}, \quad Nu_x = \frac{x q_w|_{r=d^*}}{k_\infty (T_f - T_\infty)}, \quad Sh_x = \frac{x q_m|_{r=d^*}}{D_B C_\infty} \quad (7.16)$$

where τ_{rx} is the shear stress, q_w the wall heat flux and q_m the wall mass flux.

Upon substitution of dimensionless variables (7.10), Eq. (7.16) takes the form

$$\frac{1}{2} \text{Re}_b^{\frac{1}{n+1}} C_{fx} = A f''(0) - [-f''(0)]^n, \quad (7.17)$$

$$\text{Re}_b^{-\frac{1}{n+1}} Nu_x = -\theta'(0), \quad (7.18)$$

$$\text{Re}_b^{-\frac{1}{n+1}} Sh_x = 0. \quad (7.19)$$

Here the Sherwood number becomes identically zero due to the revised boundary

condition (7.8), i.e., nanoparticle concentration flux is zero at the surface.

7.2 Solution Methodology

The locally-similar coupled ordinary differential Eqs. (7.11), (7.12) and (7.13) are of third order in $f(\eta)$ and second order in $\theta(\eta)$ and $\phi(\eta)$ which have been reduced to a system of seven simultaneous equations of first-order as follows:

$$f = y_1, y_1' = y_2, y_2' = y_3, y_3' = -\frac{1}{\left[(1 + 2\eta M)A + n(1 + 2\eta M)^{\frac{n+1}{2}}(-y_3)^{n-1}\right]} \times \left[2MAy_3 - M(1 + n)(1 + 2\eta M)^{\frac{n-1}{2}}(-y_3)^n + \frac{2n}{n+1}y_1y_3 - (y_2)^2\right], \quad (7.20)$$

$$\theta = y_4, y_4' = y_5, y_5' = -\frac{1}{(1 + 2\eta M)(1 + \varepsilon y_4)} \left[\varepsilon(1 + 2\eta M)(y_5)^2 + 2M(1 + \varepsilon y_4)y_5 + N_b(1 + 2\eta M)y_5y_7 + N_t(1 + 2\eta M)(y_5)^2 + \frac{2n}{n+1} \text{Pr } y_1y_5 \right] \quad (7.21)$$

$$\phi = y_6, y_6' = y_7, y_7' = -\frac{1}{(1 + 2\eta M)} \left[\text{Pr } Le \left(\frac{2n}{n+1} \right) y_1y_7 + \frac{N_t}{N_b}(1 + 2\eta M)y_5' + 2My_7 + 2\frac{N_t}{N_b}My_5 \right], \quad (7.22)$$

$$y_1(0) = 0, y_2(0) = 1, y_5(0) = -\gamma[1 - y_4(0)], N_b y_7(0) + N_t y_5(0) = 0. \quad (7.23)$$

In order to solve the above system of equations (7.20) – (7.22) with boundary conditions (7.23) numerically by using the shooting technique seven initial conditions are required but one initial condition each on f , θ and ϕ are missing. However, the values of f , θ and ϕ are known at infinity. Thus, these three end conditions are

utilized to produce three unknown initial conditions at $\eta = 0$. The resulting initial value problem is solved using the fourth order Runge–Kutta method. The Newton–Raphson method is also implemented to correct the guessed values of $f''(0)$, $\theta'(0)$ and $\phi'(0)$.

7.3 Validity of Numerical Results

To prove the authenticity of the numerical results, an analytical approach named the homotopy analysis method is utilized to solve the same problem. Figure 7.8 (b) represents a comparison between the solutions obtained by the homotopy analysis method (HAM) and shooting technique. This figure affirms the agreement between these results and hence proves the authenticity of numerical results obtained by the shooting technique.

7.4 Results and Discussion

The numerical computations are performed for different values of the parameters appearing in the problem namely the power law index n , the curvature parameter M , the generalized Biot number γ , the thermal conductivity parameter ε , the thermophoresis parameter N_t and the Brownian motion parameter N_b . To get a definite perception of the problem, the temperature and concentration profiles are presented graphically for the flow above a flat plate and cylinder, for both the shear thinning ($n < 1$) and shear thickening ($n > 1$) fluids through figures (7.1 – 7.9). Additionally, table presents the influence of the emerging parameters on rate of heat transfer at the surface.

The variation of the temperature $\theta(\eta)$ and concentration $\phi(\eta)$ profiles is presented through figures 7.1 (a, b) and figures 7.2 (a, b) for different values of the power-law index n corresponding to shear thinning ($n < 1$) and shear thickening ($n > 1$) fluids, respectively, for both the flow over a flat plate and cylinder. An observation of these figures makes it clear that the temperature and concentration profiles are decreasing functions of the power-law index n . Further, these effects are more prominent in case of the shear thinning fluid when compared to the shear thickening fluid. Also, from these figures we can observe that the thermal and concentration boundary layer thicknesses are smaller for the flow over a flat plate ($M = 0$) when compared to the flow over a cylinder ($M = 0.5$).

In figures 7.3 (a, b) the variation of the temperature profiles within the boundary layer for various values of the thermal conductivity parameter ε is presented for the shear thinning ($n < 1$) and shear thickening ($n > 1$) fluids, respectively. It is revealed through these figures that as expected, the non-dimensional temperature profile increases with the increase of the thermal conductivity parameter. The value $\varepsilon = 0$ corresponds to the constant conductivity of the fluid. Thus, it is found that the surface temperature is low for constant thermal conductivity when compared to the variable thermal conductivity. It is due to the fact that when ε increases i.e. thermal conductivity of the fluid increases the value of the Prandtl number decreases which as a result increases the temperature of the fluid. Also, these figures reveal that the thermal boundary layer thickness is larger in case of flow over a cylinder ($M = 0.5$) when compared to the flow over a flat plate ($M = 0$).

The influence of the generalized Biot number γ on the temperature distribution is elucidated through figures 7.4 (a, b) for both the cases, i.e., shear thinning ($n < 1$)

and shear thickening ($n > 1$) fluid. The generalized Biot number γ represents the ratio of internal thermal resistance of a solid to boundary layer thermal resistance. When $\gamma = 0$ the surface of cylinder is totally insulated, i.e., internal thermal resistance of the surface of cylinder is extremely high and no convective heat transfer takes place from the surface of cylinder to the cold fluid far away from cylinder. Further, these figures exhibit that the temperature is larger in case of the shear thinning fluid when compared to the shear thickening fluid.

The thermophoresis parameter N_t is an important parameter for investigating the temperature distributions and nanoparticles volume fraction in nanofluid flow. The impact of thermophoresis parameter N_t on the temperature and nanoparticle volume fraction is elucidated through figures 7.5 (a, b) and 7.6 (a, b) for both the shear thinning and shear thickening cases. It turns out from these figures that with the increase of N_t , the temperature as well as nanoparticle volume fraction of the fluid increases. Physically, the thermophoresis force increments with the increase in N_t which tends to move nanoparticles from hot to cold areas and hence increases the magnitude of temperature and nanoparticle volume fraction profiles. Ultimately, the concentration boundary layer thickness turns out to be significantly larger for slightly increased value of thermophoresis parameter. Additionally, these results are more prominent in case of the shear thinning fluid as compared to the shear thickening fluid.

It is noticed that with increasing values of the Brownian motion parameter N_b concentration profile diminishes (figures 7.7 (a, b)) for both the shear thinning and shear thickening fluids. Physically, the higher values of N_b stifle the diffusion of nanoparticles into the fluid regime away from the surface which as a result decreases

the nanoparticle concentration in the boundary layer. Also, the thermal boundary layer remains unaffected by the variation of N_b which is justifiable when we utilize the more realistic boundary conditions proposed by Kuznetsov and Nield [59, 60] given by Eq. (7.8).

In figures 7.8 (a) and 7.9 (a, b) the influence of the curvature parameter M on the temperature and concentration profiles is exhibited for the shear thinning ($n < 1$) and shear thickening ($n > 1$) fluids, respectively. These figures make it clear that the temperature profiles diminish with increasing values of the curvature parameter close to the surface, however, ascent significantly afterwards and the thermal boundary layer thickness increases. This behavior of the temperature profile occurs due to the fact that the surface area in contact with the fluid decreases as the radius of cylinder shrinks down. Here, it is essential to specify that the heat is transferred to the fluid in two modes: conduction at the surface and convection in the fluid for region $\eta > 0$. Thus, as the surface area of cylinder reduces, the temperature profile falls slightly near the surface of the cylinder, in light of the fact that through conduction less heat energy is transferred from the surface to the fluid. On the other hand, in light of the fact that heat transfer in the fluid due to enhanced convection process around the cylinder the thermal boundary layer increases. For the dynamic region (near the surface), the increase of M leads to a decrease in the concentration boundary layers slightly because of the little enhancement of surface mass flux.

The rate of heat transfer at the boundary of the stretching cylinder is presented by table 7.1. Straightforwardly, it appears from table 7.1 that the magnitude of the temperature increases with increasing values of the curvature parameter M , generalized Biot number γ and power-law index n , whereas, it decreases for larger values of

the thermal conductivity parameter ε and thermophoresis parameter. Interestingly, table 7.1 shows that the variation in the values of Brownian motion parameter plays no role in the heat transfer process at the boundary which is justifiable when using conditions (7.8).

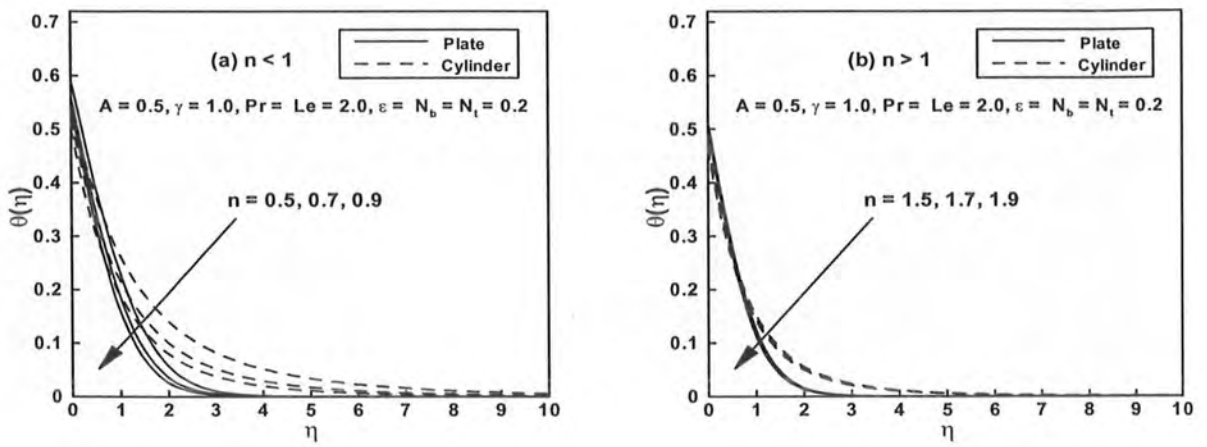


Figure 7.1: The temperature profiles $\theta(\eta)$ for different values of the power-law index

n .

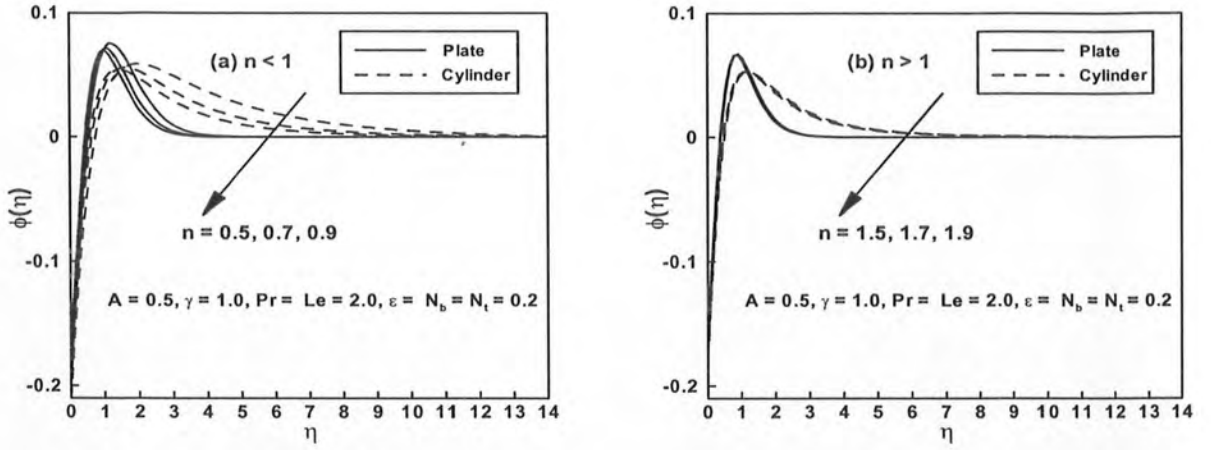


Figure 7.2: The concentration profiles $\phi(\eta)$ for different values of the power-law index n .

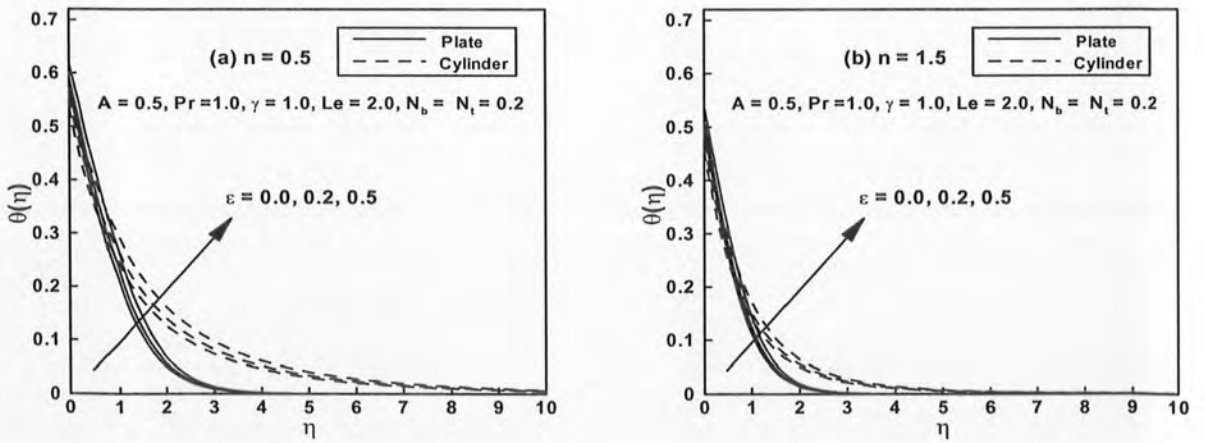


Figure 7.3: The temperature profiles $\theta(\eta)$ for different values of the thermal conductivity parameter ϵ .

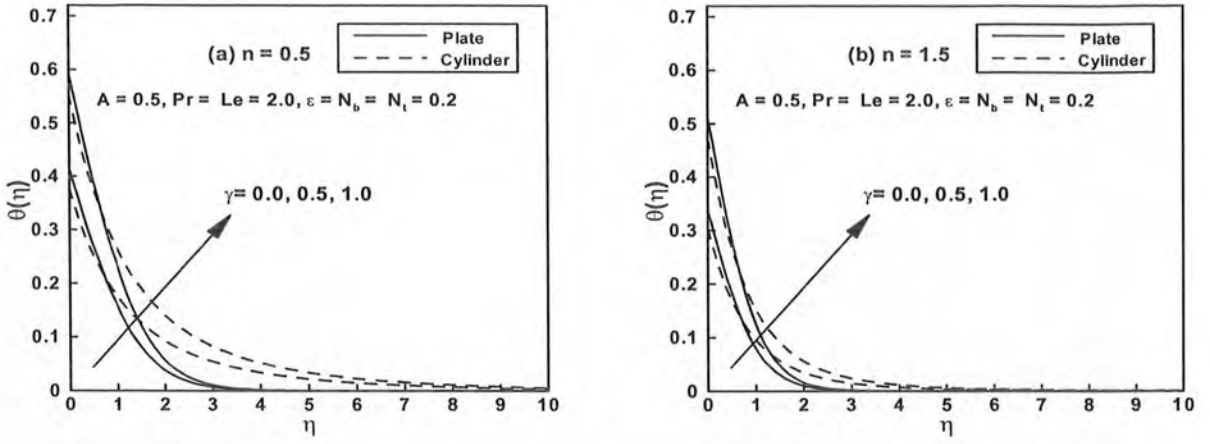


Figure 7.4: The temperature profiles $\theta(\eta)$ for different values of the generalized Biot number γ .

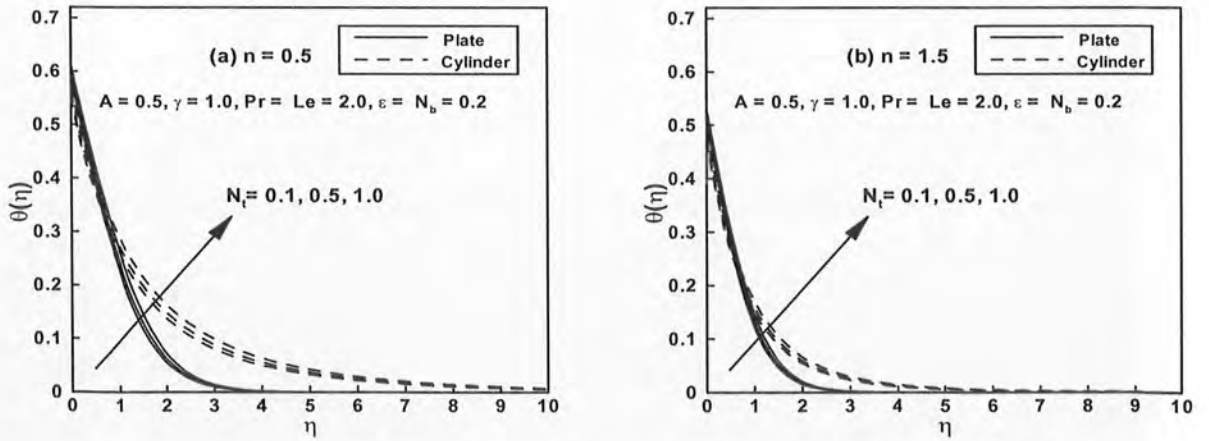


Figure 7.5: The temperature profiles $\theta(\eta)$ for different values of the thermophoresis parameter N_t .

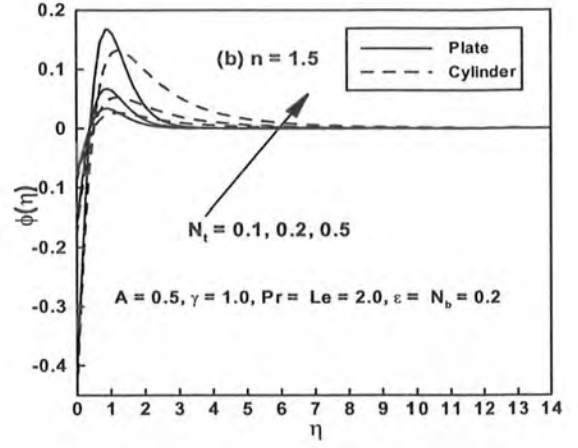
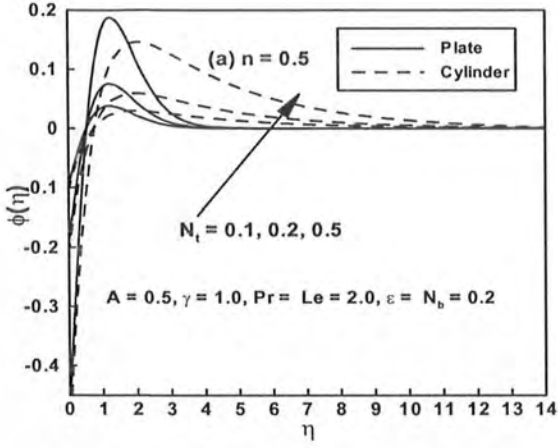


Figure 7.6: The concentration profiles $\phi(\eta)$ for different values of the thermophoresis parameter N_t .

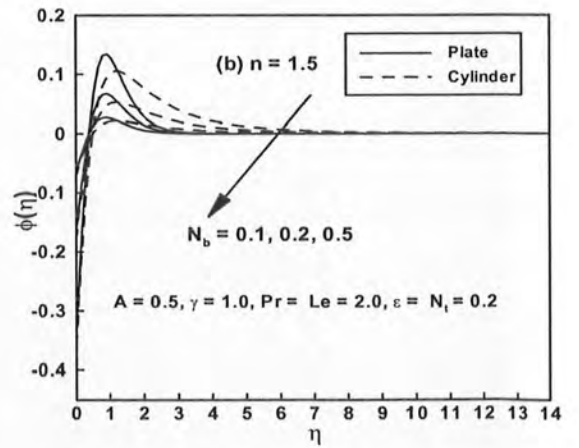
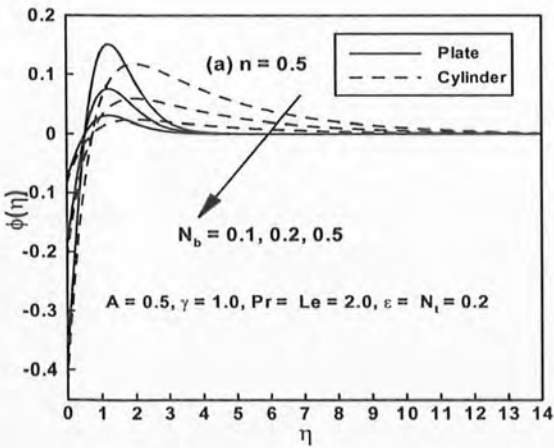


Figure 7.7: The concentration profiles $\phi(\eta)$ for different values of the Brownian motion parameter N_b .

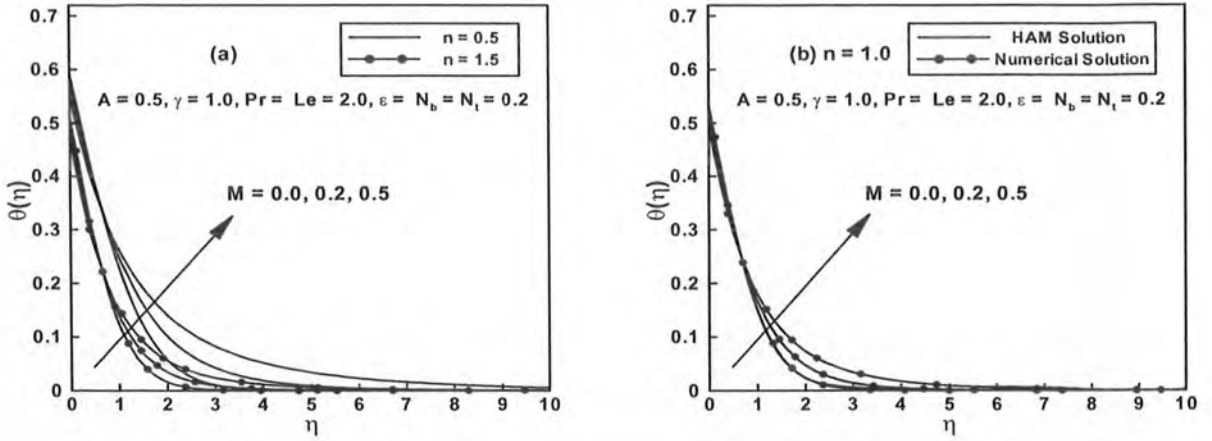


Figure 7.8: The temperature profiles $\theta(\eta)$ for different values of the curvature parameter M .

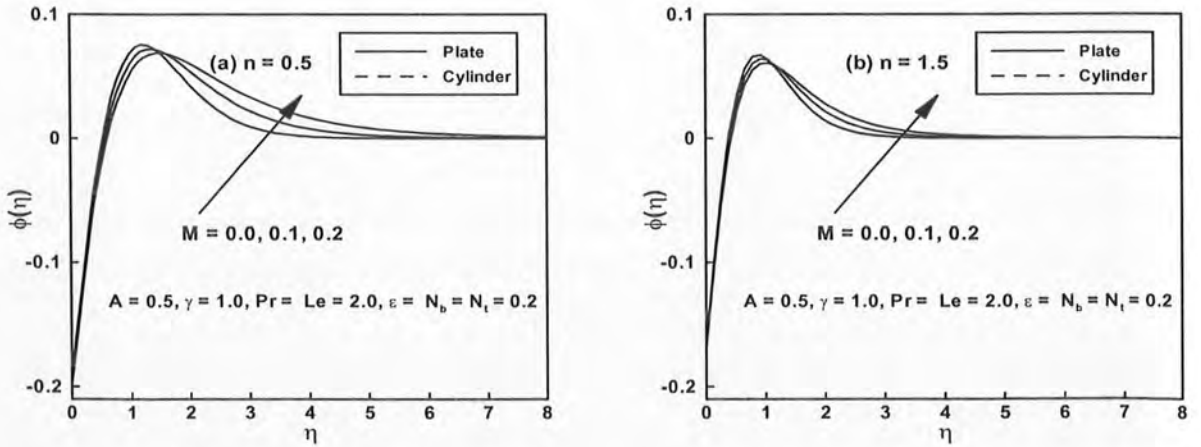


Figure 7.9: The concentration profiles $\phi(\eta)$ for different values of the curvature parameter M .

Table 7.1: Numerical values of the local Nusselt number $\text{Re}_b^{-\frac{1}{n+1}} Nu_x$ for various values of physical parameters $M, \varepsilon, \gamma, \text{Pr}, N_b$ and N_t when $A = 0.5$ and $Le = 2$ are fixed.

M	ε	γ	Pr	N_b	N_t	$-\text{Re}_b^{-\frac{1}{n+1}} Nu_x$	
						$n = 0.5$	$n = 1.5$
0.0	0.2	1.0	2.0	0.2	0.2	0.408470	0.488324
0.5						0.446334	0.527672
1.0						0.484478	0.560735
0.5	0.0	1.0	2.0	0.2	0.2	0.464272	0.543205
	0.2					0.446334	0.527672
	0.5					0.421611	0.505432
0.5	0.2	0.0	2.0	0.2	0.2	0.000000	0.000000
		0.5				0.311804	0.348210
		1.0				0.446334	0.527672
0.5	0.2	1.0	0.7	0.2	0.2	0.334384	0.388298
			1.0			0.365526	0.432345
			2.0			0.446334	0.527672
0.5	0.2	1.0	2.0	0.1	0.2	0.446334	0.527672
				0.2		0.446334	0.527672
				0.5		0.446334	0.527672
0.5	0.2	1.0	2.0	0.2	0.1	0.448391	0.529447
					0.2	0.446334	0.527672
					0.5	0.440027	0.522215

Chapter 8

Homogeneous-Heterogeneous Reactions in Stagnation-Point Flow of Sisko Fluid past a Stretching Cylinder

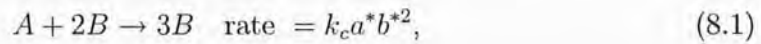
The motivation behind the present chapter is to focus on the effects of stagnation-point flow and heat transfer to the Sisko fluid past an impermeable non-linearly stretching cylinder in the axial direction involving convective boundary conditions with homogeneous-heterogeneous reactions. Diffusion coefficients of species A and B are assumed to be of the same size. Also, it is assumed that heat released during chemical reaction is negligible. A system of governing ordinary differential equations is obtained by using suitable transformations which are then solved numerically by means of the shooting method combined with Runge-Kutta integration technique. The significance of dimensionless parameters involved in the problem has been contemplated for the velocity, temperature and concentration profiles and are discussed at length. The results obtained reveal that the concentration profile decreases with increasing the homogeneous and heterogeneous reaction parameters. Moreover, to prove the authenticity of obtained numerical results a comparison is performed with the analytic results and a good agreement is found between these results.

8.1 Formulation of the Problem

8.1.1 Governing Equations

We consider a steady convective heat transfer near the stagnation-point of a non-Newtonian Sisko fluid by an impermeable horizontal and non-linearly stretching cylinder of radius d^* . The cylindrical coordinates are chosen in a way that x -axis is along the axial direction of cylinder while r -axis is perpendicular to it. By keeping the origin fixed the two equal and opposite forces are applied so that the cylinder surface is stretched in the x -direction with non-linear surface velocity $U_w = cx^s$ and the velocity outside the boundary layer is $U_e = dx^s$, where $d > 0$ is the strength of stagnation flow. Here, a hot fluid with temperature T_f is assumed to be responsible for heating up the surface of the cylinder by which the heat transfer coefficient h_f is provided.

Here, we assume a simple model in a boundary layer flow reported by Chaudhary and Merkin [61, 62] for the interaction between the homogeneous and heterogeneous reactions which involve two chemical species A and B given as follows:



where a^* and b^* represent the concentrations of the chemical species A and B , while k_c and k_s are the rate constants. It is also assumed that a uniform concentration a_0 of reactant A and no autocatalyst B exist far away from the sheet at ambient fluid. Further, it is considered that the heat released by the reaction is negligible. Along

all the above assumptions and in view of the boundary layer approach the governing equations (2.1) – (2.5) in the current problem take the form as follows:

$$\frac{\partial(rv)}{\partial r} + \frac{\partial(ru)}{\partial x} = 0, \quad (8.3)$$

$$\begin{aligned} u \frac{\partial u}{\partial x} + v \frac{\partial u}{\partial r} &= U_e \frac{\partial U_e}{\partial x} + \frac{a}{\rho r} \frac{\partial}{\partial r} \left(r \frac{\partial u}{\partial r} \right) + \operatorname{sgn} \left[\frac{d}{c} - 1 \right] \frac{b}{\rho r} \left\{ \operatorname{sgn} \left[\frac{d}{c} - 1 \right] \frac{\partial u}{\partial y} \right\}^n \\ &+ \frac{bn}{\rho} \left\{ \operatorname{sgn} \left[\frac{d}{c} - 1 \right] \frac{\partial u}{\partial r} \right\}^{n-1} \frac{\partial^2 u}{\partial r^2} + \frac{d^2}{c^2}, \end{aligned} \quad (8.4)$$

$$u \frac{\partial T}{\partial x} + v \frac{\partial T}{\partial r} = \alpha \left(\frac{\partial^2 T}{\partial r^2} + \frac{1}{r} \frac{\partial T}{\partial r} \right), \quad (8.5)$$

$$u \frac{\partial a^*}{\partial x} + v \frac{\partial a^*}{\partial r} = D_A \left(\frac{\partial^2 a^*}{\partial r^2} + \frac{1}{r} \frac{\partial a^*}{\partial r} \right) - k_c a^* b^{*2}, \quad (8.6)$$

$$u \frac{\partial b^*}{\partial x} + v \frac{\partial b^*}{\partial r} = D_B \left(\frac{\partial^2 b^*}{\partial r^2} + \frac{1}{r} \frac{\partial b^*}{\partial r} \right) + k_c a^* b^{*2}, \quad (8.7)$$

where D_A and D_B represent the diffusion species coefficients of A and B .

8.1.2 Boundary Conditions

The subjected boundary conditions for the velocity, temperature and concentrations of the chemical species A and B are given as

$$\begin{aligned} u(r, x) &= U_w = cx^s, \quad v(r, x) = 0, \quad k \frac{\partial T(r, x)}{\partial r} = -h_f [T_f - T(r, x)], \\ D_A \frac{\partial a^*}{\partial r} &= k_s a^*, \quad D_B \frac{\partial b^*}{\partial r} = -k_s a^* \quad \text{at } r = d^*, \end{aligned} \quad (8.8)$$

$$u = U_e = dx^s, \quad T \rightarrow T_\infty, \quad a^* \rightarrow a_0, \quad b^* \rightarrow 0 \quad \text{as } r \rightarrow \infty, \quad (8.9)$$

where c and d are positive real numbers, s , d^* and k represent the stretching parameter, radius of the cylinder and thermal conductivity of the fluid, respectively.

8.1.3 Local-Similarity Transformations

The suitable local transformations are defined as follows:

$$\begin{aligned} \eta &= \frac{r^2 - d^{*2}}{2d^*x} \text{Re}_b^{\frac{1}{n+1}}, & \psi &= -Ud^*x \text{Re}_b^{-\frac{1}{n+1}} f(\eta), \\ \theta(\eta) &= \frac{T - T_\infty}{T_f - T_\infty}, & m(\eta) &= \frac{a^*}{a_0}, & h(\eta) &= \frac{b^*}{a_0}. \end{aligned} \quad (8.10)$$

The incompressibility condition (8.3) is satisfied automatically and Eqs. (8.4) – (8.7) reduced to the following forms

$$\begin{aligned} &(1 + 2\eta M)Af''' + \text{sgn} \left[\frac{d}{c} - 1 \right] M(1 + n)(1 + 2\eta M)^{\frac{n-1}{2}} \left(\text{sgn} \left[\frac{d}{c} - 1 \right] f'' \right)^n \\ &+ \left(\frac{1 + (2n - 1)s}{n + 1} \right) ff'' + n(1 + 2\eta M)^{\frac{n+1}{2}} \left(\text{sgn} \left[\frac{d}{c} - 1 \right] f'' \right)^{n-1} f''' \\ &+ 2MAf'' + s \left(\frac{d^2}{c^2} - (f')^2 \right) = 0, \end{aligned} \quad (8.11)$$

$$[(1 + 2\eta M)\theta'' + 2M\theta'] + \left(\frac{1 + (2n - 1)s}{n + 1} \right) \text{Pr} f \theta' = 0, \quad (8.12)$$

$$\frac{1}{Sc} [(1 + 2\eta M)m'' + 2Mm'] + f m' - Km h^2 = 0, \quad (8.13)$$

$$\frac{\delta}{Sc} [(1 + 2\eta M)h'' + 2Mh'] + f h' + Km h^2 = 0. \quad (8.14)$$

The boundary conditions (7.8) and (7.9) then take the form

$$f(0) = 0, \quad f'(0) = 1, \quad \theta'(0) = -\gamma [1 - \theta(0)], \quad m'(0) = K_s m(0), \quad \delta h'(0) = -K_s m(0), \quad (8.15)$$

$$f'(\eta) = d/c, \theta(\eta) \rightarrow 0, m(\eta) \rightarrow 1, h(\eta) \rightarrow 0 \text{ as } \eta \rightarrow \infty. \quad (8.16)$$

In the above dimensionless expressions Sc , δ , K and K_s denote the generalized Schmidt number, ratio of mass diffusion coefficients, strength of homogeneous reaction parameter and strength of heterogeneous reaction parameter, respectively. These quantities are defined as

$$K = \frac{a_0^2 k_c x}{U_w}, \quad K_s = \frac{k_s dx}{D_A r} \text{Re}_b^{\frac{-1}{n+1}}, \quad Sc = \frac{D_A}{U_w x} \text{Re}_b^{\frac{2}{n+1}}, \quad \delta = \frac{D_B}{D_A}. \quad (8.17)$$

Here an assumption is made that the diffusion coefficients of chemical species A and B are of comparable size. This argument leads us to make further assumption, i.e., the diffusion coefficients D_A and D_B are equal, i.e., $\delta = 1$ and thus

$$m(\eta) + h(\eta) = 1. \quad (8.18)$$

Now in view of Eq. (8.18), Eqs. (8.13) and (8.14) are reduced to

$$\frac{1}{Sc} [(1 + 2\eta M)m'' + 2Mm'] + f m' - Km(1 - m)^2 = 0, \quad (8.19)$$

along with the boundary conditions

$$m'(0) = K_s m(0), m(\eta) \rightarrow 1 \text{ as } \eta \rightarrow \infty. \quad (8.20)$$

8.1.4 Physical Quantities

The physical quantities of interest, i.e., the local skin friction coefficient C_{fx} (surface drag) and the local Nusselt number Nu_x (rate of heat transfer) are defined in dimensionless form as follow:

$$\frac{1}{2} \text{Re}_b^{\frac{1}{n+1}} C_{fx} = Af''(0) + \left\{ \text{sgn} \left[\frac{d}{c} - 1 \right] f''(0) \right\}^n, \quad (8.21)$$

$$\text{Re}_b^{-\frac{1}{n+1}} Nu_x = -\theta'(0). \quad (8.22)$$

8.2 Solution Methodologies

8.2.1 The Numerical Solution

The system of highly non-linear governing ordinary differential Eqs. (8.11), (8.12) and (8.13) along with boundary conditions (8.15), (8.16) and (8.20) have been solved numerically by using the Runge-Kutta method in combination with the shooting technique. In this technique, a set of coupled Eqs. (8.11), (8.12) and (8.13) are reduced to a system of first order differential equations and converted into set of initial value problem as:

$$\begin{aligned} f &= y_1, y'_1 = y_2, y'_2 = y_3, \\ y'_3 &= \frac{-1}{\left[(1 + 2\eta M)A + n(1 + 2\eta M)^{\frac{n+1}{2}} \left(\text{sgn} \left[\frac{d}{c} - 1 \right] y_3 \right)^{n-1} \right]} \left[\left(\frac{1 + (2n-1)s}{n+1} \right) y_1 y_3 \right. \\ &\quad \left. + \text{sgn} \left[\frac{d}{c} - 1 \right] M(1+n)(1 + 2\eta M)^{\frac{n-1}{2}} \left(\text{sgn} \left[\frac{d}{c} - 1 \right] y_3 \right)^n \right. \\ &\quad \left. + 2MAy_3 + s \left(\frac{d^2}{c^2} - (y_2)^2 \right) \right], \end{aligned} \quad (8.23)$$

$$\begin{aligned}\theta &= y_4, y_4' = y_5, \\ y_5' &= \frac{-1}{(1+2\eta M)} \left[2My_5 + \left(\frac{1+(2n-1)s}{n+1} \right) \text{Pr } y_1 y_5 \right],\end{aligned}\quad (8.24)$$

$$\begin{aligned}m &= y_6, y_6' = y_7, \\ y_7' &= \frac{-1}{(1+2\eta M)} \left[2My_7 + Sc \{ y_1 y_7 - Ky_6 (1-y_6)^2 \} \right],\end{aligned}\quad (8.25)$$

with

$$\begin{aligned}y_1(0) &= 0, \quad y_2(0) = 1, \quad y_3(0) = s_1, \quad y_4(0) = \frac{y_5(0)}{\gamma} + 1, \\ y_5(0) &= s_2, \quad y_6(0) = \frac{y_7(0)}{K_s}, \quad y_7(0) = s_3.\end{aligned}\quad (8.26)$$

The above initial value problems are then solved by setting some initial guesses for three unknown initial conditions $y_3(0) = s_1$, $y_5(0) = s_2$ and $y_7(0) = s_3$. We have chosen appropriate value of domain length $\eta \rightarrow \infty$ namely $\eta = \eta_\infty = 10$ for the present problem.

8.2.2 Validity of Solutions

The analytic series solutions are obtained for the governing equations (8.11), (8.12) and (8.13) along with boundary conditions (8.15), (8.16) and (8.20) by employing the homotopy analysis method (HAM). This method works remarkably for the non-linear equations and also provides freedom to choose initial guesses and linear operators. The results obtained by this method are in the form of series whose convergence can be questioned. For the convergence of these results the auxiliary parameter \hbar plays

a very important role. The auxiliary parameter can have value between $-2 < \hbar < 0$ and in the present analysis the most suitable value from this range is obtained by minimizing the squared residual error (ch. Chapter 2, Eq. (2.39)). Further, the accuracy of our numerical results is affirmed by comparing them with results obtained by the HAM results for particular cases (see figure 8.8(b)). A comparison given in this figure shows an excellent agreement between these results and gives us confidence in our numerical computations.

8.3 Results and Discussion

In this study, numerical calculations are accomplished for the analysis of homogeneous-heterogeneous reactions on the stagnation-point flow of Sisko fluid over a non-linearly stretching cylinder in the presence of convective boundary conditions. The Runge-Kutta method in combination with shooting technique is employed to solve governing Eqs. (8.11), (8.12) and (8.19) along with boundary conditions (8.15), (8.16) and (8.20). A detailed discussion is provided in this section about the physical significance of dimensionless parameters on the velocity, temperature and concentration profiles. Figures 8.1 – 8.8 are plotted for the shear thinning ($n = 0.2$) and shear thickening ($n = 1.5$) fluids and these figures reveal that the boundary layer thickness is larger for the shear thinning fluid as compared to the shear thickening fluid. For numerical calculations, we considered $\gamma = 1$, $Pr = 2$, $s = 0.5$, $A = 1$, $M = 0.5$, $d/c = 0.5$, $K_s = 0.2$, $K = 1$ and $Sc = 1.5$. In this entire study we considered these values as common except the variations in the corresponding graphs and tables.

Figures 8.1 and 8.2 illustrate the nature of the velocity, temperature and concen-

tration distributions with the curvature parameter M . These figures reveal that the velocity and temperature profiles decrease near the surface of the cylinder while these increase gradually away from the surface with increasing values of the curvature parameter and an opposite behavior can be seen in the concentration profile. Actually, for higher values of the curvature parameter, the radius of cylinder decreases which reduces area of contact of the cylinder with fluid. Therefore the velocity and temperature profiles increase. It is noteworthy here that for $M = 0$ the problem reduces to the flow over a flat plate for which the momentum and thermal boundary layers are smaller when compared to the case of flow over a stretching cylinder ($M \neq 0$) whereas, the concentration boundary layer is larger for the case of flow over a flat plate.

The stretching parameter s significantly affects the velocity, temperature and concentration profiles which is clear from figures 8.3 and 8.4. It appears from these figures that the velocity and temperature profiles decrease while the concentration profile increases with enlarging values of the stretching parameter. Figure 8.5 represents the temperature response to the change in the generalized Biot number γ for small and large values of the generalized Prandtl number Pr (i.e., $Pr = 2, 20$). For decreasing diffusion resistance compared to the convection resistance i.e., for increasing values of γ the temperature profile increases which is evident from this figure. Moreover, this figure shows that the thermal boundary layer is larger for smaller value of Pr ($= 2$) relative to larger value of Pr ($= 20$).

The influence of the homogeneous reaction parameter K on the concentration profile is illustrated through figure 8.6. Since during the homogeneous reactions reactants are consumed so as a result the concentration depreciates which is evident

from this figure. Further, the influence of strength of heterogeneous reaction parameter K_s on the concentration profile is quite similar to that of the homogeneous reaction parameter which is shown through figure 8.7. The concentration boundary layer thickness increases with enlarging K_s which agrees with the general physical behavior of the homogeneous and heterogeneous reaction parameters.

In figure 8.8(a) the concentration profile against various values of the generalized Schmidt number Sc is displayed. For enlarge values of Sc the concentration profile is noted to be increasing. In fact the Schmidt number is the ratio of momentum diffusivity to mass diffusivity. Therefore, higher values of the Schmidt number correspond to small mass diffusivity. In order to prove the accuracy of the obtained numerical results a comparison between the numerical results and the analytical results computed by means of the homotopy analysis method is performed through figure 8.8(b). This comparison leads to an excellent agreement of the analytical solutions with the numerical results.

Tables 8.1 and 8.2 illustrate the influence of various dimensionless parameters on the local skin friction coefficient and local Nusselt number. It appears from these tables that the magnitude of the local skin friction coefficient diminishes with A and M for the shear thinning fluid while it increases for shear thickening fluid. Further, magnitude of the rate of heat transfer increases with A , M , Pr and γ for both the shear thinning and shear thickening fluids.



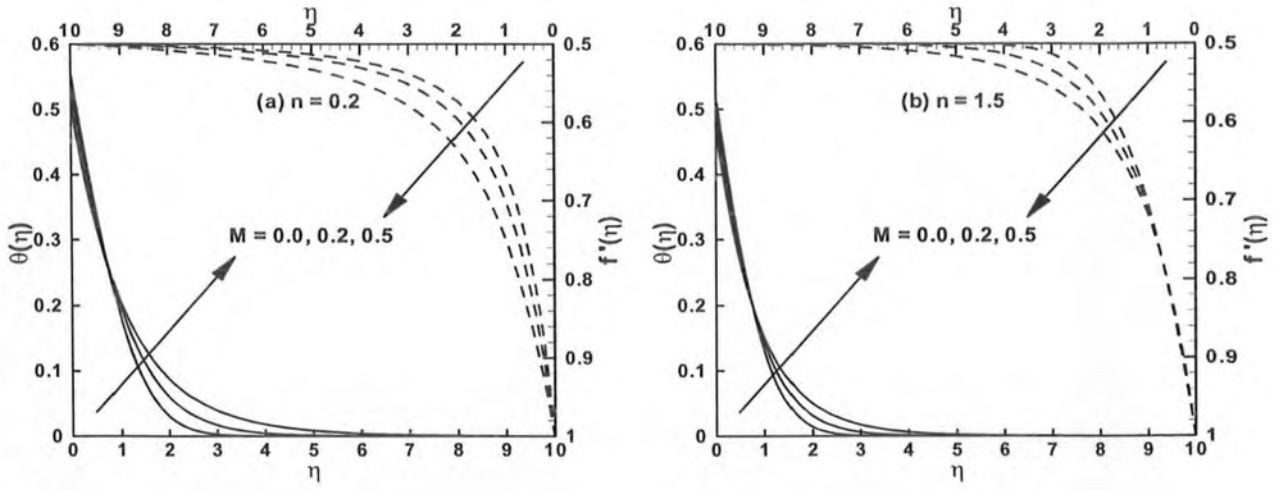


Figure 8.1: Variation of $f'(\eta)$ and $\theta(\eta)$ for different values of the curvature parameter M .

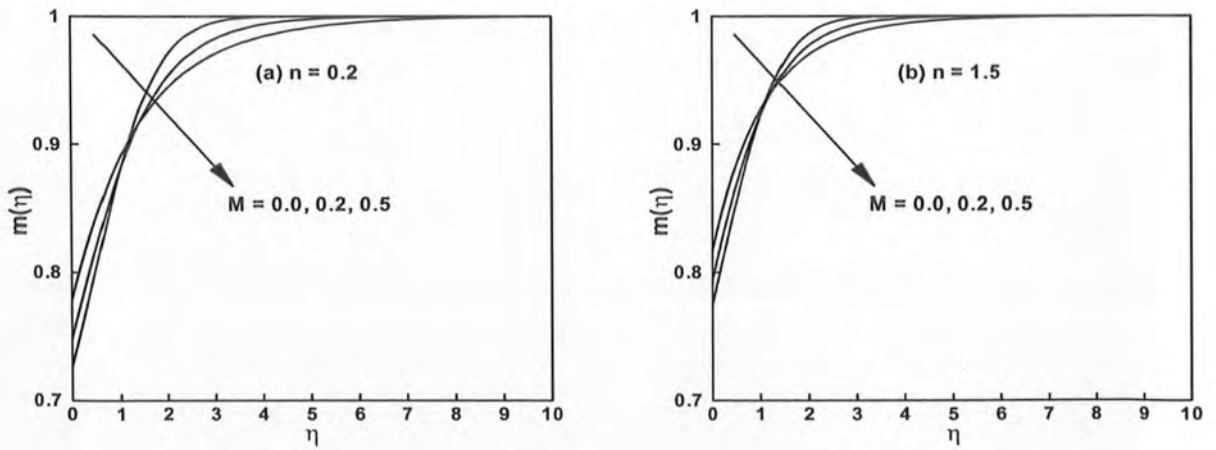


Figure 8.2: Variation of $m(\eta)$ for different values of the curvature parameter M .

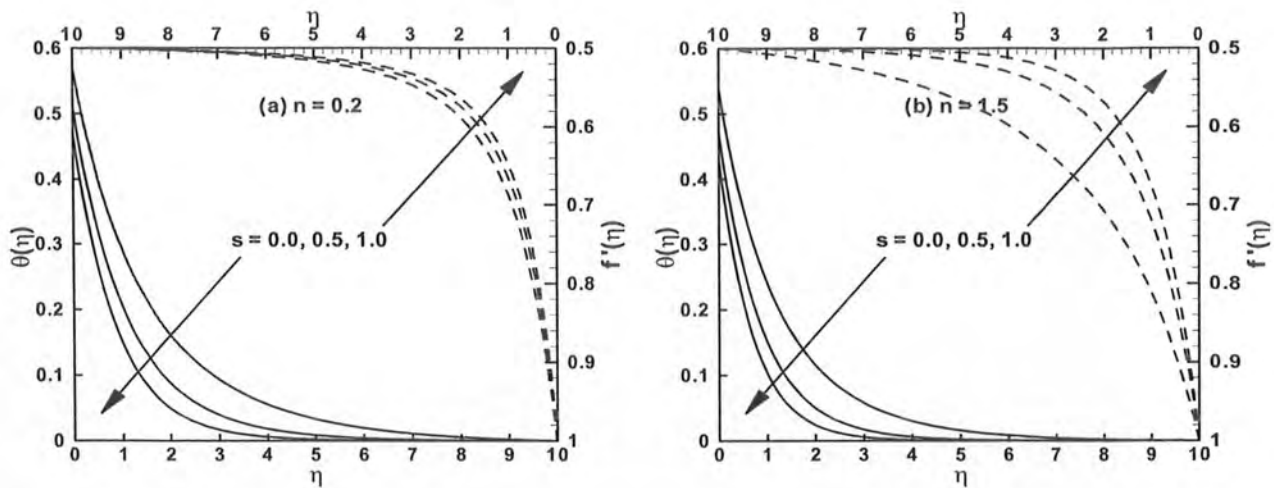


Figure 8.3: Variation of $f'(\eta)$ and $\theta(\eta)$ for different values of the stretching parameter

s.

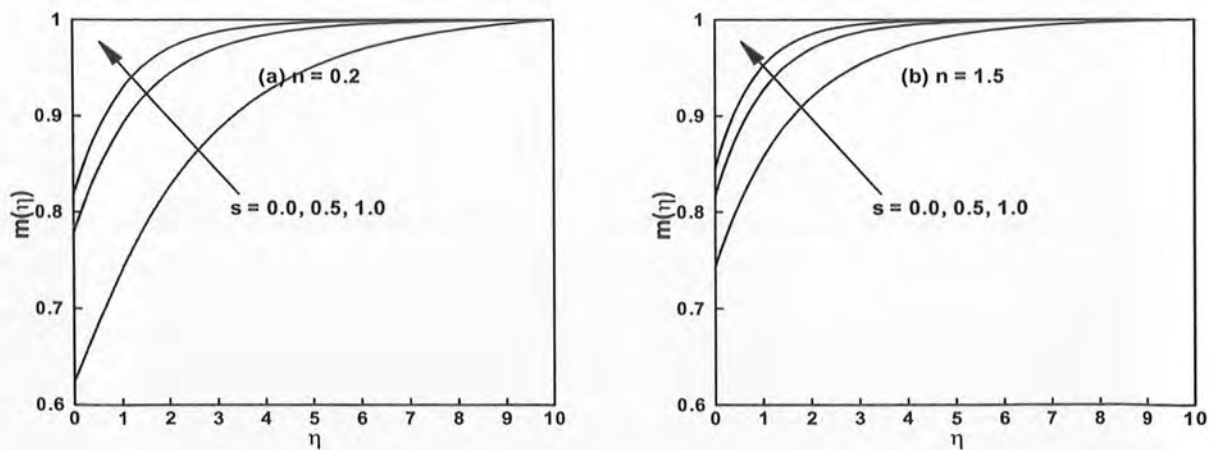


Figure 8.4: Variation of $m(\eta)$ for different values of the stretching parameter s .

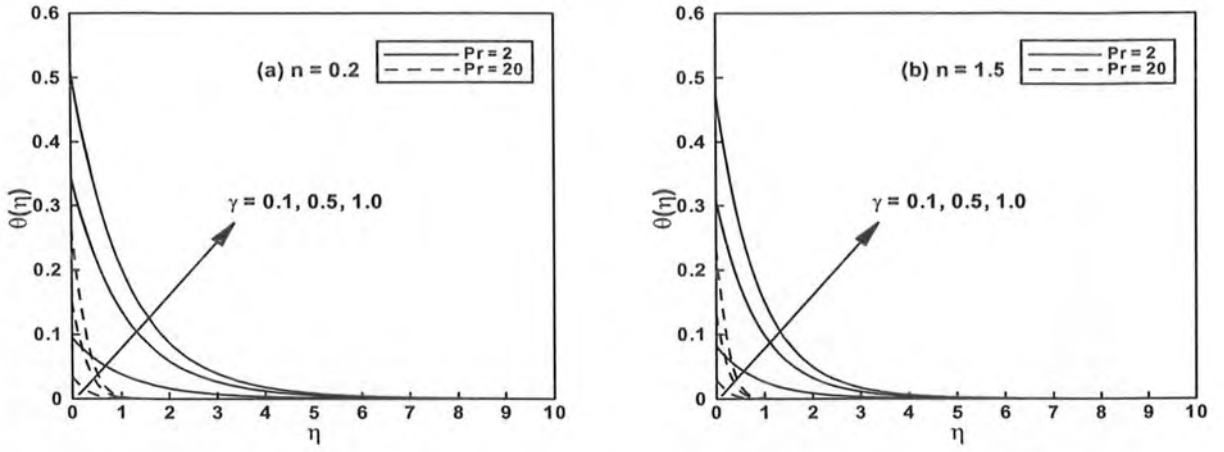


Figure 8.5: Variation of $\theta(\eta)$ for different values of the generalized Biot number γ .

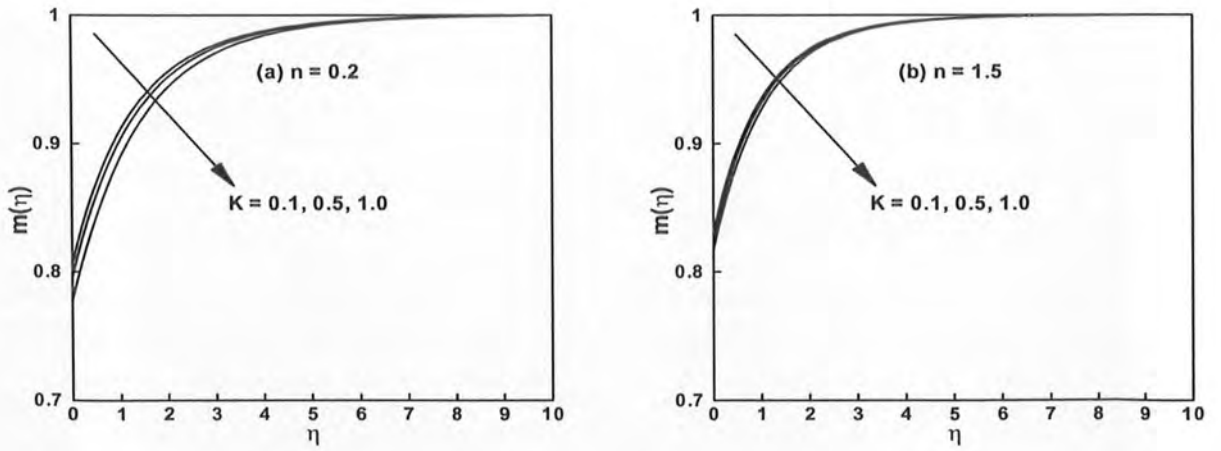


Figure 8.6: Variation of $m(\eta)$ for different values of the homogeneous reaction parameter K .

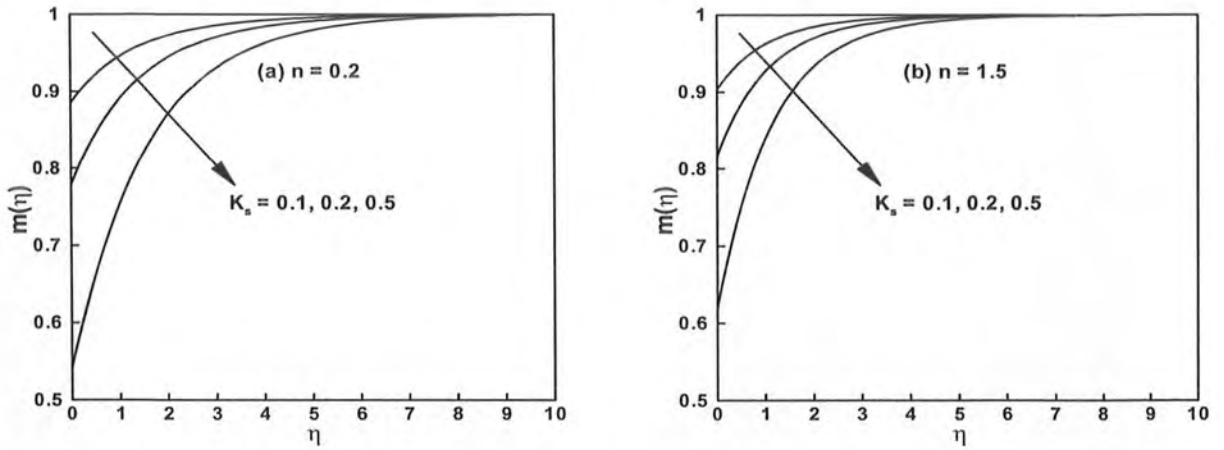


Figure 8.7: Variation of $m(\eta)$ for different values of the heterogeneous reaction parameter K_s .

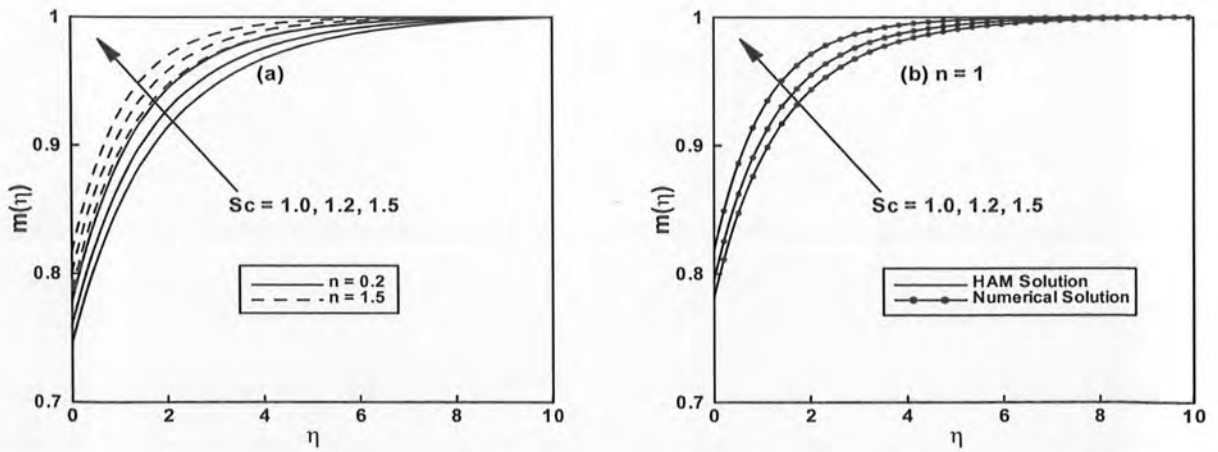


Figure 8.8: Variation of $m(\eta)$ for different values of the generalized Schmidt number Sc .

Table 8.1: Numerical values of the local skin friction coefficient $\frac{1}{2} \text{Re}_b^{\frac{1}{n+1}} C_{fx}$ for different values of A and M when $s = 0.5$ and $d/c = 0.5$ are kept fixed.

A	M	$\frac{1}{2} \text{Re}_b^{\frac{1}{n+1}} C_{fx}$	
		$n = 0.2$	$n = 1.5$
0.5	0.5	0.5417954	0.1191422
1.0		0.2470970	-0.1477414
1.5		0.0179531	-0.3644116
1.0	0.0	0.4574655	-0.1463242
	0.2	0.3719450	-0.1478883
	0.5	0.2470970	-0.1477414

Table 8.2: Numerical values of the local Nusselt number $\text{Re}_b^{-\frac{1}{n+1}} Nu_x$ for different values of M , A , Pr and γ when $s = 0.5$ and $d/c = 0.5$ are kept fixed.

M	γ	Pr	A	$\text{Re}_b^{-\frac{1}{n+1}} Nu_x$	
				$n = 0.2$	$n = 1.5$
0.0	1.0	2.0	0.5	0.4439990	0.4825066
0.2				0.4618786	0.5021327
0.5				0.4880411	0.5282420
0.5	0.1	2.0	0.5	0.0905059	0.0918015
	0.5			0.3279756	0.3456534
	1.0			0.4880411	0.5282420
0.5	1.0	2.0	0.5	0.4880411	0.5282420
		3.0		0.5330922	0.5737181
		5.0		0.5908293	0.6303546
0.5	1.0	2.0	0.5	0.4840073	0.5258823
			1.0	0.4880411	0.5282420
			1.5	0.4906021	0.5298594

Chapter 9

Conclusions and Future Work

9.1 Conclusions

The purpose of the present thesis was to investigate theoretically the characteristics of convective heat transfer to the Sisko fluid flowing over moving surfaces in the presence of convective boundary conditions. Here, mainly two type of moving surfaces were considered i.e., the planer/radially stretching flat plate and the stretching cylinder in its axial direction. Further, the local-similar transformed governing equations were solved numerically by using the shooting technique along with the Runge-Kutta method and analytically by the homotopy analysis method. In the case of flow over a flat plate, the exact analytic solutions were also calculated for some special cases. The flow and thermal characteristics were scrutinized over a range of values of the non-dimensional parameters such as the power-law index (integer and non-integer), generalized Prandtl number, generalized Biot number, curvature parameter, mixed convection buoyancy parameter, Eckert number, thermal radiation parameter, temperature ratio parameter, thermal conductivity parameter, the thermophoresis and Brownian motion parameters, the strength of homogeneous and heterogeneous reaction parameters etc. In general, it was observed that the boundary layer thickness

was larger when considering the shear thinning fluid as compared to the shear thickening fluid. Also, for the flow over a stretching flat plate the thermal boundary layer thickness was smaller as compared to the flow over a stretching cylinder. The main findings of the thesis could be summarized as follows:

- In general, impact of the power-law index on the temperature was to diminish it as well as the thermal boundary layer thickness. The effects seemed more significant for the shear thinning fluid as compared to the shear thickening fluid which was marginally influenced. The magnitude of the local skin friction was smaller in case of the shear thickening fluid as compared to the shear thinning fluid whereas more heat transferred for the shear thickening fluid than the shear thinning fluid.
- The generalized Prandtl number highly influenced the temperature profile. With the increasing values of the generalized Prandtl number the temperature profile was decreased and thereby reduced the thermal boundary layer thickness. Further, It was observed that more heat transferred for the larger generalized Prandtl number.
- Due to the hot fluid's reduced convection resistance with the larger values of the generalized Biot number, temperature profile was increased and a rise in the thermal boundary layer was observed. Also, magnitude of rate of heat transfer was increased with the generalized Biot number.
- The mixed convection buoyancy parameter significantly affected the velocity and temperature profiles. For the assisting flow the velocity profile was increasing whereas the temperature profile was decreasing and an opposite behavior

appeared for the opposing flow. Additionally, magnitude of the local skin friction and local Nusselt number had opposite behaviors.

- Inside the thermal boundary layer, the temperature profile was increasing with the stronger thermal radiation and hence a rise in the thermal boundary layer thickness was witnessed whereas, magnitude of both the local skin friction and the local Nusselt number was decreasing.
- The temperature profile showed two different behaviors for the increasing values of the curvature parameter i.e., decreasing near the surface and increasing dramatically far away from the surface which resulted from reduced conduction and increased convection in the fluid, respectively. Also, the boundary layer thickness was larger in the case of flow over a cylinder when compared to the flow over a flat plate. Also, the magnitude of local skin friction and the rate of heat transfer is larger when we considered the stretching cylinder as compared to the stretching flat plate.
- The Eckert number which representing a relation between enthalpy and kinetic energy in a flow was responsible for rising the temperature with its increasing values. When comparing the influence of Eckert number on a stretching plate and stretching cylinder it was abundantly clear that more significant results were achieved for the stretching cylinder rather than stretching plate. Further, more heat was transferred with the increasing values of the Eckert number.
- The temperature ratio parameter which was assumed to be greater than one represented that fluid temperature was dominant over the ambient temperature. The increasing values of temperature ratio parameter indicated a rise in



the temperature and the rate of heat transfer.

- The thermal conductivity parameter represents the constant conductivity of the fluid for zero value and variable conductivity for the positive values. An increase in the thermal conductivity parameter corresponded an increase in the temperature profile. Also, temperature profile was larger in case of variable thermal conductivity as compared to the constant thermal conductivity of the fluid, however, rate of heat transfer appeared as diminishing with the thermal conductivity parameter.
- The Brownian motion parameter did not effect the temperature and rate of heat transfer due to utilization of new mass flux conditions. Whereas, in the boundary layer the concentration profile decreased with a rise in the Brownian motion parameter.
- The temperature and nanoparticle volume fraction profiles tended to increase with the increasing values of the thermophoresis parameter which resulted from an increase in the thermophoresis force and moved the particles from hot to cold regions.
- For the homogeneous and heterogeneous reactions parameters the concentration boundary layer thickness was increased.
- Ultimately, to verify the obtained results a comparison between analytical and numerical results was provided in graphical and/or tabular form which confirmed the validity of our results.

9.2 Future Work

In the present thesis we have studied the steady convective heat transfer to the boundary layer flows of Sisko fluid in the presence of the convective boundary conditions. It will be valuable to study the boundary layer flow of the Sisko fluid over a planner as well as curved stretching surfaces in the presence of melting heat transfer effects. Also, the study of unsteady boundary layer flow of the Sisko fluid over rotating surfaces/geometries which have direct relevance to the industrial applications will be the focus of our research in the next step. Also, we considered only impermeable stretching flat plate and cylinder in the previous investigations and in the future, we can consider different permeable geometries.

Bibliography

- [1] Sisko, A.W., The flow of lubricating greases, *Ind. Eng. Chem. Res.*, **50** (12) (1958) 1789-1792.
- [2] Hassanien, I.A., Abdullah, A.A. and Gorla, R.S.R., Flow and heat transfer in a power-law fluid over a nonisothermal stretching sheet, *Math. Comput. Model.*, **28** (9) (1998) 105-116.
- [3] Chen, C., Heat transfer in a power-law fluid film over a unsteady stretching sheet, *Heat Mass Transf.*, **39** (2003) 791-796.
- [4] Prasad, K.V., Santhi, S.R. and Datti, P.S., Non-Newtonian power-law fluid flow and heat transfer over a non-linearly stretching surface, *Appl. Math.*, **3** (2012) 425-435.
- [5] Lin, Y., Zheng, L., Li, B. and Zhang, X., MHD thin film and heat transfer of power law fluids over an unsteady stretching sheet with variable thermal conductivity, *Therm. Sci.*, **00** (2014) 34-34.
- [6] Shahzad, S.A., Alsaedi, A. and Hayat, T., Three-dimensional flow of Jeffrey fluid with convective surface boundary conditions, *Int. J. Heat Mass Transf.*, **55** (15-16) (2012) 3971-3976.

- [7] Hayat, T., Iqbal, Z., Mustafa, M. and Alsaedi, A., Momentum and heat transfer of an upper-convected Maxwell fluid over a moving surface with convective boundary conditions, *Nucl. Eng. Des.*, **252** (2012) 242-247.
- [8] Hayat, T., Iqbal, Z., Qasim, M. and Obaidat, S., Steady flow of an Eyring Powell fluid over a moving surface with convective boundary conditions, *Int. J. Heat Mass Transf.*, **55** (2012) 1817-1822.
- [9] Srinivasacharya, D. and Bindu, K.H., Entropy generation in a micropolar fluid flow through an inclined channel with slip and convective boundary conditions, *Energy*, **91** (2015) 72-83.
- [10] Rundora, L. and Makinde, O.D., Effects of Navier slip on unsteady flow of a reactive variable viscosity non-Newtonian fluid through a porous saturated medium with asymmetric convective boundary conditions, *J. Hydrodyn.*, **27** (6) (2015) 934-944.
- [11] Srinivas, A.T., Bharti, R.P. and Chhabra, R.P., Mixed convection heat transfer from a cylinder in power-law fluids: Effect of aiding buoyancy, *Ind. Eng. Chem. Res.*, **48** (2009) 9735-9754.
- [12] Shahzad, A. and Ali, R., MHD Flow of a non-Newtonian power law fluid over a vertical stretching sheet with the convective boundary condition, *Walailak J. Sci. Tech.*, **10** (1) (2013) 43-56.
- [13] Sui, J., Zheng, L., Zhang, X. and Chen, G., Mixed convection heat transfer in power law fluids over a moving conveyor along an inclined plate, *Int. J. Heat Mass Transf.*, **85** (2015) 1023-1033.

- [14] Naseer, M., Malik, M.Y. and Rehman, A., Numerical study of convective heat transfer on the power law fluid over a vertical exponentially stretching cylinder, *Appl. Comput. Math.*, **4** (5) (2015) 346-350.
- [15] Gebhart, B., Effects of viscous dissipation in natural convection, *J. Fluid Mech.*, **14** (1962) 225-232.
- [16] Chamkha, A.J., Aly, A.M. and Mansour, M.A., Unsteady natural convective power-law fluid flow past a vertical plate embedded in a non-Darcian porous medium in the presence of a homogeneous chemical, *Nonlinear Anal.: Model. Control*, **15** (2) (2010) 139-154.
- [17] Vajravelu, K., Prasad, K.V. and Ng, C., Unsteady flow and heat transfer in a thin film of Ostwald–de Waele liquid over a stretching surface, *Commun. Nonlinear Sci. Numer. Simulat.*, **17** (2012) 4163-4173.
- [18] Abel, M.S., Tawade, J.V. and Agadi, A.H., An analysis for non uniform heat source for the Maxwell fluids over a stretching sheet in presence of viscous dissipation, *Int. J. Adv. Comput. Math. Sci.*, **3** (4) (2012) 471-481.
- [19] Kishan, N. and Kavitha, P., Magneto-hydrodynamic flow and heat transfer of non-Newtonian power-law fluid over a non-linear stretching surface with viscous dissipation, *Int. J. Appl. Mech. Eng.*, **19** (2) (2014) 259-273.
- [20] Hayat, T., Shafiq, A. and Alsaedi, A., Effect of joule heating and thermal radiation in flow of third grade fluid over radiative surface, *PLoS ONE*, **9** (1) (2014): e83153. doi:10.1371/journal.pone.0083153.



- [21] Hiemenz, K., Die Grenzschicht an einem in den gleichförmigen Flüssigkeitsstrom eingetauchten geraden Kreiszylinder, *Dingler's Poly. J.*, **326** (1911) 321-324.
- [22] Chiam, T.C., Stagnation-point flow towards a stretching plate, *J. Phys. Soc. Jpn.*, **63** (1994) 2443-2444.
- [23] Mahapatra, T.R. and Gupta, A.S., Magnetohydrodynamic stagnation-point flow towards a stretching sheet, *Acta Mech.*, **152** (2001) 191-196.
- [24] Zhu, J., Zheng, L. and Zhang, X., Flow and heat transfer in a power-law fluid with variable conductivity over a stretching sheet, *Proc. World Cong. Eng.*, **3** (2010) 1893-1897.
- [25] Jahan, S. and Sakidin, H., Influence of heat transfer on the MHD stagnation point flow of a power law fluid with convective boundary condition, *Jurnal Teknologi (Sciences & Engineering)*, **77** (20) (2015) 53-59.
- [26] Singh, K. and Kumar, M., Melting and heat absorption effects in boundary layer stagnation-point flow towards a stretching sheet in a micropolar fluid, *Ain Shams Eng. J.*, (2016), <http://dx.doi.org/10.1016/j.asej.2016.04.017>
- [27] Adegbeie, S.K., Koriko, O.K. and Animasaun, I.L., Melting heat transfer effects on stagnation point flow of micropolar fluid with variable dynamic viscosity and thermal conductivity at constant vortex viscosity, *J. Nigerian Math. Soc.*, **35** (2016) 34-47.

- [55] Khan, W.A. and Pop, I., Boundary-layer flow of a nanofluid past a stretching sheet, *Int. J. Heat Mass Transf.*, **53** (2010) 2477-2483.
- [56] Wang, C.Y., Free convection on a vertical stretching surface, *J. Appl. Math. Mech. (ZAMM)*, **69** (1989) 418-420.
- [57] Gorla, R.S.R. and Sidawi, I., Free convection on a vertical stretching surface with suction and blowing, *Appl. Sci. Res.*, **52** (1994) 247-257.
- [58] Liao, S., Beyond perturbation : Introduction to homotopy analysis method, CRC Press LLC, London, 2004.
- [59] Nield, D.A. and Kuznetsov, A.V., Thermal instability in a porous medium layer saturated by a nanofluid: A revised model, *Int. J. Heat Mass Transf.*, **68** (2014) 211-214.
- [60] Kuznetsov, A.V. and Nield, D.A., Natural convective boundary-layer flow of a nanofluid past a vertical plate: A revised model, *Int. J. Therm. Sci.*, **77** (2014) 126-129.
- [61] Chaudhary, M.A. and Merkin, J.H., A simple isothermal model for homogeneous-heterogeneous reactions in boundary-layer flow I. Equal diffusivities, *Fluid Dyn. Res.*, **16** (1995) 311-333.
- [62] Chaudhary, M.A. and Merkin, J.H., Homogeneous-heterogeneous reactions in boundary-layer flow: effects of loss of reactant. *M&L Comput. Model.*, **24** (3) (1996) 21-28.